Doctor thesis

2017

Structural and Functional Studies of *Clostridium perfringens* Iota-like Enterotoxin (CPILE)

Kyoto Sangyo University Graduate School

Division of Life Sciences

Doctor course, 4th year

GNo. 456032

Waraphan Toniti

Table of Contents

Abbreviations

General Introduction:

CPE	*Clostridium perfringens* enterotoxin
Ia	Enzymatic subunit of iota toxin from *Clostridium perfringens*
Ib	Membrane transporting subunit of iota toxin from *Clostridium perfringens*
LSR	Lipolysis-stimulated lipoprotein receptor
NAD	Nicotinamide adenine dinucleotide
NAD^+	Oxidized form of Nicotinamide adenine dinucleotide
NADH	Reduced form of Nicotinamide adenine dinucleotide
ATP	Adenosine triphosphate
G-actin	Globular actin
F-actin	Filamentous actin
BEC	Binary enterotoxin of *Clostridium perfringens*
CPILE	*Clostridium perfringens* iota-like enterotoxin

Chapter I:

ARTs	Group of toxins harbor a catalytic ADP-ribosyltransferase domain
ARTC	Clostridia-toxin-like ART subfamily with conserved RSE motifs
ARTD	Diphtheria-toxin-like ART subfamily with conserved HYE motifs
PEGs	Polyethylene glycol
MOPS	3-(N-morpholino) propane sulfonic acid
MR	Molecular Replacement
MAD	Multi-wavelength Anomalous Diffraction
SAD	Single-wavelength Anomalous Diffraction
FOM	Figure of Merit
PT	Protruding loop

Chapter III:

NADase	NAD glycohydrolase

ARTase	ADP-ribosyltransferase
AMP	Adenosine monophosphate

Chapter IV:

FITC	Fluorescein isothiocyanate labelling technique
PN loop	Phosphate nicotinamide loop
ARTT loop	ADP-ribosylating turn-turn loop
βTAD	Thiazole-4-carboxamide adenine dinucleotide

Chapter VI:

EXE-C3	Exoenzyme C3 mutant (from wild type QXE to mutant EXE on the ARTT loop)

List of tables

List of figures

Page

General Introduction

Clostridium perfringens

The Gram-positive anaerobic, spore-forming bacteria, *Clostridium* spp., are commonly found in soil, marine, fresh water sediments, and gastrointestinal tracts of animals as well as humans. Members of these pathogenic bacteria are involved in a variety of diseases including gas gangrene, food poisoning, antibiotic-associated diarrhea, pseudomembranous colitis, and enterotoxemia of humans, domestic animals, and wildlife (Songer, 1996; Petit et al, 1999; Stiles et al, 2014; Hassen et al, 2015). *Clostridium perfringens* have been classified into five toxin types (A-E) on the basis of the production of four major lethal toxins (α, β, ε, and ι). Most of the virulent genes from *C. perfringens* have been characterized (Table 1). In addition, the *C. perfringens* enterotoxin (CPE) encoded by *cpe* is well known and has been studied worldwide. This CPE causes diarrhea by forming pores in enterocytes and subsequent leakage of water and ions.

Table 1: Classification of *C. perfringens* major toxins. Modified from Songer, 1996; Petit et al, 1999.

Toxin	Gene name	Mode of action	Biological activity
α	*plc*	Phospholipase C/ sphingomyelinase	Cytolytic, hemolytic, dermonecrotic, lethal
β1	*cpb1*	Pore-forming activity? Cell membrane disruption?	Cytolytic, dermonecrotic, lethal Hemorrhagic necrosis of intestinal mucosa
β2	*cpb2*	Pore-forming activity? Cell membrane disruption?	Cytolytic, lethal Hemorrhagic necrosis of intestinal mucosa
ε	*etx*	Alteration of cell membrane permeability (pore-forming activity?)	Edema in various organs: liver, kidney, and central nervous system Dermonecrotic, lethal
ι	*iap* *ibp*	ADP-ribosylation of actin (Ia)	Disruption of actin cytoskeleton, disruption of cell barrier integrity Dermonecrotic, lethal

The classic method of identification has been the mouse lethality test developed in 1931. An alternative method characterizes the necrotic and erythematous lesions caused by an intradermal injection of *C. perfringens* culture supernatants into a guinea pig. Each type of toxin causes a specific symptom (Table 2); hence, the correct identification of causative pathovars is critical for epidemiological studies and development of effective preventive procedures, including vaccines (Petit et al, 1999).

Table 2: Diseases associated *C. perfringens.* Modified from Songer, 1996; Petit et al, 1999.

Toxin type	**Major toxin(s)**	**Associated pathology**	
		Human	**Animals**
A	α	Gangrene Gastrointestinal diseases (food poisoning, antibiotic-associated diarrhea, sporadic diarrhea)	Myonecrosis, food poisoning, necrotic enteritis (fowl) Enteroxemia (cattle, lambs) Necrotizing enterocolitis (piglets) Diarrhea (foals, pigs) Necrotic enteritis (fowl)
B	α, β, ε		Dysentery (newborn lambs) Chronic enteritis (older lambs) Hemorrhagic enteritis (neonatal calves and foals) Hemorrhagic enterotoxemia (sheep)
C	α, β	Necrotic enteritis	Necrotic enteritis (fowl) Hemorrhagic or necrotic enterotoxemia (neonatal pigs, lambs, calves, goats, and foals) Acute enterotoxemia (sheep)
D	α, ε		Enterotoxemia (lambs, calves) Enterocolitis (neonatal and adult goats)
E	α, ι		Enterotoxemia (calves, lambs) Enteritis (rabbits)

Most of the *C. perfringens* toxins act on the cell membrane (Figure 1). Alpha-toxin is a membrane-damaging toxin and possesses phospholipase C/ sphingomyelinase activities (Figure 1A). The β1-toxin and β2-toxin might be membrane-damaging toxins. A complex of ε-toxin and membrane protein alters the membrane permeability (Figure 1B). The θ-toxin, δ-toxin, and *C. perfringens* enterotoxin (CPE) belong to groups of pore-forming toxins. These groups recognize specific membrane receptors (Figure 1C, 1D).

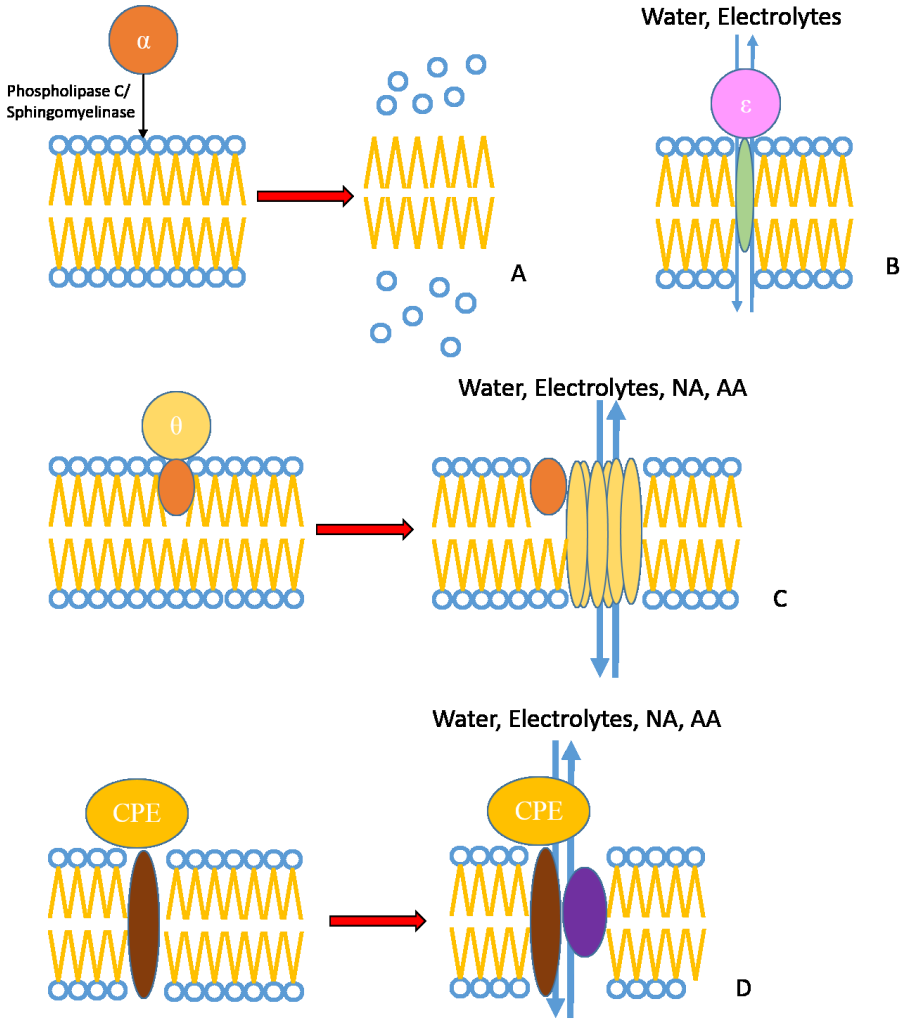

Figure 1: Schematic representation of the targets and modes of action of the *C. perfringens* toxins. A) α-Toxin is a membrane-damaging toxin and causes dissociation of the phospholipid bilayer as a consequence. B) ε-Toxin forms a large complex with a membrane protein (green oval) and alters the membrane permeability. C) θ-Toxin recognizes cholesterol (orange oval) and forms a pore. D) CPE recognizes a protein receptor (brown oval) and forms a large complex with another membrane protein (purple oval). This pore-forming by θ-toxin and CPE-complex causes leakage of small molecules such as, water, ions, nucleic acids (NA) and amino acids (AA). Modified from Petit et al., (1999).

In the case of ι-toxin, this binary toxin acts intracellularly. The binding component (Ib) mediates internalization of the enzymatic component (Ia) into the target cell, as will be described in the next section. After entering the cell, Ia possesses ADP-ribosylation to actin. The consequence of ADP-ribosylation of actin monomers by Ia is disruption of the actin cytoskeleton. Moreover, *C. perfringens* also produces various hydrolytic enzymes, which act as additional virulence factors in gangrenous lesions by favoring degradation of extracellular and lysed cell substrates and providing nutrients for *C. perfringens* growth (Petit et al, 1999).

C. perfringens Iota toxin

Iota toxin is one of the major lethal and dermonecrotic toxins of *C. perfringens* type E. Iota toxin is classified as a member of the clostridial binary toxin group. Iota toxin consists of two unlinked proteins: an enzymatic component (Ia) and a binding component (Ib) (Sakurai and Kobayashi, 1995). Each component is nontoxic; however, a mixture of Ia and Ib are cytotoxic to various cultured cells. Once it binds to the lipolysis-stimulated lipoprotein receptor (LSR) on target cells, Ib forms a heptamer and assists translocation of Ia into cytosol (Papatheodorou et al., 2011). Then Ia–Ib is transported to the endosome where acidification promotes cytosolic entry of Ia. After internalization, Ia ADP-ribosylates globular skeletal muscle α-actin and non-muscle β/γ-actin at Arg-177 (Perelle et al., 1993; Marvaud et al., 2002; Sakurai et al., 2009; Papatheodorou et al., 2011).

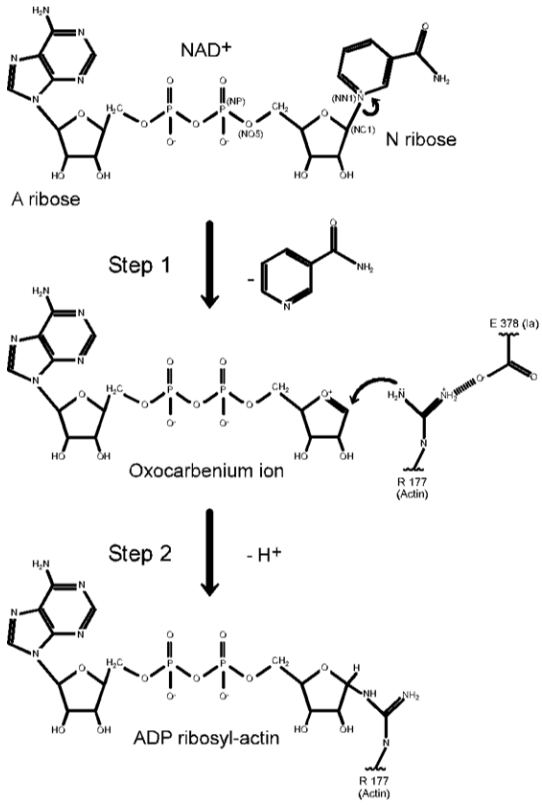

Figure 2: Catalytic mechanism of the ADP-ribosylation reaction. Step 1: Cleavage of the nicotinamide moiety and production of oxocarbenium cation. Step 2: deprotonation of Arg177 of actin and bond formation between the NC1 of N-ribose and guanidyl nitrogen of Arg177. Source: Tsurumura et al., 2013.

Based on several complex structures of Ia–actin, the mechanism of actin–ADP-ribosylation is proposed (Tsurumura et al., 2013) in Figure 2. The strain-alleviation model consists of two main steps and two conformations of the oxocarbenium cation intermediate. The ADP moiety of NAD^+ is gripped between Gln300-Arg352-Arg296 on one side and Asn335-Arg295 on another side of Ia. Once the nicotinamide moiety is cleaved at the first step, the oxocarbenium cation intermediate is formed, which in turn causes strain on the ADP moiety itself. Then, the conformation of the oxocarbenium cation intermediate changes and closes to the protonated $Arg177^A$ (*amino acid residues of actin are shown in superscript) followed by bond formation between the NC1 of N-ribose and the guanidyl nitrogen of $Arg177^A$. At this second step, the strain is relieved, which is termed alleviation (Tsurumura et al., 2013). If there is no actin, Ia shows NAD glycohydrolase activity, which suggests that the oxycarbenium ion is attacked by a water molecule instead of $Arg177^A$.

Monomeric globular actin (G-actin) has a pivotal role in filamentous actin (F-actin) formation essential for cytoskeleton development and cellular processes (Aktories et al., 2011). Actin polymerization proceeds until equilibrium is established between monomeric and filamentous actin (Aktories et al., 2011; Stiles et al., 2011). During polymerization, ATP-bound G-actin preferentially associates with the fast-growing end (barbed end). After reaching equilibrium, actin monomers associate with the barbed end, and an identical number dissociates preferentially from the opposite end (pointed end).

The ADP-ribosylated at Arg177 turns G-actin into a capping protein, which binds to the barbed ends of the actin filaments and blocks the addition of non-modified G-actin to this end. On the other hand, ADP-ribosylated G-actin does not affect the pointed end of the actin filament (Barth and Aktories, 2011). Mono-ADP-ribosylation of G-actin inhibits assembly of F-actin strands through steric hindrance of hydrophobic loop interactions between G-actin molecules.

Pathogen disruption of the eukaryotic cytoskeleton through the ADP-ribosylation of actin can alter many vital processes, including vesicle trafficking, phagocytosis, migration, epithelial barrier formation, and binding to the extracellular matrix, as well as signaling (Aktories et al., 2011; Stiles et al., 2011). Furthermore, depolymerization of F-actin affects regulation of the dynamic behavior of microtubules and causes tubulin protrusion (Figure 3). Toxin-induced formation of the microtubule-based network of protrusions on the surface of epithelial cells has major consequences for adherence of bacteria and, thus, influences host–pathogen interactions (Aktories et al., 2011).

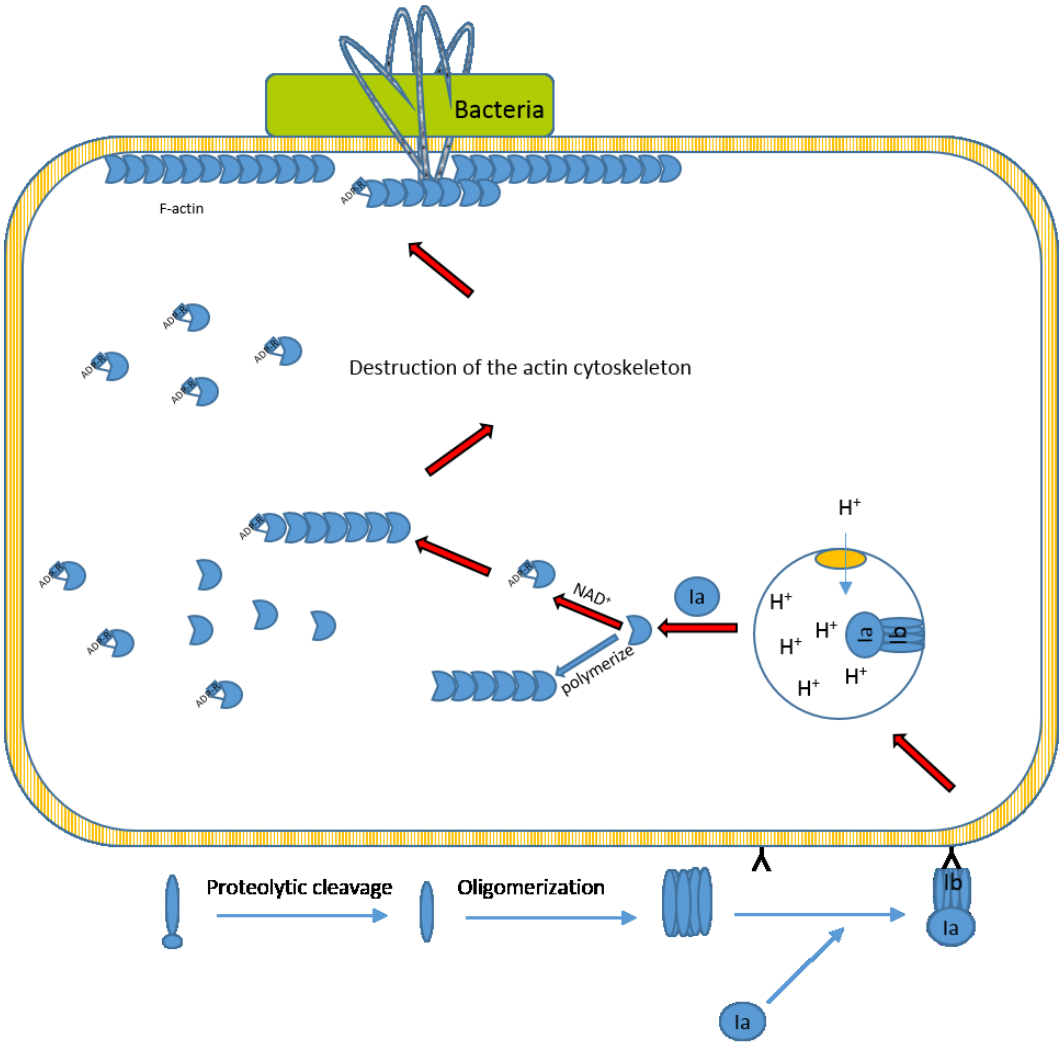

Figure 3: Model of the action of toxin-induced formation of the microtubule-based network of protrusions. Iota toxin consists of an enzymatic ADP-ribosyltransferase component (Ia) and a binding component (Ib). After binding to cell surface receptors, Ib is proteolytically activated and forms heptamers. Then, Ia interacts with Ib and the toxin complex is endocytosed into endosome. Under the acidic conditions of endosomes, the complex inserts into membranes and finally allows translocation of Ia into the cytosol. Ia ADP-ribosylates actin at Arg177 and causes inhibition of actin polymerization. Destruction of the actin cytoskeleton has consequences for the microtubule system. Growing microtubules are no longer captured at the cell membrane and form long protrusions extending from the cell surface. These protrusions facilitate adherence and colonization of bacteria. Modified from Aktories et al., (2011) and Stiles et al., 2011.

C. perfringens iota-like enterotoxin (CPILE)

C. perfringens gastroenteritis is characterized mainly by diarrhea and abdominal pain. To date, *C. perfringens* enterotoxin (CPE) has been considered to be the only virulence factor

responsible for the gastrointestinal symptoms reported in *C. perfringens* type A food-borne outbreaks. On the other hand, non-CPE-producing *C. perfringens* is considered to be non-diarrheagenic and is a normal flora in humans and animals (Monma et al., 2015). To diagnose *C. perfringens* type A food poisoning, the presence of the *cpe* and CPE production are necessary.

There were four strange food-borne diseases in Japan during 1997–2010 in which a new type of enterotoxin produced by *C. perfringens* was strongly suspected to be the cause on the basis of epidemiological information and bacteriological investigations of the isolates (Yonogi et al., 2014; Monma et al., 2015; Irikura et al., 2015). The first two outbreaks occurred in 1997 and 2003 in Tokyo followed by another two similar outbreaks in Osaka (2009) and Tochigi (2010). The isolated OS1 (Osaka) and TS1 (Tochigi) strains were *C. perfringens* type A. They were closely related large plasmids despite their distinct genetic backgrounds (Yonogi et al., 2014). In addition, the Tokyo outbreaks were serotype TW27, similar to the OS1 strain, and differed from serotype TW21 of the TS1 strain (Monma et al., 2015).

The isolates did not harbor the *cpe* nor produce CPE even though the clinical symptoms of the patients and epidemiological characteristics indicated that the outbreaks were caused by *C. perfringens*. The isolated OS1 and TS1 strains were named binary enterotoxin of *C. perfringens* (BEC), whereas the W5052 strain was called *C. perfringens* iota-like enterotoxin (CPILE). However, it has been shown that BEC and CPILE were identical on the basis of the results of a BLAST search (Irikura et al., 2015).

The culture supernatant of *C. perfringens* strain W5052 caused the death of Vero cells and L929 cells that lack the CPE receptor. Interestingly, the trypsin-treated rCPILE-b alone also killed both kinds of cells at high concentration, whereas glutathione S-transferase (GST)-fused rCPILE-b did not (Figure 4). This finding indicated that the pro-sequence must be cleaved before biological activity can occur. Moreover, the cytotoxicity to the Vero cells and L929 cells depended on the amount of rCPILE-a added. It should be noted that a mixture of rCPILE-a and the trypsin-treated rCPILE-b affected the morphology of L929 cells, which showed a balloon-like shape with expanding cytosol, whereas the trypsin-treated rCPILE-b did not. This finding probably indicates a different mechanism of action. The polymerization of actin may be disrupted by ADP-ribosylation performed by rCPILE-a, whereas the trypsin-

treated rCPILE-b may induce cytotoxicity through pore-forming activity. The supernatant also evoked swelling and fluid accumulation in the ileal loops of rabbits (Irikura et al., 2015).

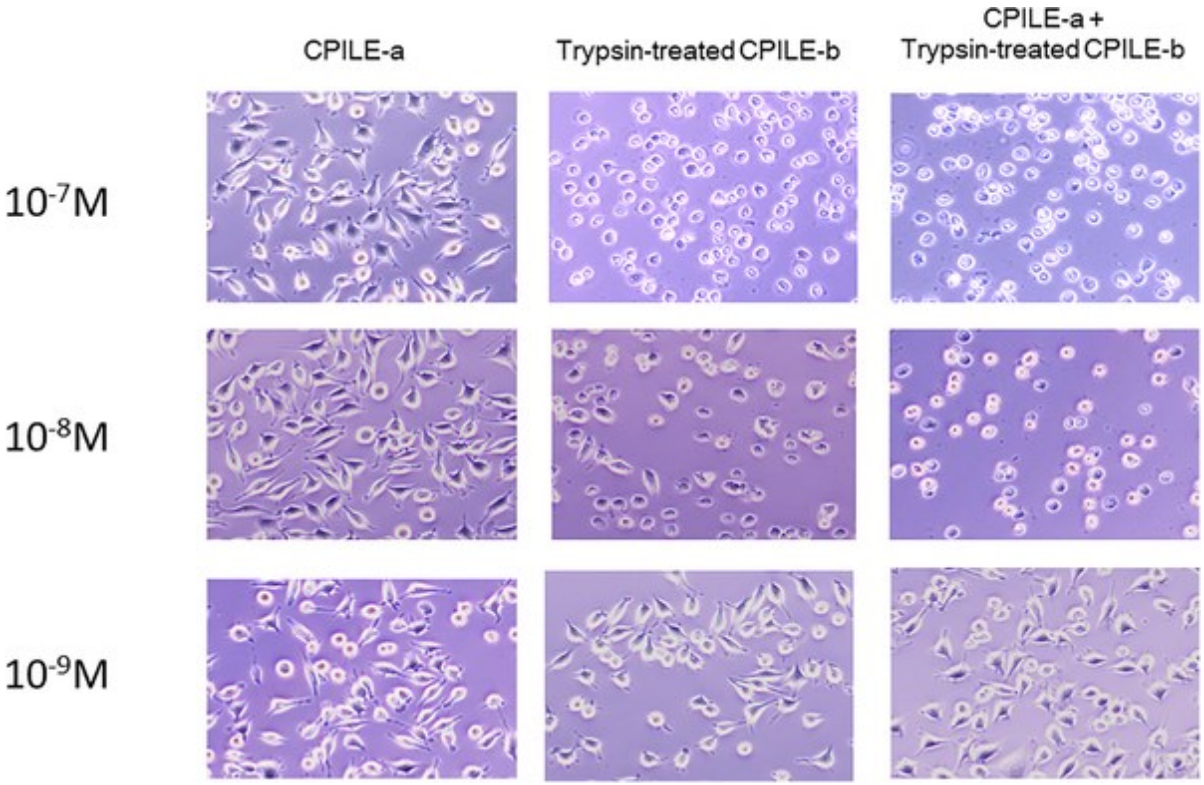

Figure 4: Morphological changes of the L929 cells after treatment with various concentrations of the rCPILE of *C. perfringens* strain W5052. The L929 cells were treated for 16 hours with various concentrations of rCPILE-a, trypsin-treated rCPILE-b, and a mixture of rCPILE-a and trypsin-treated rCPILE-b. The morphology of the L929 cells was observed by optical microscopy. Source: Irikura *et al*., (2015). *PLoS One* 10, e0138183.

The enterotoxicity of CPILE was confirmed by rabbit ileal loop assay. Compared with cholera toxin, no enterotoxic effects of the W5052 strain were observed at low concentrations of a mixture of rCPILE-a and trypsin-treated rCPILE-b (Figure 5; loop 2). On the other hand, the ileal loop became dark red, swollen, and showed fluid accumulation at high concentrations of the mixture (Figure 5; loop 3 and loop 4). CPILE exerted dose-dependent enterotoxic effects (Irikura et al., 2015).

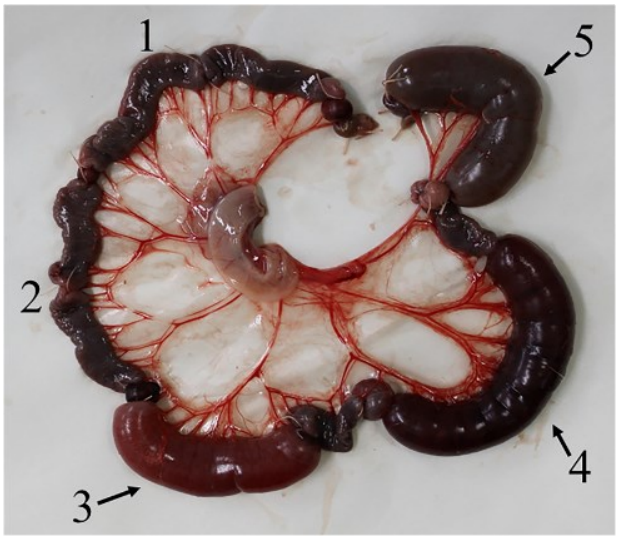

Figure 5: The rabbit ileum loop test for the rCPILE of the *Clostridium perfringens strain* W5052. Fluid accumulation was observed in several ileal loops (arrows) in response to the injected rCPILE. Loop 1, saline; loop 2, rCPIILE-a (0.1 μg) and trypsin-digested rCPILE-b (0.9 μg); loop 3, rCPILE-a (1 μg) and trypsin-treated rCPILE-b (9 μg); loop 4, rCPILE-a (10 μg) and trypsin-treated rCPILE-b (90 μg); and loop 5, cholera toxin (1 μg). Source: Irikura *et al*., (2015). *PLoS One* 10, e0138183.

Objective

As described above, CPILE-a was characterized and studied; however, structural and functional information for this enzyme was lacking. To gain insight into the CPILE-a mechanism of action, enzyme-substrate selection, and recognition of clostridia-toxin-like ADP-ribosylating toxins (ARTC), this study had two main objectives: 1) to characterize CPILE-a in terms of structure and function and 2) to compare CPILE-a with Ia. The crystal structures of apo-, NAD^+, and NADH-CPILE-a will be useful for understanding the structure–function relationship of this novel enterotoxin. The mimicry of the CPILE-a-$R177^A$ interaction through the E49R mutant may show the enzyme-substrate specificity as representative of the other ARTC members.

……

Chapter I

Crystallization and Structure determination of CPILE-a

Expression and purification of CPILE-a

To determine the structure of CPILE-a, three kinds of GST-tagged pGEX4T-2/CPILE-a were expressed in *Escherichia coli*. The CPILE-a of interest included 1) wild-type CPILE-a, 2) selenomethionine-labeled CPILE-a, and 3) triple cysteine-mutated CPILE-a. The triple cysteine mutants were A97C, S185C, and S366C. Then, the CPILE-a in *E. coli* culture was purified by using affinity chromatography followed by gel filtration chromatography. The GST-tag was cleaved by thrombin. The GST-tagged CPILE-a was 73.5 kDa as shown in the Sepharose without thrombin lane, whereas the purified CPILE-a was 47.5 kDa after thrombin cleavage, as shown in the flow-through with thrombin and fraction numbers 28–35 lanes. The GST was 26 kDa as shown in the Sepharose with thrombin lane. (Figure 6).

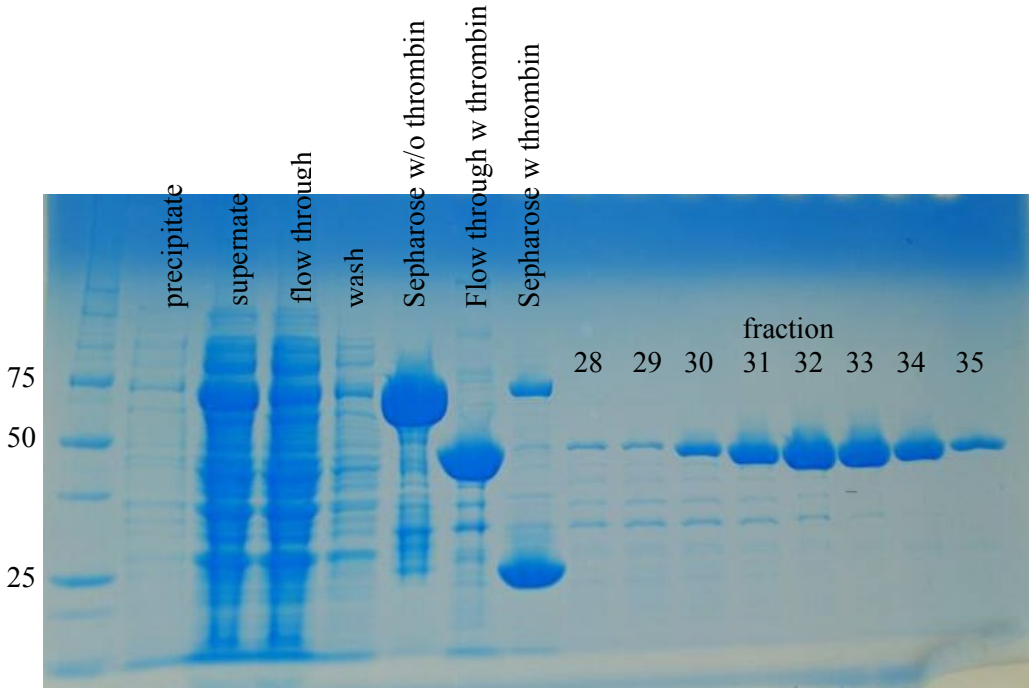

Figure 6: Coomassie Brilliant Blue stain of the purified CPILE-a. Protein marker ran on the left. It should be noted that the first seven lanes were collected from an Affinity column, and the next eight lanes on the right were collected from a Superdex 200 column.

There was not much difference in the expression and purification among all of the mutants and wild-type CPILE-a except that the yields of purified selenomethionine-labeled CPILE-a and triple cysteine-mutated CPILE-a were much lower than that of the wild-type CPILE-a.

Crystallization of CPILE-a

Theoretically, protein crystallization should occur when the concentration of protein and precipitant are higher than the threshold value. The closed system of the hanging drop method allows vapor diffusion to occur; hence, the protein/precipitant solution reaches equilibrium. The solution concentration ranges from unsaturated to supersaturated with protein. The unsaturated area has low concentrations of protein and precipitant, and the supersaturated area has high concentrations of protein in solution (Figure 7 and 8).

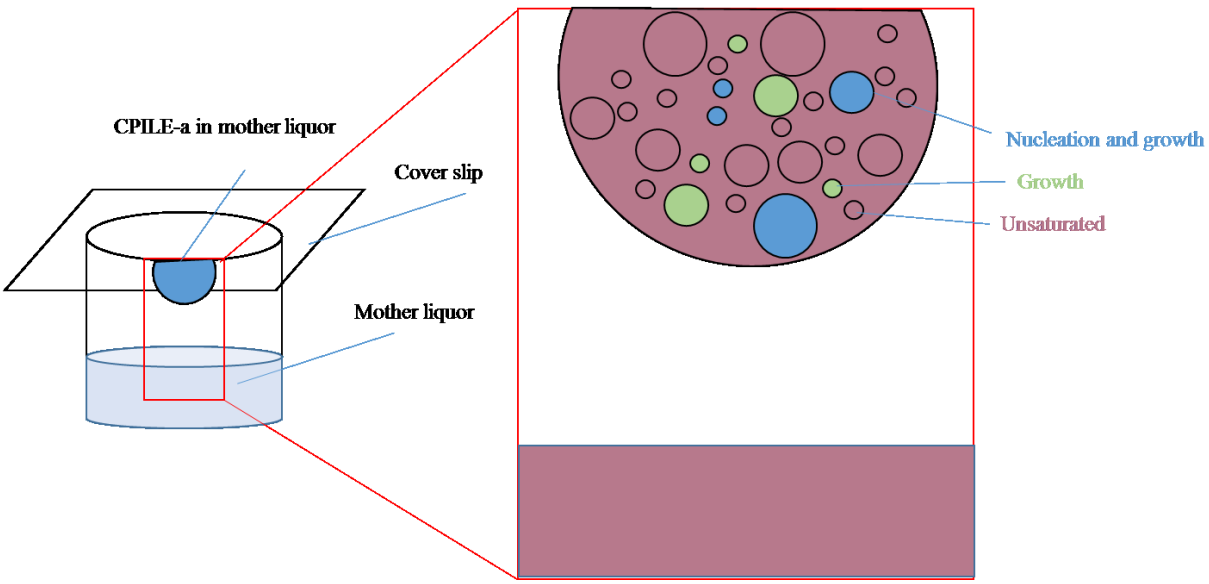

Figure 7: Hanging drop system and growing crystals. The hanging drop is a closed system composed of two main components: a basin and a cover slip. This system is sealed by grease to protect the protein drop from air and allow simultaneously exchange of the mother liquor in the drop and in the basin until equilibrium occurs. Modified from Rhodes G., 2006.

Only the supersaturated area allows nucleation and/or crystal growth. However, the supersaturated solution is unstable. An ideal strategy for growing large crystals is to allow nucleation to occur under conditions in the blue region, then to move to conditions in the green region until crystal growth ceases (Rhodes G., 2006; Figure 7 and 8).

The phase diagram below shows the conditions under which crystallization of the protein occurs (Figure 8). The protein solubility can be divided into three regions: undersaturated (stable), supersaturated (metastable and labile), and very highly supersaturated (precipitation). In the undersaturated region, the concentrations of protein and precipitant are relatively low. Proteins are in random orientation surrounded by mother liquor, including water and precipitant. Once protein molecules cross the solubility line (magenta line), the mother liquor becomes metastable and the proteins enter a supersaturated state. However, there is no spontaneous nucleation. In this state, protein molecules may form transient nuclei but they do not reach critical size. An external stimulus, such as seeding, may be necessary to induce crystallization (Rupp B., 2003).

Homogenous nucleation occurs and reaches critical size, while further supersaturation of the solution occurs in the labile region. However, better crystals grow continuously in the metastable region in contrast to the labile region.

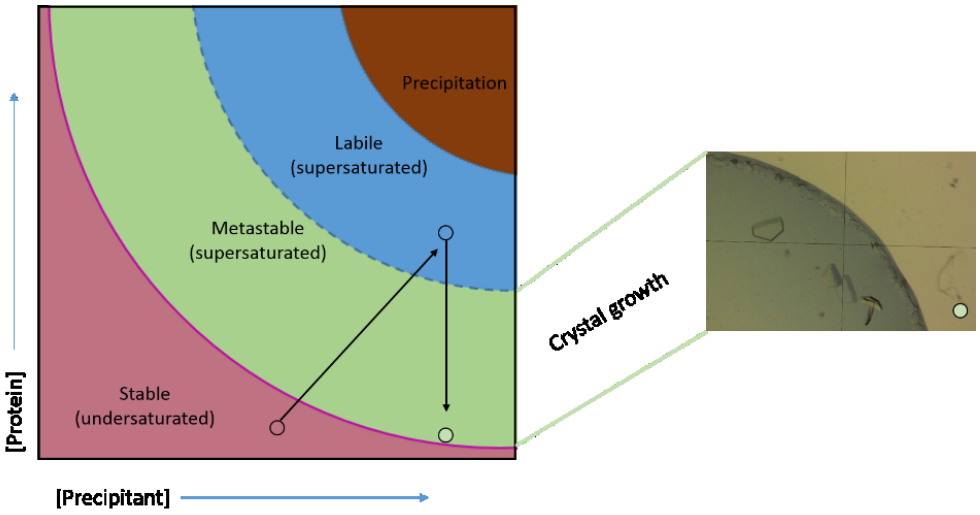

Figure 8: Phase diagram for crystallization of CPILE-a. The cerise color represents a region of low concentration of protein and precipitant. The green and blue colors represent regions of supersaturation with protein. The brown color represents a region of very high supersaturation with protein. Modified from Rupp B. (2003); Rhodes G. (2006); McPherson A. and Gavira JA. (2014).

After a number of trials of crystal screening performed by using several Hampton screening kits, we concluded that polyethylene glycol (PEGs) were good precipitants and suitable for CPILE-a crystallization. Moreover, Tris HCl buffer at high pH and $MgCl_2$ salt were a good combination for CPILE-a crystallization. On the other hand, alcohol-based solutions were not suitable for CPILE-a and probably denatured it. Purified CPILE-a was crystallized by using the standard Hampton screening system and the hanging drop method. In this study, the purified CPILE-a was subjected to supersaturated conditions by varying the concentration of the PEG 4000 in the droplet (Figure 9). The CPILE-a screening plates were screened and kept at 4 °C until data collection.

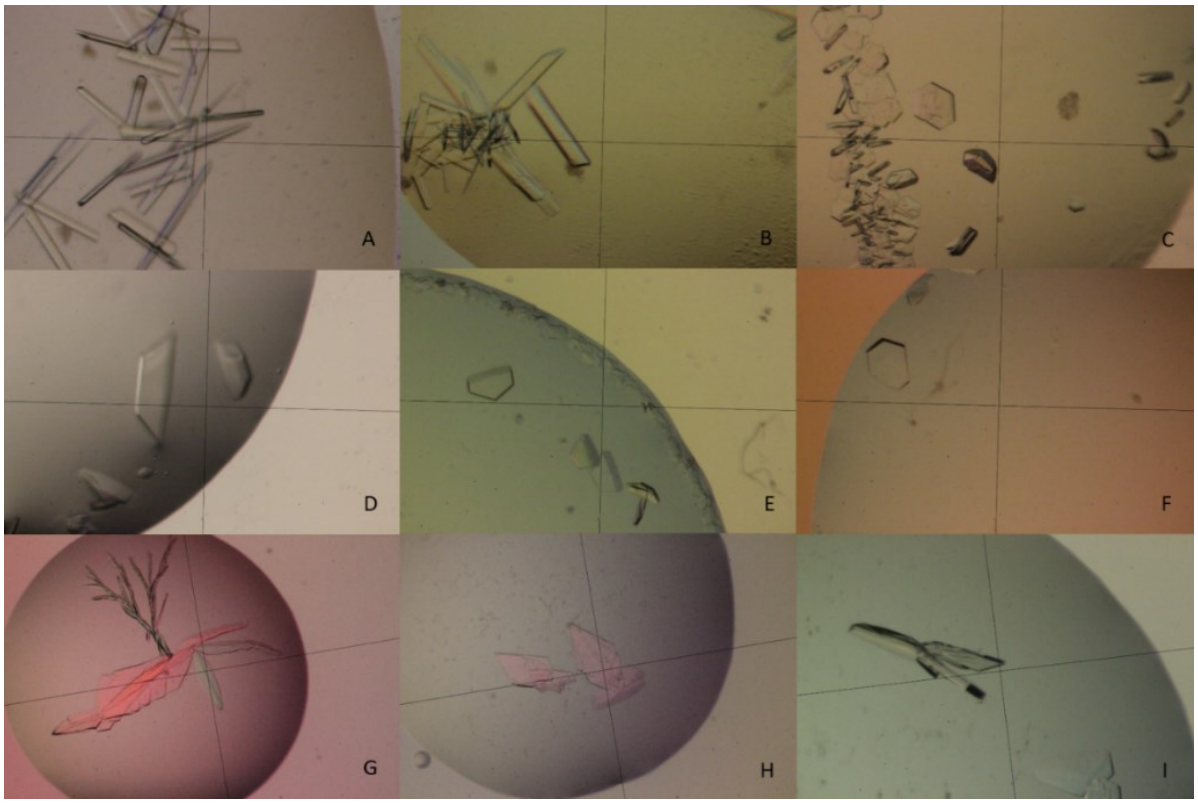

Figure 9: CPILE-a crystals via hanging drop method. A–C Wild-type CPILE-a crystals showing cylindrical and hexagonal shapes. It should be noted that a variety of crystal shapes from A to C were generated by using seeding technique. D–F Selenomethionine-labeled CPILE-a crystals showing the typical CPILE-a crystal shape. G–I Triple cysteine-mutated CPILE-a crystals showing blades or trees shapes.

When using the Hampton screening kit #6, which consists of PEG 4000, 100 mM Tris HCl Buffer at pH 8.5, and 200 mM $MgCl_2$ salt, the purified CPILE-a took $\leq$ 3 days to form crystals. The typical shapes of the CPILE-a crystal were trapezoidal and hexagonal (Figure 9C-F). Cylindrical shapes were formed in seeded MOPS (3-(N-morpholino) propane sulfonic acid) buffer crystal. The most abundant shapes of triple cysteine-mutated CPILE-a crystals were thin, fragile, and formed blades or trees (Figure 9G-H). However, the more typical shapes of CPILE-a crystals were selected carefully and used for data collection (Figure 9I).

Structure determination of CPILE-a

The first attempt at structure determination of CPILE-a started with the wild-type crystals (Figure 10). At this trial, there was a problem determining the correct space group of CPILE-a. The *I*222 and *C*222 were found in data collection of the wild-type CPILE-a crystals. Several attempts to solve the structure of wild-type CPILE-a by using Ia (1GIQ) as a structural template for the molecular replacement (MR) method failed because of the phase problem (Taylor, 2003). The R-work and R-free did not decrease. The R-work value represents how well the simulated diffraction pattern matches the experimentally observed diffraction pattern. However, it may introduce bias into the refinement process. Thus, 10% of the experimental observations are removed from the data set before refinement. The R-free value is then calculated, and a refinement process using remain data set is performed. The R-free value represents how well the model predicts relative to the prediction using the excluded 10% data set.

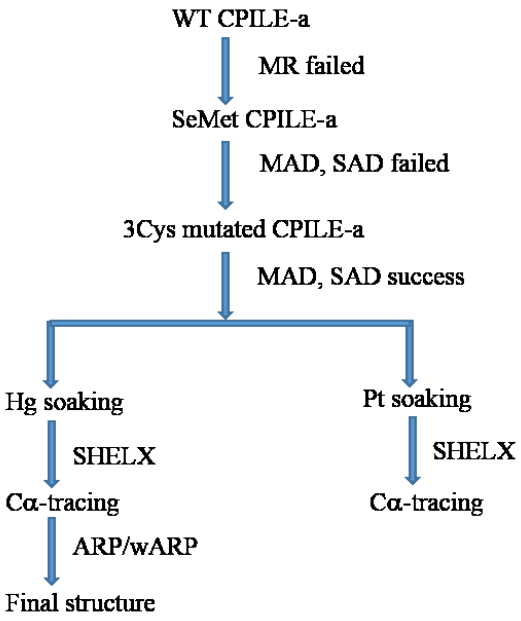

Figure 10: Schematic of phase determination of CPILE-a *I*222 crystal.

The MR failed for two reasons: the wrong space group and/or wrong model search was used or both. To solve the phase problem, selenomethionine-labeled CPILE-a and the anomalous scattering method were used. Multi-wavelength Anomalous Diffraction (MAD) and Single-wavelength Anomalous Diffraction (SAD) had been used to locate the selenomethionine. Unfortunately, those two methods failed again. The third attempt used heavy atom soaking of the triple cysteine-mutated CPILE-a. Several pieces of evidence showed that successful phase determination by mercuration of cysteine was achieved (Blundell and Johnson, 1994). However, CPILE-a had no cysteine residue; thus, it was necessary to make a cysteine mutant for heavy atom soaking. The triple cysteine mutants modified CPILE-a at Ala97, Ser185, and Ser366 in the third try.

The triple cysteine mutant CPILE-a was expressed, purified, and crystallized in the same manner as the wild-type CPILE-a. Then, the crystals were soaked in 1 mM mercury chloride mother liquor for 22 hours. Next, the data sets at three different wavelengths for peak, edge, and remote were collected by using an NW-12A beamline in KEK PF-AR (Table 3).

Additionally, an isomorphous crystal was detected and soaked with platinum chloride solution for 22 hours. Then, the data sets at the three different wavelengths were collected by using the same NW-12A beamline. Both heavy atom-soaked data sets were used for phase

determination by using program suite SHELX C/D/E (Schneider and Sheldrick, 2002; Sheldrick, 2008; Sheldrick, 2010).

Table 3: Data collection of native and heavy atom-soaked CPILE-a.

Data collection	**Wild type CPILE-a**	**Hg-soaking triple cysteine mutated CPILE-a**	**Pt-soaking triple cysteine mutated CPILE-a**
Space group	*I*222	*I*222	*I*222
Cell dimensions			
a, b, c (Å)	70.3, 100.7, 126.0	70.2, 101.5, 126.5	70.4, 99.9, 125.6
a, b, g (°)	90.0, 90.0, 90.0	90.0, 90.0, 90.0	90.0, 90.0, 90.0
X-ray source	MicroMax-007, RAXIS VII (RIGAKU)	PF-AR NW 12A	PF-AR NW 12A
Wavelength (Å)	1.5418	Peak: 1.0070 Edge: 1.0099 Remote H: 0.9937	Peak: 1.0725 Edge: 1.0729 Remote L: 1.0775
Resolution range (Å)	50.00-2.01 (2.04-2.01)	50.00-2.20 (2.24-2.20)	50.00-1.99 (2.02-1.99)
Observed reflections	198493	255478	335650
Rmeas[a]	0.099 (0.660)	0.098 (0.491)	0.069 (0.382)
Rpim[b]	0.037 (0.262)	0.041 (0.206)	0.028 (0.166)
$CC_{1/2}$[c]	(0.885)	(0.927)	(0.957)
I / σI (%)	31.2 (2.9)	29.8 (5.8)	37.4 (5.1)

Completeness (%)	98.3 (85.8)	100.0 (100.0)	99.9 (100.0)
Redundancy	6.7 (5.2)	5.8 (5.7)	5.7 (5.2)

[a]*R*meas = $\sum_{hkl}\{N(hkl)/[N(hkl)-1]\}^{\frac{1}{2}}\sum_i|I_i(hkl)-\langle I(hkl)\rangle|/\sum_{hkl}\sum_i I_i(hkl)$,

[b]*R*pim = $\sum_{hkl}\{1/[N(hkl)-1]\}^{\frac{1}{2}}\sum_i|I_i(hkl)-\langle I(hkl)\rangle|/\sum_{hkl}\sum_i I_i(hkl)$, where $I_i(hkl)$ are the observed intensities, $\langle I(hkl)\rangle$ is the average intensity and $N(hkl)$ is the multiplicity of reflection hkl.

[c]$CC_{1/2}$ = percentage of correlation between intensities from random *hkl*-data sets

Table 3 presents the data collection summary of three data sets: wild-type CPILE-a, Hg-soaked triple cysteine-mutated CPILE-a, and Pt-soaked triple cysteine-mutated CPILE-a. The wild-type CPILE-a data set was collected by using in-house x-ray diffractometer at Kyoto Sangyo University, whereas the heavy atom-soaked data sets were collected at the Photon Factory. The data are summarized in Appendix A.

As a starting point, SHELXC was used to prepare input for SHELXD. Then, SHELXD was used to find the substructure. At this point, SHELXD plotted the substructure coordinates of a subset of atoms within the same unit cell. Once SHELXD was able to plot the substructure coordinates, they were used to overcome the phase problem. The success criterion was the correlation coefficient between E_{obs} and E_{calc}. In the case of SAD, a CC_{all} value of $\geq$ 30% was a good indication of a correct solution (Schneider and Sheldrick, 2002; Sheldrick, 2008; Sheldrick, 2010). SHELXE was used to autotrace of the peptide backbone and report the poly-Ala polypeptide chains model as a pdb file. If the value of CC for the partial structure against the native data was $\geq$ 30%, it was a strong indicator of a successful structure solution. Another value was the Pseudo-free CC, which indicated a successful structure solution if this value was $\geq$ 65% (Grüne, 2010).

The heavy atom data sets were used for the phasing of the MAD and SAD calculation by SHELX (Table 4 and Table 5). The Figure of Merit (FOM) of the Hg-soaked data sets showed that MAD_{ori} and MAD_{inv} were 0.525 and 0.500, respectively (Table 4). The FOM of SAD_{ori} and SAD_{inv} were 0.589 and 0.536, respectively. The origin (ori) and invert (inv) show the right-hand and left-hand coordinate, respectively. The correct hand shows a high FOM. MAD_{ori} was better than MAD_{inv}, so MAD_{ori} was the correct answer. SAD_{ori} was also better than SAD_{inv}, so SAD_{ori} was the correct answer. The highest pseudo-free CC of 64.29% belonged to the SAD_{ori} data. The CC for the partial structure against the native data also showed the highest value at 31.34% for SAD_{ori}. Taken together, among the Hg-soaked data sets, SAD_{ori} gave the best results.

Table 4: Statistics of SHELX phasing; Hg MAD and SAD experiment.

Hg position (MAD_{ori})				**FOM**	**Pseudo-free CC (%)**	**CC[a] (%)**	**Cα-tracing[b]**
Site	**x**	**y**	**z**				
1	0.0684	0.7233	0.0871	0.525	57.27	7.79	15 (143)
2	0.3260	0.6940	0.0086				
3	-0.0993	0.8025	0.0497				
Hg position (MAD_{inv})				**FOM**	**Pseudo-free CC (%)**	**CC[a] (%)**	**Cα-tracing[b]**
Site	**x**	**y**	**z**				
1	0.9316	0.2767	0.9129	0.500	54.02	5.60	14 (125)
2	0.6740	0.3060	0.9915				
3	1.0993	0.1975	0.9503				
Hg position (SAD_{ori})				**FOM**	**Pseudo-free CC (%)**	**CC[a] (%)**	**Cα-tracing[b]**
Site	**x**	**y**	**z**				
1	0.5685	0.7770	0.0870	0.589	64.29	31.34	18 (344)
2	0.8262	0.8053	0.0085				
3	0.4054	0.6976	0.0485				
Hg position (SAD_{inv})				**FOM**	**Pseudo-free CC**	**CC[a]**	**Cα-tracing[b]**

Site	x	y	z		(%)	(%)	
1	0.4315	0.2230	0.9130	0.536	58.46	5.47	15 (139)
2	0.1738	0.1947	0.9915				
3	0.5946	0.3024	0.9514				

[a]CC for partial structure against native data
[b]Number of Cα-tracing chains; Number of Cα-tracing residues showed in parenthesis.

For the Pt-soaked data sets, the highest pseudo-free CC of 62.95% belonged to SAD_{ori} data (Table 5). The CC for the partial structure against the native data showed the highest value at 11.84% for SAD_{ori}. Among the Pt-soaked data sets, SAD_{ori} gave the best results.

Table 5: Statistics of SHELX phasing; Pt MAD and SAD experiment.

Pt position (MAD_{ori})				**FOM**	**Pseudo-free CC (%)**	**CC[a] (%)**	**Cα-tracing[b]**
Site	**x**	**y**	**z**				
1	0.7271	0.4301	0.0108	0.466	51.53	4.04	13 (113)
2	0.7638	0.4064	0.0185				
3	0.7446	0.4142	-0.0407				
4	0.7368	0.2650	-0.0156				
Pt position (MAD_{inv})				**FOM**	**Pseudo-free CC (%)**	**CC[a] (%)**	**Cα-tracing[b]**
Site	**x**	**y**	**z**				
1	0.2729	0.5699	0.9892	0.496	55.02	4.86	11 (94)
2	0.2362	0.5936	0.9815				
3	0.2554	0.5858	1.0407				

4	0.2632	0.7350	1.0156				
Pt position (SAD_{ori})				**FOM**	**Pseudo-free CC (%)**	**CC[a] (%)**	**Cα-tracing[b]**
Site	**x**	**y**	**z**				
1	0.7724	0.9309	0.0105	0.566	62.95	11.84	14 (272)
2	0.7385	0.9047	0.0178				
3	0.6876	0.8064	-0.0070				
4	0.6874	0.9175	0.0192				
Pt position (SAD_{inv})				**FOM**	**Pseudo-free CC (%)**	**CC[a] (%)**	**Cα-tracing[b]**
Site	**x**	**y**	**z**				
1	0.2276	0.0691	0.9895	0.524	58.28	6.85	15 (132)
2	0.2615	0.0953	0.9822				
3	0.3124	0.1936	1.0070				
4	0.3126	0.0825	0.9808				

[a]CC for partial structure against native data
[b]Number of Cα-tracing chains; Number of Cα-tracing residues showed in parenthesis.

The Hg-soaked and Pt-soaked data sets were used to locate the heavy atoms in the asymmetric unit. The SHELXE data showed that the Hg-soaked SAD_{ori} data was the best followed by the Pt-soaked SAD_{ori} data. Therefore, these two data sets were used to represent the results of Cα-tracing by SHELX (Figure 11).

Figure 11 shows the Cα-tracing of the Hg-soaked CPILE-a on the left and Pt-soaked CPILE-a on the right. The SHELX results were for several fragments of the poly-Ala polypeptide chain. For the Hg-soaked SAD data set, the results of Cα-tracing showed 344 alanine residues in 18 polypeptide chains, whereas the results of Cα-tracing of the Pt-soaked SAD data set represented 139 alanine residues in 15 polypeptide chains. After review of the SHELXE results, the Hg-soaked SAD_{ori} data set was selected and subjected to model building because it showed the best results from the Cα-tracing. Those fragments were then filled up to 419 amino acid residues by using ARP/wARP as an automated model building program (Langer et al., 2008). Then, the full-length Hg-soaked model was used as a search model for refining the wild-type CPILE-a data set.

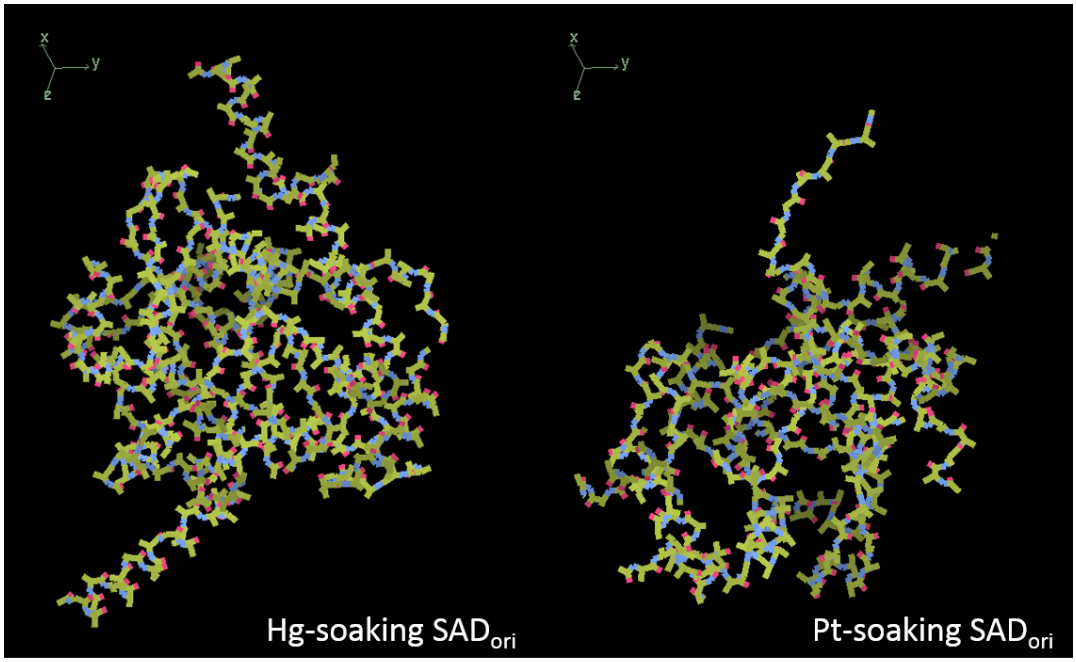

Figure 11: Cα tracing using SHELX. The poly-alanine polypeptides of Hg-soaked triple cysteine-mutated CPILE-a is shown on the left and the poly-alanine polypeptides of the Pt-soaked triple cysteine-mutated CPILE-a is shown on the right. Both of them support the original structure of SHELX.

The wild-type CPILE-a structure was solved at 2.01 Å by using MR method and the Hg-soaked SAD_{ori} structure as a search model. Wild-type CPILE-a belongs to a member of the *I*222 space group and is composed of one molecule in an asymmetric unit (Table 6).

Table 6: Refinement statistics of wild type CPILE-a.

Refinement	**Wild type CPILE-a**
Resolution (Å)	21.8-2.01
R_{work}/R_{free} [a] (%)	17.6 / 22.9
Overall B factors (Å^2)	44.0
r.m.s.deviations	
Bond lengths (Å)	0.007
Bond angles (°)	1.084
Ramachandran plot	
Favored regions (%)	97.35
Allowed regions (%)	2.41
Outliers (%)	0.24
PDB ID	5GTT

[a] Rwork = $\sum_{hkl}||F_{obs}| - |F_{calc}||/\sum_{hkl}|F_{obs}|$. Rfree is the cross-validation R factor for the test set (5%) of reflections

omitted from model refinement.

Later, we evaluated the binding site of Hg-soaked and Pt-soaked data sets using the final structure. In the case of Hg-soaking, only three large electron density regions were detected: the triple cysteine-mutated CPILE-a composed of A97C, S185C, and S366C. However, only Cys185 and Cys366 showed a large peak in the |Fo-Fc| map. Interestingly, the third large peak was found near His157 (Figure 12).

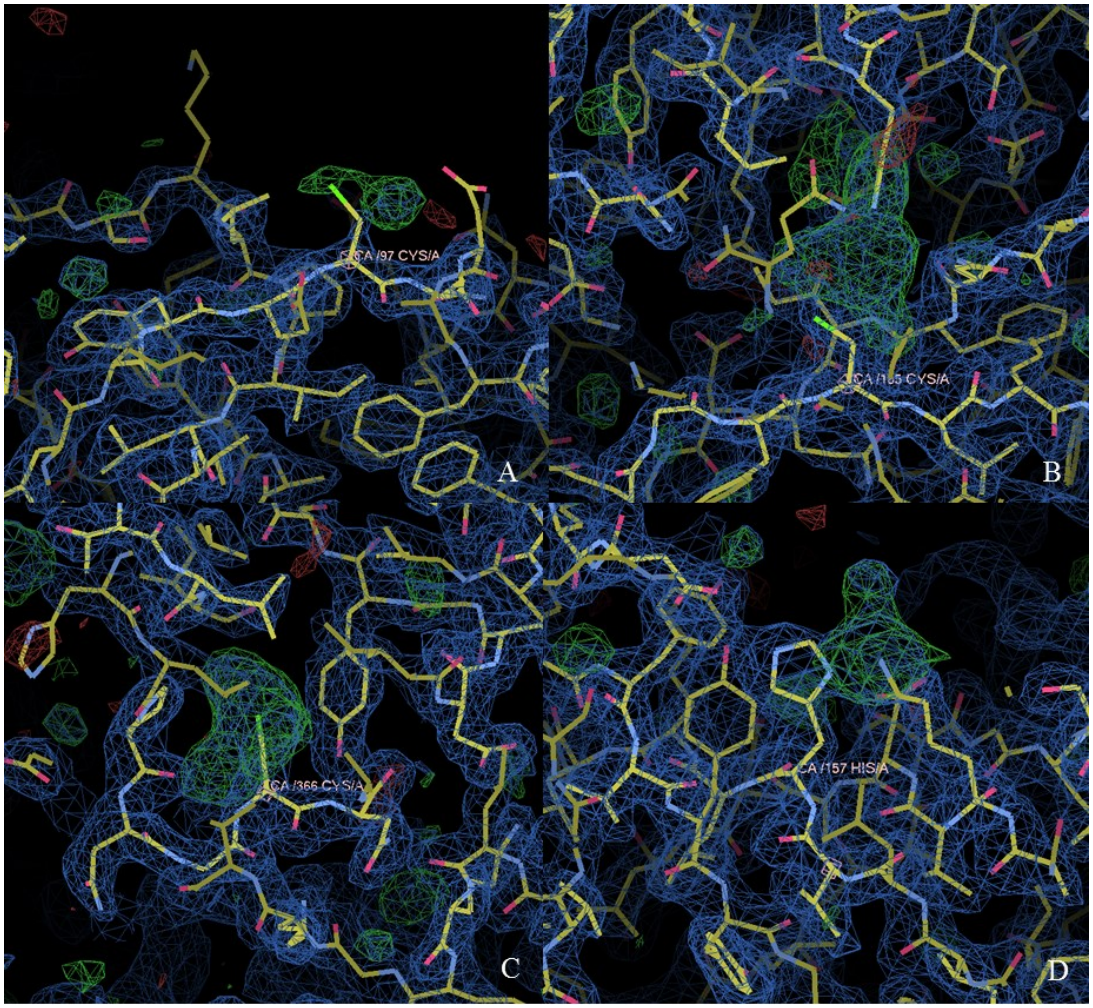

Figure 12: Hg-soaked CPILE-a. A–D, the electron density maps of Cys97, Cys185, Cys366, and His157. The A97C-mutated CPILE-a showing a small peak in the |Fo-Fc| map that probably represents another rotamer of the cysteine residue. Large peaks were found at S185C, S366C, and H157 in the |Fo-Fc| map.

Compared with the Hg-soaked data set, the Pt-soaked CPILE-a showed four large electron density regions at Cys97, Cys185, Cys366, and Met8 (Figure 13). Interestingly, the biggest electron density region was found at the Met8 site (Figure 13D). In corporation of

heavy atoms in the triple cysteine mutant have been responsible for solving the phase problem.

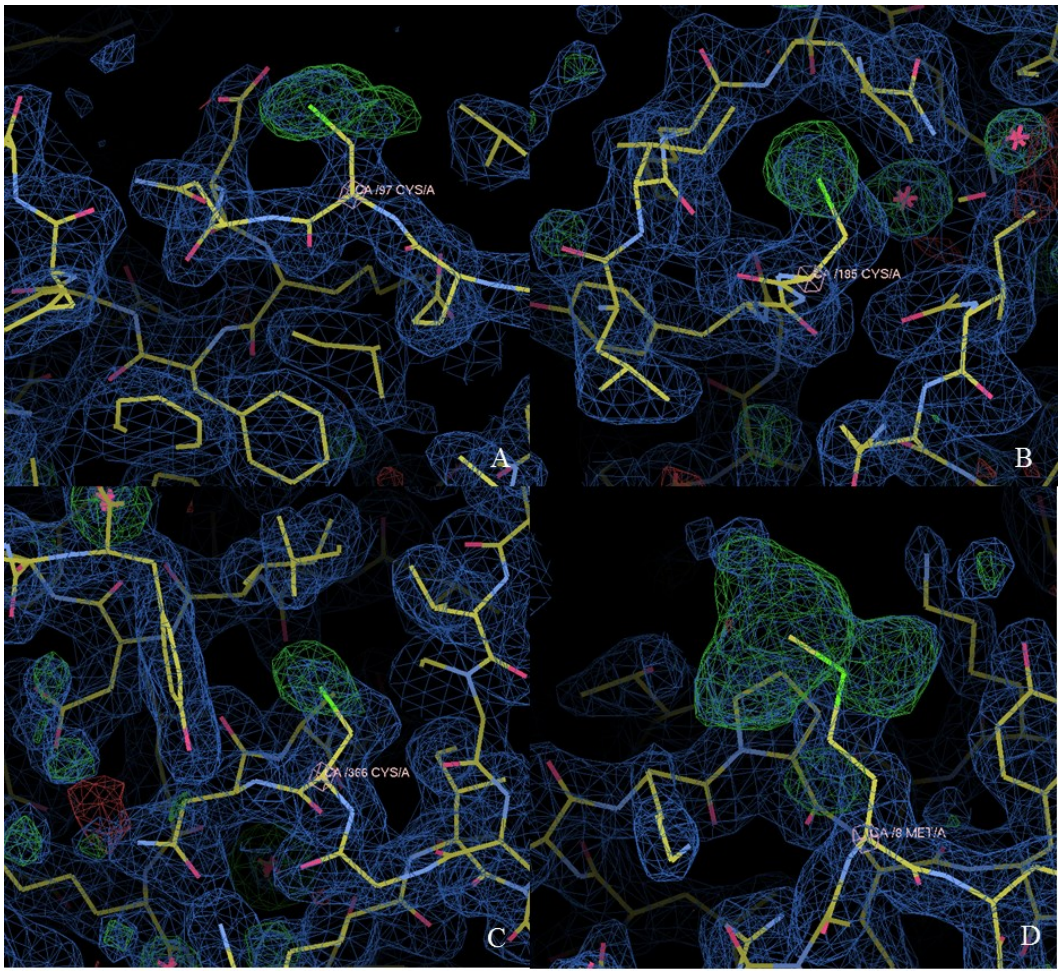

Figure 13: Pt-soaked CPILE-a. A–D, the electron density maps of Cys97, Cys185, Cys366, and Met8. Electron density maps for Pt atoms at the triple cysteine residues and the biggest |Fo-Fc| map was located at the methionine residue.

Structure of CPILE-a

CPILE-a is comprised of 419 amino acid residues and can be divided into two domains: the N-terminal domain (1-211) and C-terminal domain (212-419). The structures of the N-terminal domain and C-terminal domain of CPILE-a were quite similar even though the sequence identity was low (28.87%). The overall structure of CPILE-a was composed of two sets of β-strands and α-helices (Figure 14). The core structure of CPILE-a is constructed from five β-strands (four strands in N-terminal domain) and a set of three anti-parallel β-

sheets. Interestingly, there was a long loop at the junction between the N- and C-terminal domains. The arrangement of the N-domain was found to be α1, α2, α3, α4, β1, α5, α6, , β2, β3, β4, β5, β6, and β7 followed by α7, α8, α9, α10, β8, α11, α12, α13, β9, β10, β11, β12, α14, α15, β13, and β14 of the C-terminal domain. Moreover, there were three flexible loops that should be carefully investigated to determine their roles on actin binding, including loop I, protruding loop I (PT I), and protruding loop II (PT II) (magenta color in Figure 14).

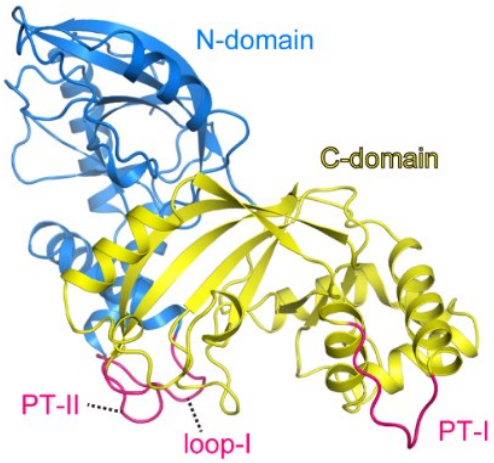

Figure 14: Crystal structure of CPILE-a. The overall structure of CPILE-a is composed of two sets of β-strands and α-helices. N-terminal domain (blue), C-terminal domain (yellow), loop I, PT I, and PT II (magenta).

A Ramachandran plot showed a 2-dimensional scatter plot of the φ-ϕ backbone torsion angle pairs for each residue of CPILE-a (Figure 15). The 402 amino acid residues were in the preferred region, and 11 residues and two residues were in the allowed and outlier regions, respectively.

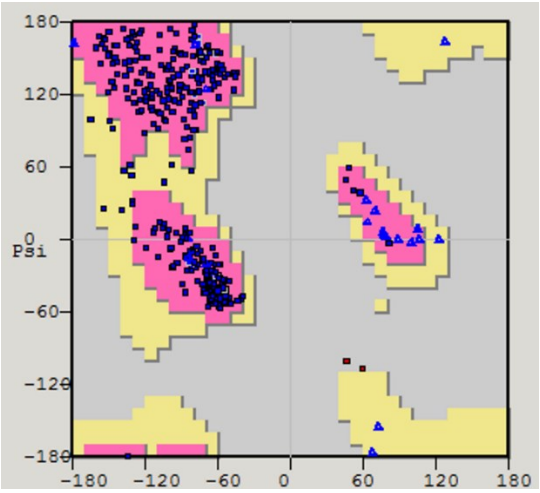

Figure 15: Ramachandran plot of CPILE-a. Most amino acid residues are in the β-region and right helical region. There are two outlier residues: Ala11 and Asn115.

To confirm that the structure of CPILE-a was solved correctly, the electron density map was captured at 1.09 rmsd. The amino acid residues fit well to the electron density map shown (Figure 16).

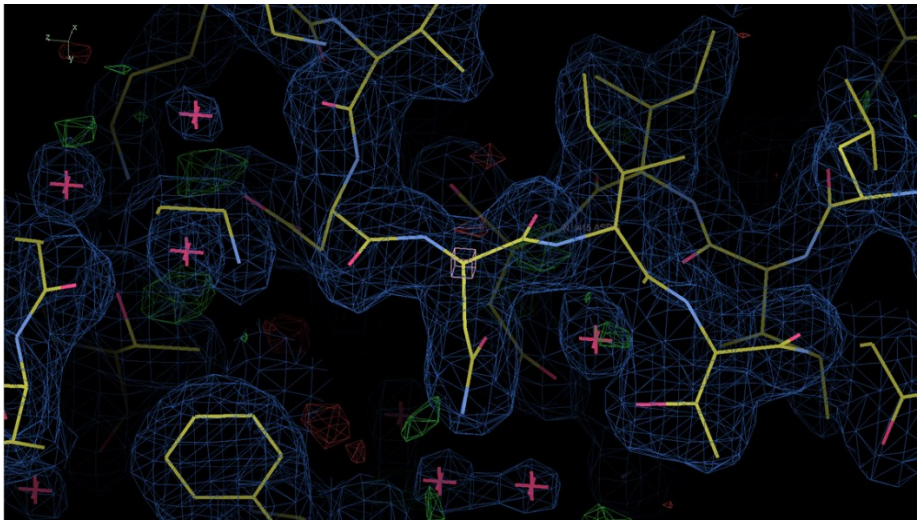

Figure 16: |Fo-Fc| map of CPILE-a at the 1.09 σ map contour level. Isoleucine residues fit to the electron density map are shown.

Comparison with Iota toxin (Ia)

1.1 Sequence comparison

On the basis of the family of amino acid residues at three positions essential for NAD-binding, ARTs can be divided into two major subclasses: ARTC (Clostridia toxin-like/ Cholera toxin-like) carrying the RSE triad motif and ARTD (Diphtheria toxin-like) carrying the HYE triad motif (Hottiger et al., 2010). Several studies have shown that the asparagine or arginine specificity is governed by the first Gln or Glu of the Q/ExE motif (Hara et al., 1996; Maehama, Hoshino, and Katada, 1996; Han et al., 2001; Vogelsgesang and Aktories, 2006). This residue is positioned two residues upstream of the catalytic Glu. It is also present in the variant R-S-E triad motif. CPILE-a and Ia belong to the ARTC subfamily.

The sequence alignment of CPILE-a and Ia show high identity and have similar residues, especially in the RSE triad motif, which are conserved between them (Figure 17). The RSE motif consists of three β-strands located in the C-terminal domain (yellow circle). The first aromatic-R on RSE motif is located between loop II and loop III. The STS motif is located between loop III and loop IV. CPILE-a has STT instead of the STS as in Ia. The EXE motif is located on the ARRT loop.

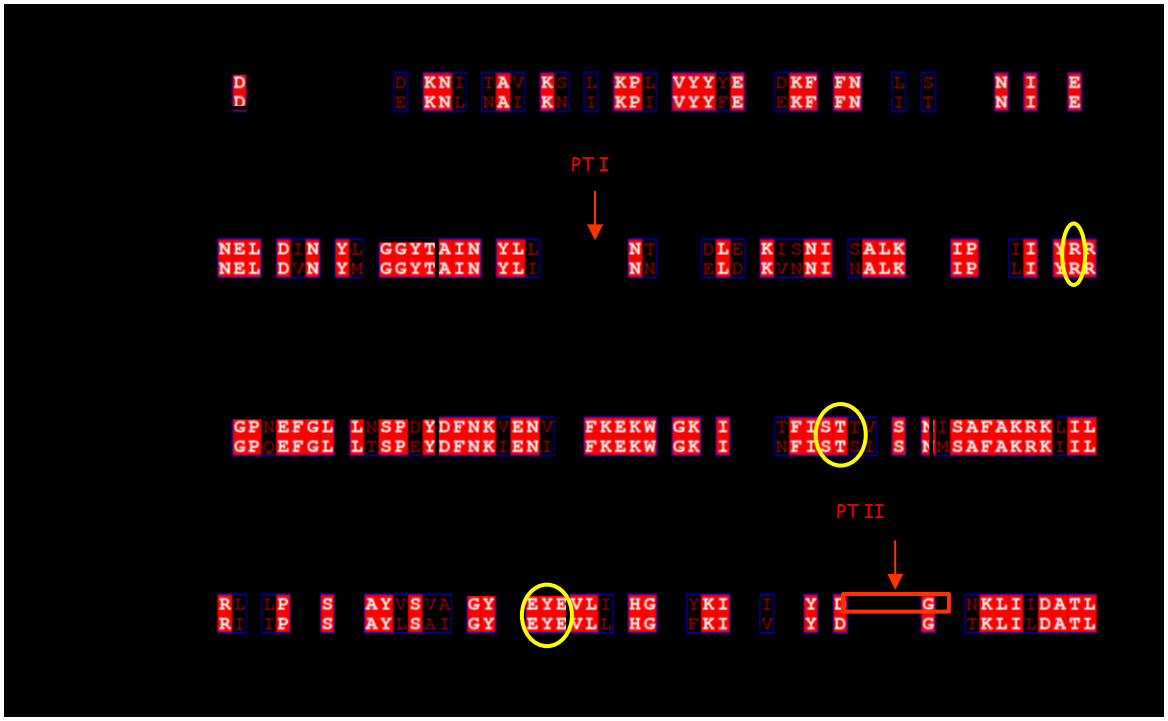

Figure 17: Sequence alignment of CPILE-a and Ia. The black boxes show actin-binding loops (I-V) based on the Ia–actin crystal structure. The Ia five loops are named loop I (Tyr61-Tyr62), loop II (active site loop), loop III, loop IV (PN loop), and loop V (ARTT loop) (Tsuge et al., 2008). Yellow circles represent the RSE triad motif.

1.2 Structural comparison

The overall crystal structure of CPILE-a is similar to that of Ia at the RMSD 1.56 Å of 360 amino acid residues compared. However, CPILE-a has two extra-long loops, including PT I and PT II, which represent a distinct difference from Ia (Figure 18). Those distinct loops are not located around the NAD binding cleft and probably do not affect NAD binding. Interestingly, the conformation of loop I of CPILE-a is different from that of Ia, which are important for actin binding. CPILE-a harbors Leu61, Asp62, and Asn63, whereas Ia has Tyr61, Asp62, and Tyr63. However, based on the structural difference between CPILE-a and Ia, several key residues of loop I, PT I, and PT II were selected and mutated for the ADP-ribosyltransferase study. The amino acid residues of interest were Leu61 and Asn63 from loop-I, Glu266Asn267 from PT-I, and Ser404 and Leu405 from PT-II.

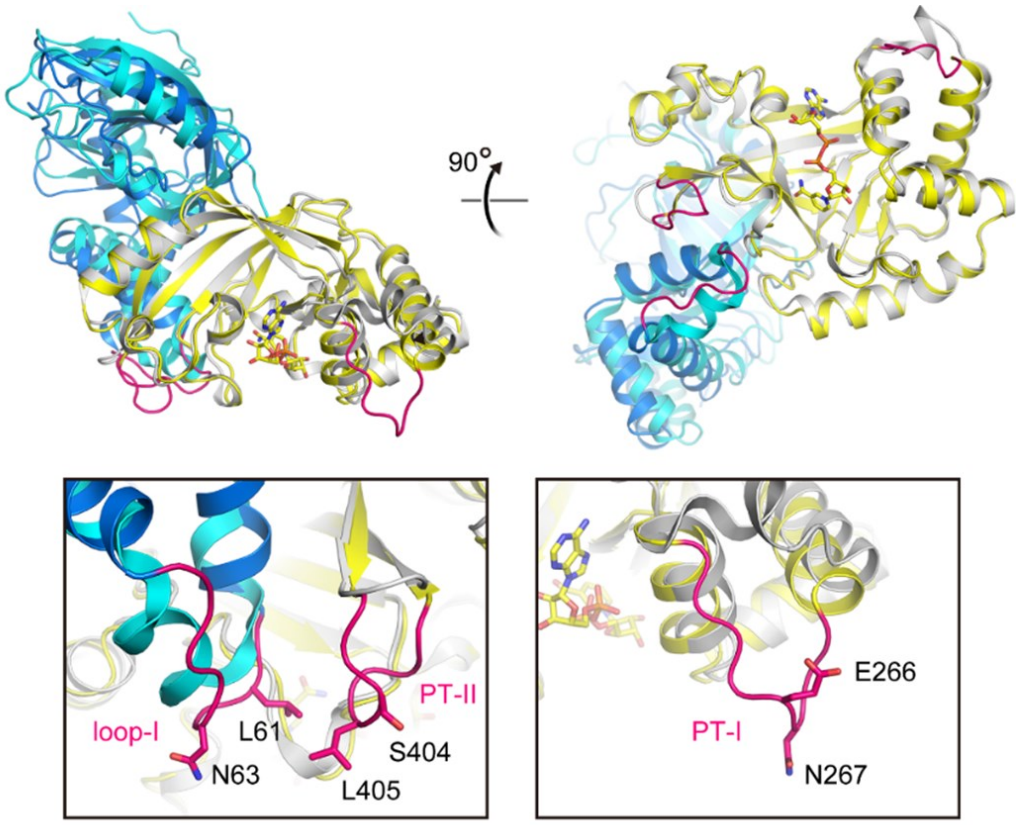

Figure 18: Structural comparison between CPILE-a and Ia. Superimposed structures of CPILE-a (5GTT) and Ia (4H03). The marine color represents the C-terminal domain, and the yellow color represents the N-terminal domain of CPILE-a, whereas the N-terminal domain and C-terminal domain of Ia are shown in cyan and white, respectively. NAD^+ is shown as a stick. Close-up views of loop-I and PT-II are on the left, and PT-I is on the right. Some of amino acid residues selected for the mutational study are shown as a stick.

Discussion and Conclusion

Structural determination of CPILE-a

At first glance, we faced the phase problem because of at least two space groups (*I*222 and *C*222) of the CPILE-a crystal. We could not solve the structure by MR. However, we overcame the phase problem on the third try by using MAD and SAD data sets of Hg-soaked CPILE-a. Compared with Ia, CPILE-a showed three distinct loops, including a short loop I and two protruding loops, I and II. In Ia, Tyr60 and Tyr62 of loop I interact with actin through an ionic bond and hydrogen bond, respectively (Tsurumura et al, 2013). In contrast, Tyr60 and Tyr62 of loop I in CPILE-a were substituted by Leu61 and Asn63, respectively. Therefore, loop I mutants were used to test the ADP-ribosyltransferase activity as described in chapter IV. Moreover, PT I and PT II mutants were also tested.

……

Chapter II

Structural analysis of NAD^+ and NADH-binding CPILE-a

NAD^+-binding and NADH-binding of CPILE-a

NAD^+ is a cofactor of ARTs whereas NADH is not. Therefore, CPILE-a and both substances were co-crystalized and analyzed. The NAD^+-CPILE-a and NADH-CPILE-a structures were solved at 1.80 Å and 2.26 Å, respectively. The NAD^+-CPILE-a data set was collected by using an NW-12A beamline in a KEK Photon Factory-Advanced Ring, whereas NADH-CPILE-a was collected in-house by using a MicroMax-007 generator and RAXIS VII X-ray diffractometer (Rigaku) at Kyoto Sangyo University. Both structures were solved by MR and wild-type CPILE-a as a structural model. Both of them belonged to the *I*222 space group and were one molecule in an asymmetric unit (Table 7).

Table 7: Data collection of NAD^+-CPILE-a and NADH-CPILE-a

Data collection	**NAD^+-CPILE-a**	**NADH-CPILE-a**
Space group	*I*222	*I*222
Cell dimensions		
a, b, c (Å)	70.0, 95.2, 125.1	70.6, 101.6, 125.3
a, b, g (°)	90.0, 90.0, 90.0	90.0, 90.0, 90.0
X-ray source	PF-AR NW 12A	MicroMax-007, RAXIS VII (RIGAKU)
Wavelength (Å)	1.00000	1.5418
Resolution range (Å)	50.00-1.80 (1.83-1.80)	50.00-2.26 (2.30-2.26)
Observed reflections	242720	127629
R_{meas}[a]	0.152 (0.844)	0.084 (0.408)
Rpim[b]	0.060 (0.370)	0.034 (0.169)
$CC_{1/2}$[c]	(0.655)	(0.948)
I / σI	12.3 (0.92)	41.3 (6.5)
Completeness (%)	99.4 (92.1)	98.4 (95)
Redundancy	6.3 (4.8)	6.0 (5.4)

[a] $R\text{meas} = \sum_{hkl}\{N(hkl)/[N(hkl)-1]\}^{\frac{1}{2}}\sum_i|I_i(hkl)-\langle I(hkl)\rangle|/\sum_{hkl}\sum_i I_i(hkl)$,

[b] $R\text{pim} = \sum_{hkl}\{1/[N(hkl)-1]\}^{\frac{1}{2}}\sum_i|I_i(hkl)-\langle I(hkl)\rangle|/\sum_{hkl}\sum_i I_i(hkl)$, where $I_i(hkl)$ are the observed intensities, $\langle I(hkl)\rangle$ is the average intensity and $N(hkl)$ is the multiplicity of reflection hkl.

[c] $CC_{1/2}$ = percentage of correlation between intensities from random *hkl*-data sets

The NAD^+-CPILE-a and NADH-CPILE-a structures were deposited as 5WTZ and 5WU0, respectively, in the Protein Data Bank (Table 8).

Table 8: Refinement statistics of NAD^+-CPILE-a and NADH-CPILE-a

Refinement	NAD^+-CPILE-a	NADH-CPILE-a
Resolution (Å)	47.61-1.80	23.48-2.25
R_{work}/R_{free} [d] (%)	19.0 / 23.8	17.7 / 24.8
Overall B factors ($Å^2$)	32.0	47.0
r.m.s.deviations		
Bond lengths (Å)	0.007	0.007
Bond angles (°)	1.124	1.166
Ramachandran plot		
Favored regions (%)	96.39	95.20
Allowed regions (%)	3.13	4.32
Outliers (%)	0.48	0.48
PDB ID	5WTZ	5WU0

[a] $R\text{work} = \sum_{hkl}||F_{obs}| - |F_{calc}||/\sum_{hkl}|F_{obs}|$. *R*free is the cross-validation R factor for the test set (5%) of reflections omitted from model refinement.

The superimposed structure of NAD^+-CPILE-a and NADH-CPILE-a showed that there were no distinct structural differences in the 356 amino acid residues compared between them at RMSD 0.232 Å (Figure 19).

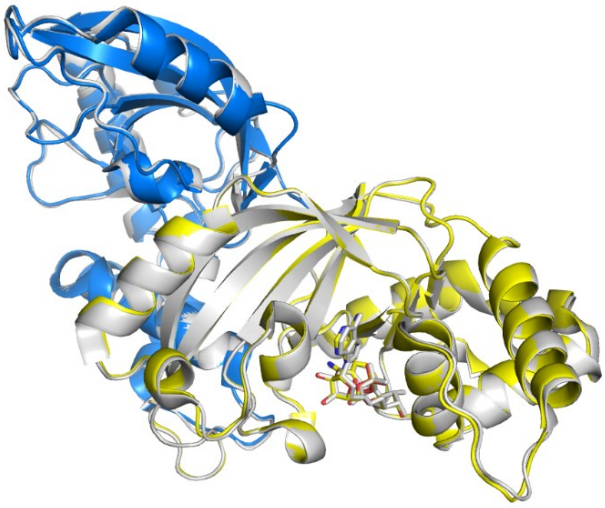

Figure 19: Superimposed structure of NAD^+-CPILE-a (5WTZ) and CPILE-a-NADH (5WU0). For NAD^+-CPILE-a labeled here, N-domain (marine blue); C-domain (yellow); NADH-CPILE-a (gray).

Figure 20 shows close-ups of the NAD^+- and NADH-binding sites of CPILE-a. No large structural difference in the NAD-binding site was seen between the two complex structures.

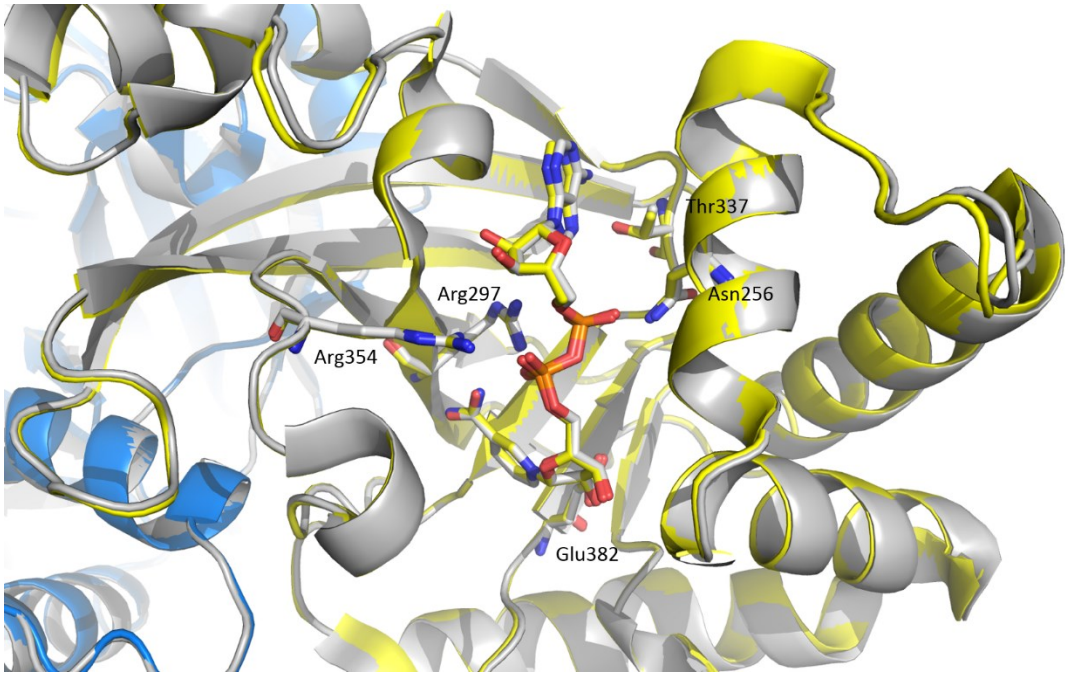

Figure 20: Closed up superimposed structure of 5WTZ and 5WU0. For NAD^+-CPILE-a labeled here, N-domain (marine blue); C-domain (yellow); NADH-CPILE-a (gray).

CPILE-a has hydrogen bonds with NAD^+ and NADH through the side chain of Asn256, Arg297, Thr337, Arg354, and Glu382 (Figure 20). The crystal structure of NAD^+-CPILE-a confirmed the location of the R (Arg297)-S (Ser340)-E (Glu382) motif around NAD cleft. Agr297 is located close to the O1N and O2N (N-phosphate) of NAD^+. As mentioned previously in chapter I, the second "S" of the STS motif was replaced by threonine in CPILE-a; thus, it did not seem to be very important to compare it with the first "S". Glu382 is the latter glutamate on the conserved EXE motif. The carbonyl and amide of the main chain Arg298 also fixed the nicotinamide in both the NAD^+- and NADH-binding structures.

Comparison with Iota toxin (Ia)

Superimposition of CPILE-a and Ia in the same direction of NAD^+ demonstrated that only 11 residues of CPILE-a form NAD^+ binding cleft, including Tyr252, Arg297, Arg298, Gly300, Asn302, Glu303, Thr337, Ser340, Thr341, Phe351, and Glu382. As we already described in chapter I, there were no large differences between CPILE-a and Ia except for loop I, PT-I, and PT-II. However, we noticed that there were some differences especially near the NAD-binding site, which caused moderate conformational differences even though the nine residues were conserved at RMSD 1.246 Å (Figure 21).

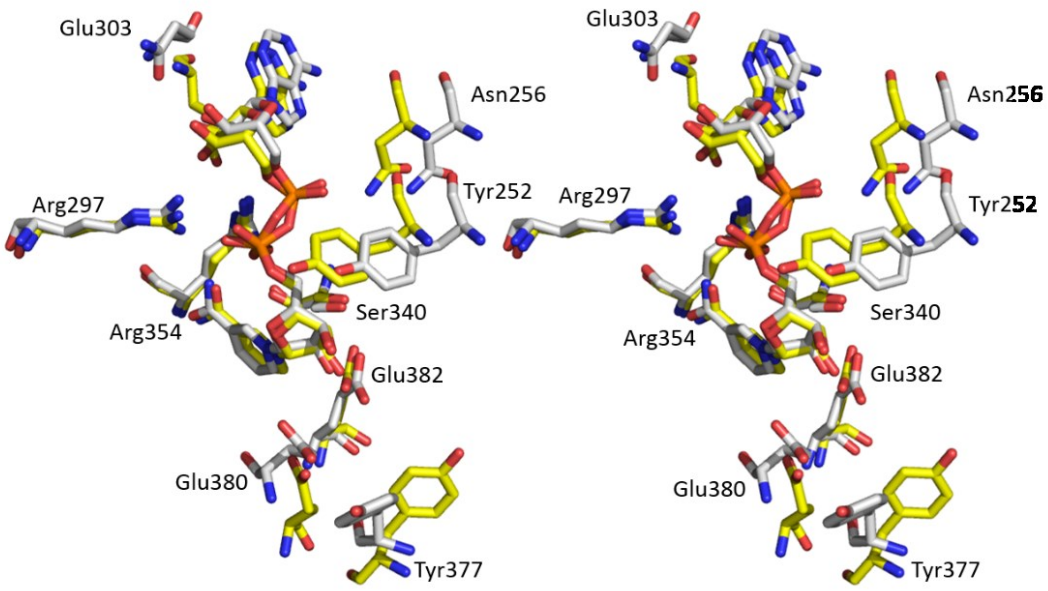

Figure 21: Comparison with NAD^+ binding site of CPILE-a and Ia. Stereo-view of NAD^+-CPILE-a (yellow) and NAD^+-Ia (4H03; gray) focused on the ligand-binding site (NAD^+). Nine residues represent the close-contact residues to NAD^+. All residues labeled here belong to NAD^+-CPILE-a.

In other words, although these nine residues around the NAD-binding site were conserved in the tertiary structures of Ia and CPILE-a, CPILE-a has a narrower NAD-binding pocket than that of Ia (Figure 22).

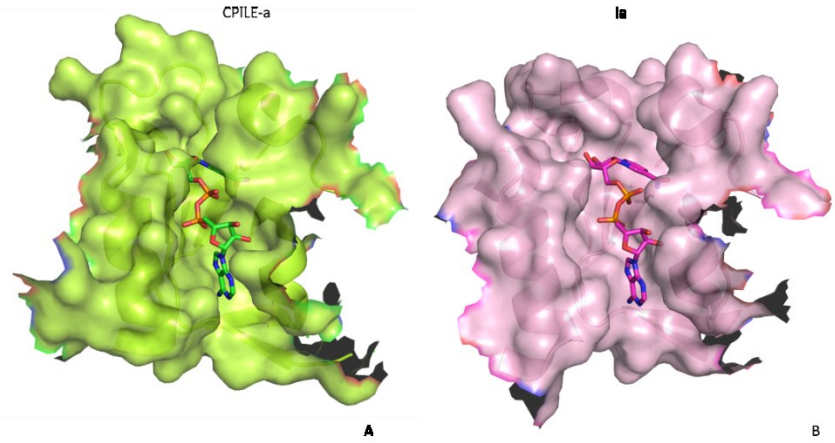

Figure 22: NAD binding pocket. A) NAD^+-CPILE-a showing a narrow NAD^+ binding pocket. B) NAD^+-Ia. Alpha helix 7 is located on the left side of the NAD molecule.

Discussion and Conclusion

NAD^+-binding and NADH-binding of CPILE-a

In the next Ligplot-like figure, we summarize the differences between CPILE-a and Ia around the NAD-binding site (Figure 23). For Ia (Figure 23B), we also added the results of the mutational study (Tsuge et al., 2003). It was known that Glu380 (Glu378 in Ia) and Glu382 (Glu380 in Ia) on the EXE motif were important residues for catalysis: the former glutamate (Glu380) is important for substrate residue recognition for ADP-ribosyltransferase (as will discussed in chapter VI: final discussion), whereas the latter glutamate (Glu382) is important for sharing a hydrogen bond with N-ribose (O2D) and for cleavage of nicotinamide-ribosyl bond (Oppenheimer, 1994; Han et al., 1999). Thus, Glu380 is a key amino acid for NADase, and Glu382 is a key amino acid for both NAD glycohydrolase and ADP-ribosyltransferase activities.

The two arginine, Arg297 (Arg295 in Ia) and Arg354 (Arg352 in Ia), support the phosphate groups of NAD. These residues did not appear to cause differences between the two structures. Interestingly, Asn256 of CPILE-a (Asn255 in Ia) has some contact with AO2 of the phosphate group. Asn256 is located on the α7 helix (252YTAINKYL259), and this alpha helix appeared to have moved slightly closer to the NAD molecule. This movement seems to cause the narrower binding pocket of CPILE-a than that of Ia. In the next chapter, we discuss the functional differences in NAD glycohydrolase activity between CPILE-a and Ia, which may be caused by this structural difference.

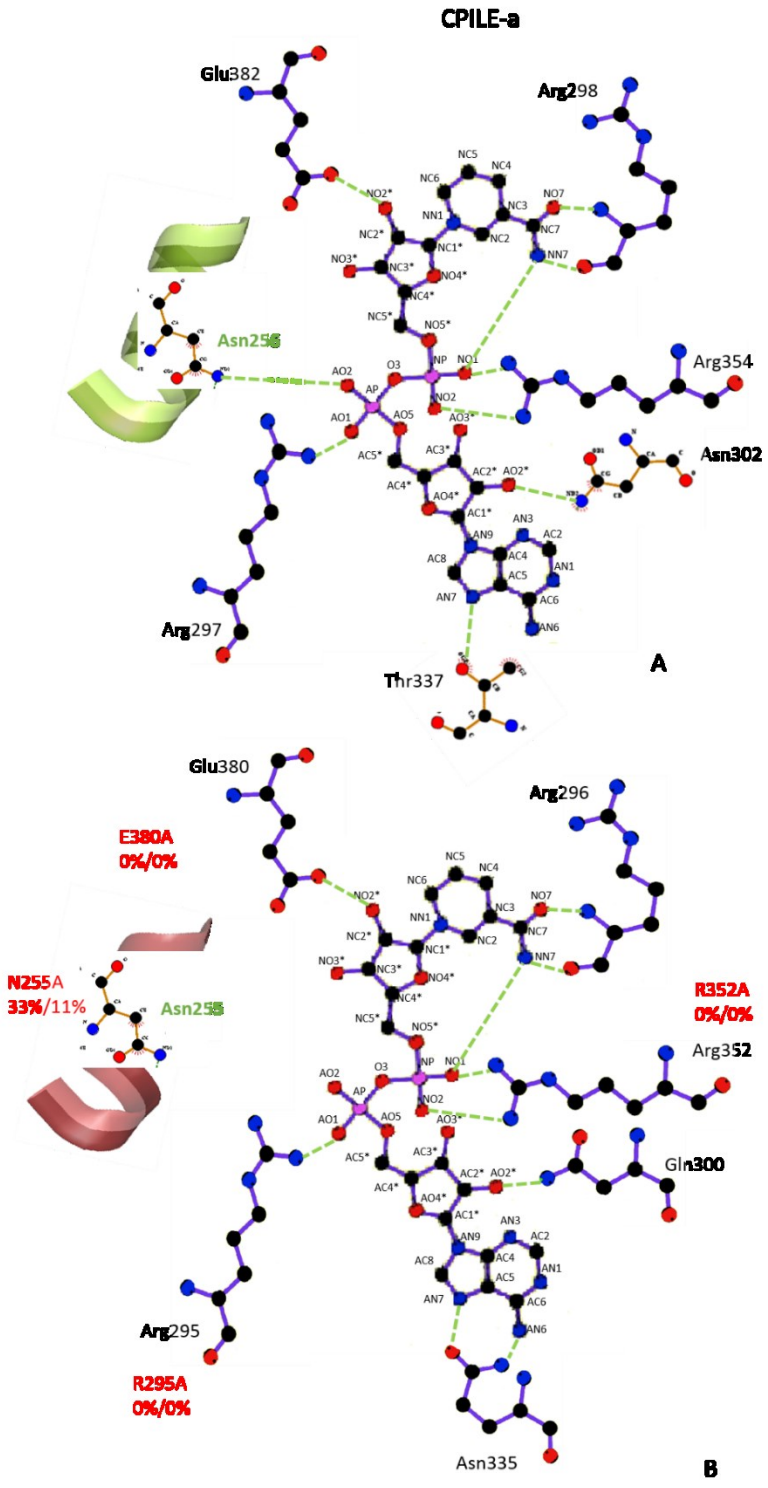

Figure 23: Schematic structure of the NAD binding site. A) NAD binding site of CPILE-a showing very close α7 helix and the location of Asn256 on the helix. B) NAD binding site of Ia showing distant α7 helix. The red label indicates the mutational study by Tsuge et al., JMB, 2003.

.....

Chapter III

Study of NADase activity of CPILE-a

NADase activity

Based on the structural similarity of the C-terminal domain with that of Ia, the two molecules should exhibit similar enzymatic activities. Despite having ADP-ribosyltransferase (ARTase), it is unclear if CPILE-a possesses NAD glycohydrolase (NADase). It is interesting to examine why Ia possesses both ADP-ribosyltransferase and NAD glycohydrolase and transfers the ADP-ribose moiety to different targets: actin and water. NADase hydrolyzes NAD into ADP-ribose and nicotinamide and then transfers the ADP-ribose moiety to a water molecule (Figure 24).

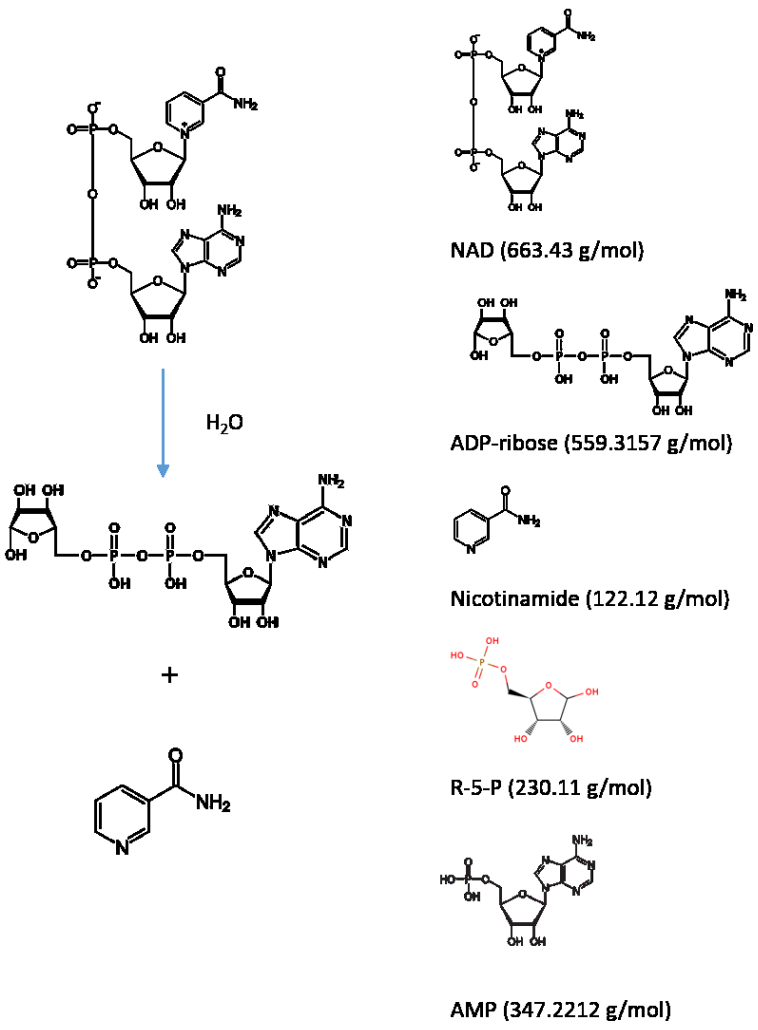

Figure 24: NADase reaction and possible substances derived from NAD hydrolysis.

Comparison with Iota toxin (Ia)

There were two purposes of this NADase assay: 1) to explore the NADase activity of CPILE-a and 2) to compare the NADase activities of CPILE-a and Ia under three conditions. The reactions were incubated at 37°C for 10 minutes and at room temperature for 1 hour or overnight. Figure 25A shows the reference peaks of βNAD$^+$, βNADH, ADP-ribose, AMP, and nicotinamide. It is interesting that ADP-ribose was the first substance eluted at approximately 1.5 minutes after injection followed by a double peak for βNAD$^+$ then a single peak for βNADH. Nicotinamide eluted at approximately4.0 minutes and AMP eluted at approximately 5.5 minutes.

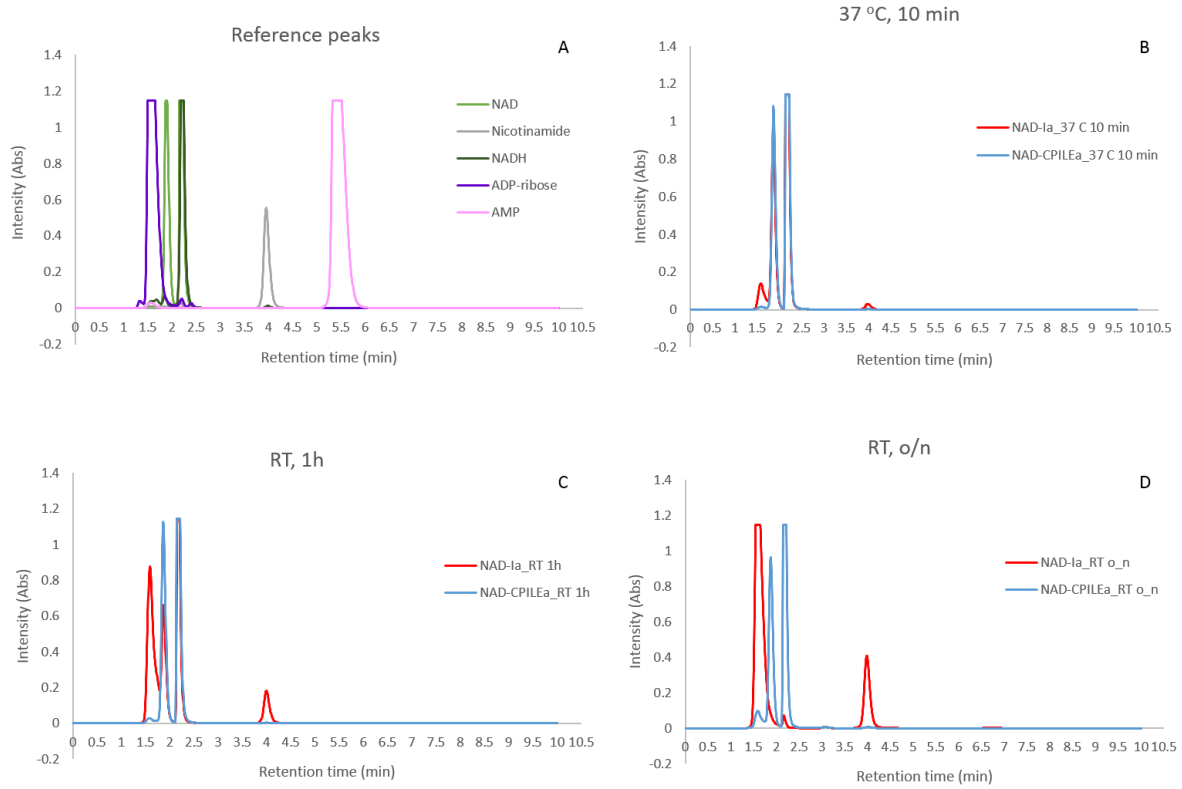

Figure 25: Chromatogram of NAD glycohydrolase activities of CPILE-a and Ia. A) Reference substances for NADase assay. All reference substances were loaded at 1 mM. B) NAD glycohydrolase activities of CPILE-a and Ia at 37°C, 10 min. C) NAD glycohydrolase activities of CPILE-a and Ia at 37°C, 10 min. D) NAD glycohydrolase activities of CPILE-a and Ia at room temperature, overnight.

The ADP-ribose and nicotinamide produced from the NADase assay showed that CPILE-a had almost no NADase activity even when incubated at room temperature overnight,

whereas Ia showed high NADase activity. It was unclear if CPILE-a cleaved NAD^+. Thus, a similar assay with actin was performed for both CPILE-a and Ia (Figure 26).

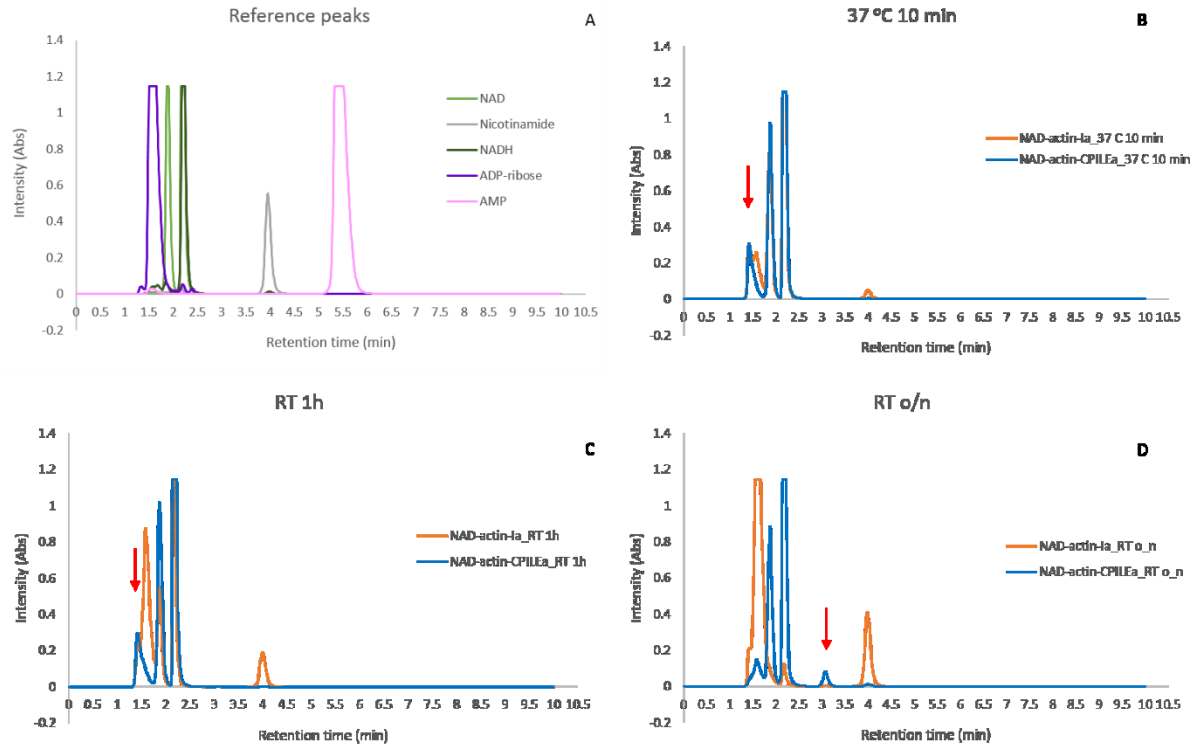

Figure 26: Chromatogram of NADase activities with actin of CPILE-a and Ia. A) Reference substances for **NADase** assay. All reference substances were loaded at 1 mM. B) **NADase** activities with actin of CPILE-a and Ia at 37°C, 10 min. C) **NADase** activities with actin of CPILE-a and Ia at 37°C, 10 min. D) **NADase** activities with actin of CPILE-a and Ia at room temperature, overnight. Red arrows indicate the unidentified peaks at 1.4 and 3.0 minutes.

Even with actin, the NADase activities of Ia showed a trend similar to that of the NADase activities. The amounts of ADP-ribose and nicotinamide increased with time. However, there was a difference in the NADase activities with actin between CPILE-a and Ia. Interestingly, the NADase activity with actin overnight of CPILE-a showed unidentified peaks at 1.4 minutes (Figure 26B, 26C and 26D) and 3 minutes (Figure 26D). It was unclear what these peaks represented. It is certain that actin affected the NADase activity of CPILE-a, and it is possible that actin triggered another reaction of CPILE-a. These unidentified peaks were collected and subjected to analysis by using mass spectrometry, but we were unable to identify the peaks.

Discussion and Conclusion

NADase activity

Irikura et al. (2015) reported the NADase activity at room temperature (6 hours) of rCPILE-a determined by LC/MS/MS. Nicotinamide released in a dose-dependent manner. However, our NADase assay showed that CPILE-a had almost no NADase activity even incubated at room temperature overnight, whereas Ia showed high NADase activity. The NADase activities between CPILE-a and Ia were much different. Furthermore, with actin, CPILE-a produced unknown products that were not seen in Ia with actin. The unidentified peak at 1.4 minutes (Figure 26B, 26C) decreased to a small peak, as shown in Figure 26D. Moreover, the unidentified peak at 3.0 minutes appeared when the reaction time was extended to overnight. Actin may induce some change in the NAD binding pocket and induce an unknown reaction. However, these products (1.4 minutes) were not stable and were transformed to another unidentified product (3.0 minutes). Further investigation regarding these observation is needed.

The site-directed mutagenesis of Ia showed the important roles of Arg295, Glu301, Arg352, Glu378, and Glu380 on NADase activity (Tsuge et al., 2003), and these residues were conserved in the tertiary structure. Based on the comparative structures of CPILE-a and Ia described in the previous chapter, we noticed one helix that included Asn256 was positioned closer to NAD and made a narrower pocket of NAD even though the two molecules have high sequence similarity. This helix is not only positioned near NAD but also related to actin binding, as shown in the Ia–actin structure. The positional difference of this helix may cause the difference in NADase activity without and with actin. Whether other factors, such as protein dynamics, are related to the catalytic difference unknown.

……

Chapter IV

Mutational studies of actin binding site in CPILE-a and Ia

General introduction

Actin is one of the most conserved proteins in eukaryote evolution and is involved in a variety of microfilament systems, such as muscle contraction, cell crawling, cytokinesis, cytoplasmic organization, and intracellular transport (Troys et al., 1999). These actins share 93.3% identity, and their secondary structures are also quite similar (Figure 27). It is interesting how bacterial ARTs recognize and distinguish between α-actin and/or β/γ-actin.

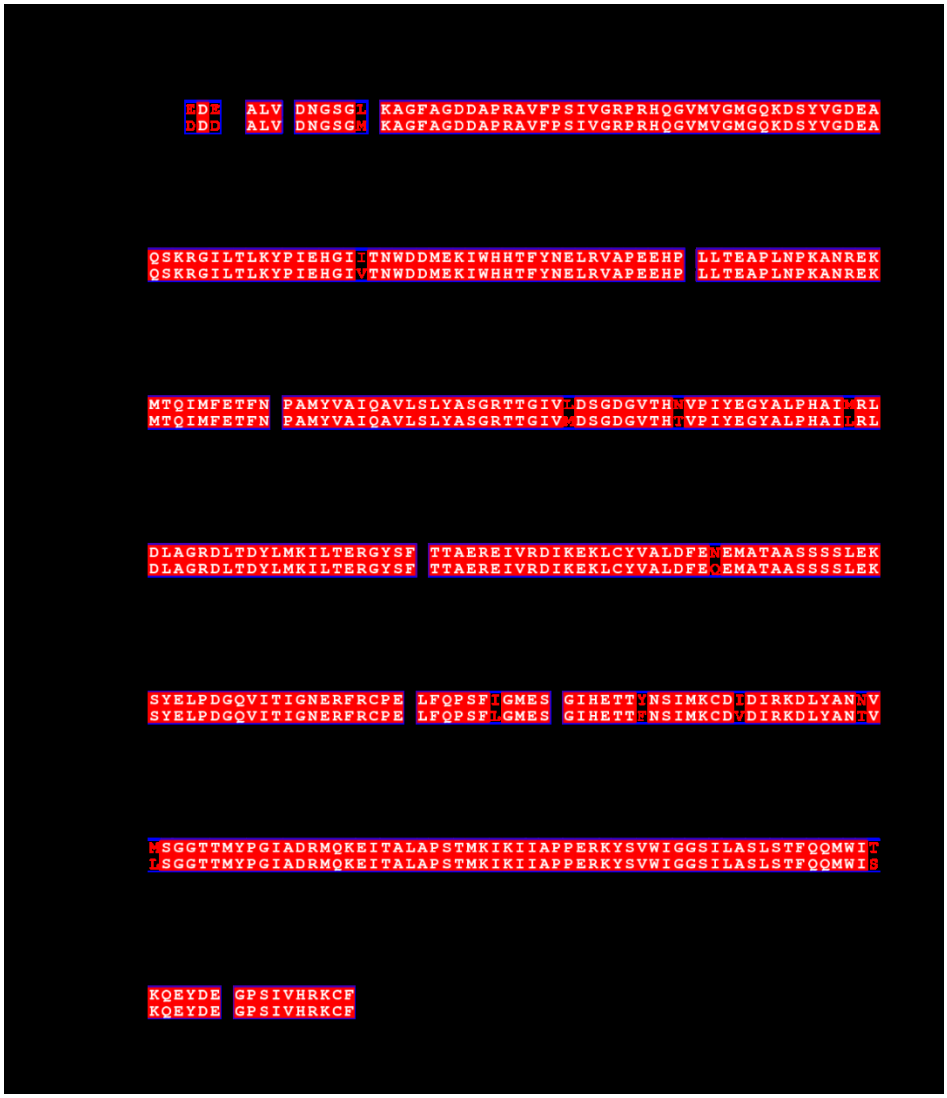

Figure 27: Sequence alignment of α-actin and β/γ-actin. Red boxes represent sequence identity, whereas the blue boxes represent sequence similarity. The figure was generated by using ESPript 3.0 after sequence alignment by Clustal Omega.

Actin is separated into two lobes by a deep cleft. Each lobe is composed of two subdomains (Figure 28). All domains contain a central β-sheet surrounded by a varying number of α-helices (Aktories et al., 2011). Both the N- and C-terminus are located in subdomain I. The target ADP-ribosylating Arg177 is located in subdomain III on the barbed end.

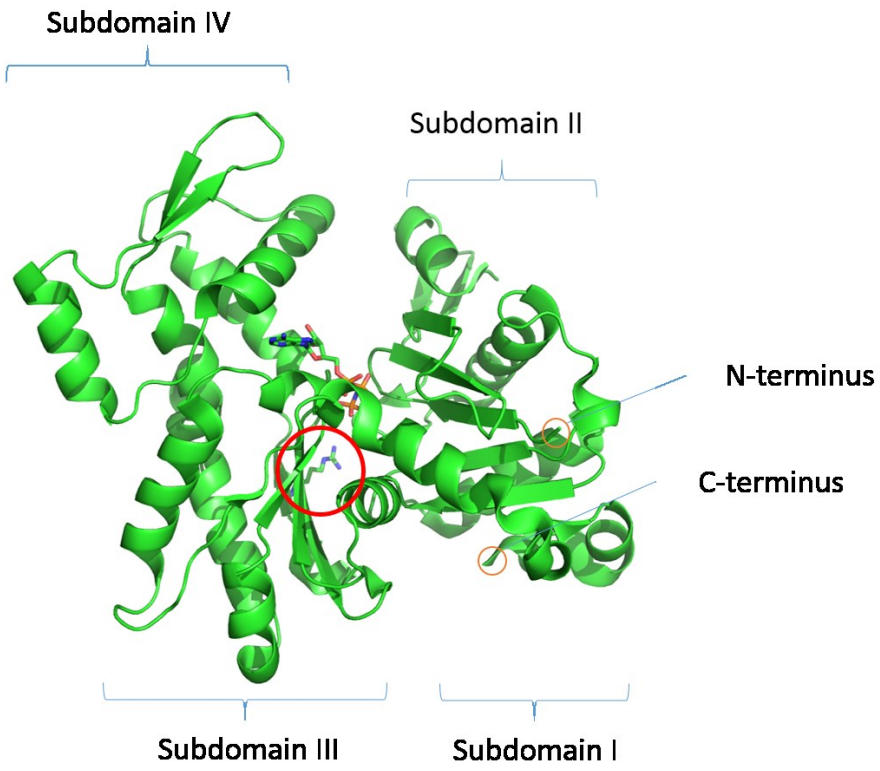

Figure 28: Structure of monomeric G-actin-ANP complex (1NWK). The red circle indicates Arg177, which is a target residue of ADP-ribosylating toxin. The orange circles the represent N- and C-termini. Modified from Aktories et al., 2011.

The sequence identity of α-actin and β-actin is very high (93.33%). Only twenty seven amino acid residues differ between α-actin and β-actin. It is interesting how CPILE-a can distinguish each type of actin, as will be described later. The ADP-ribosyltransferase activity of CPILE-a and CPILE-a-actin interaction were studied by using the Ia–actin complex structure as a model. At first, the recognition residues between Ia and actin were reviewed as they related to the crystal structure of the Ia–actin complex (4H03). Next, the CPILE-a-actin structure was modeled. Then, the selected key residues were mutated and their

roles on the ADP-ribosyltransferase activity were tested by using the fluorescein isothiocyanate (FITC) technique. Finally, the FITC results of the CPILE-a mutants were compared with Ia.

Ia–actin complex

In 2008, the complex structure of Ia–βTAD–actin had been reported (Tsuge et al., 2008). These complex structures provided insight into the actin binding site (Figure 29). Ia interacted with actin in subdomains I–IV through loops I–V. These five Ia loops were named loop I (Y61-Y62), loop II (active site loop), loop III, loop IV (PN loop), and loop V (ARTT loop), respectively (Tsuge et al., 2008; Sakurai et al., 2009). These loops located near the βTAD binding cleft were important for actin binding. It should be noted that most actin binding sites were in the C-terminal domain of Ia except that Y60-D61-Y62 belonged to loop I of the N-terminal domain. Furthermore, the Ia–actin complex also showed that the subdomain I, III, and IV of actin were close contact to Ia five loops.

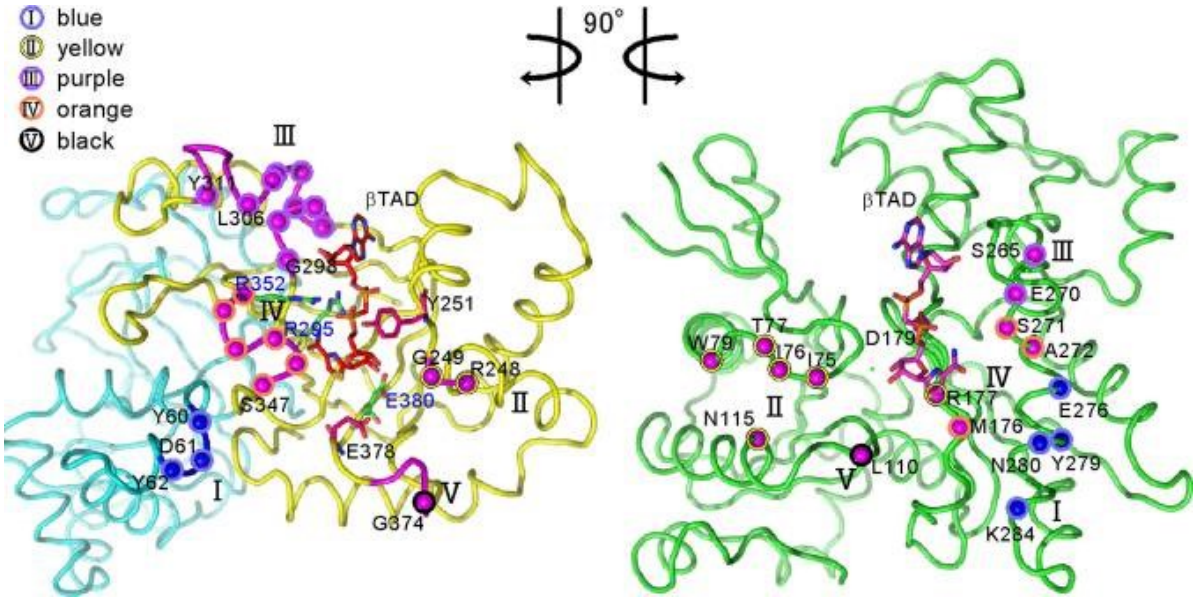

Figure 29: Butterfly representation of recognition residues between Ia and actin. Roman numerals (I-V) show the five binding loops in Ia. The actin-recognition residues on the five loops of Ia are shown as circles on the left. The catalytic residues of Ia around NAD (Tyr251, Arg295, Arg352, Glu378, and Glu380) are shown as sticks. The Ia-recognition residues of actin are shown as circles on the right. N-

terminal domain (Cyan); C-terminal domain (Yellow); Actin (Green). Source: Tsuge et al., (2008). PNAS 105, 7399-7404.

CPILE-a-actin model

How CPILE-a recognizes its target protein is unclear. Unfortunately, there is no known complex structure of CPILE-a-actin. However, Tsuge et al., 2008 showed that the structure of actin within the Ia-actin complex was relatively unchanged from its monomeric form. Thus, based on the crystal structures of Ia–α-actin (4H03), the CPILE-a-actin model was constructed. The CPILE-a-actin models were minimized by using Chimera 1.11. Therefore, the model of the CPILE-a–actin complex here was used as the template to investigate the recognition process of CPILE-a and its target proteins (α-actin and β-actin). This study focused on the interaction surface between CPILE-a and α-actin (Figure 30). It was interesting that CPILE-a shared most of its surface interaction with α-actin through the C-domain, similar to Ia. Moreover, it is expected that some part of the N-terminal domain was also associated in α-actin binding.

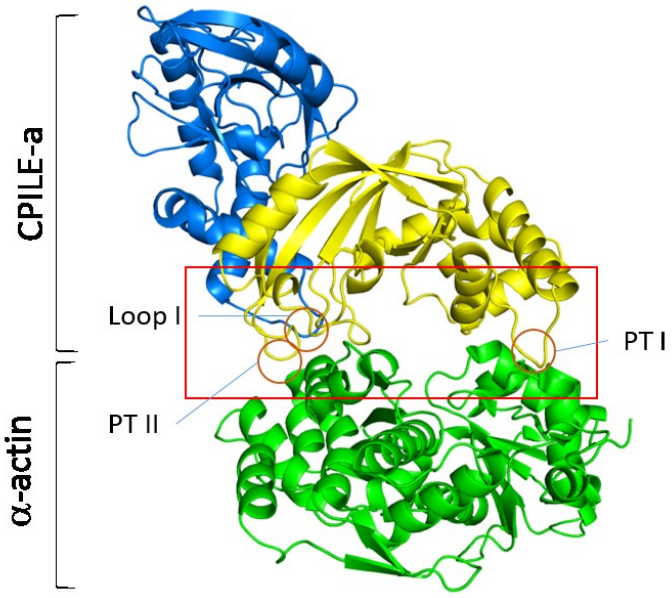

Figure 30: Model structure of CPILE-a-actin. The red square represents the interaction surface between CPILE-a and α-actin. (N-terminal domain (marine blue); C-terminal domain (yellow); α-actin, (green).

Focused residues of the actin binding site shown by the CPILE-a-actin model

In the CPILE-a-actin model, the interchain contacts were calculated by using the Contact program in CCP4 suite software (Bailey, 1994; Winn et al., 2011). The results showed that CPILE-a recognized subdomain III of α-actin through loop I (Table 9). Loop III of CPILE-a interacted with subdomain IV, whereas members of loop IV were in close contact with subdomains III and IV. Interestingly, both protruding loops were involved in the interaction between CPILE-a and α-actin. The interchain contact pattern of CPILE-a and β-actin was quite similar to the interaction between CPILE-a and α-actin. However, it should be noted that results from the Contact calculation showed that loop II of CPILE-a did not interact with α-actin nor with β-actin.

Table 9: The interchain contact of CPILE-a-α-actin and CPILE-a-β-actin using the Contact program in CCP4.

CPILE-a- α-actin			**CPILE-a-β-actin**		
	CPILE-a	**α-actin**		**CPILE-a**	**β-actin**
Loop I	L61 D62 N63 E65	E276, N280 K284 K284, M283, N280 M283, R290, Y279	**Loop I**	L61 D62 N63 E65	N280, C272 K284 N280, M283, K284 M283
Loop II	-	-	**Loop II**	-	-
PT I	N267	T66	**PT I**	-	-
Loop III	P301 L308 Y313	E270 E270, G268, M269 E270	**Loop III**	G300 P301 L308 Y313	E270 E270 G268, E270, M269 E270
Loop IV	S349 A350 F351 A352 K353 R354	S271, A272, E270, M176 S271, E270 E270 E270, S271, A272 E270, S271 E270	**Loop IV**	S349 A350 F351 A352 K353 R354	S271, C272, E270, L176 S271, E270 E270 E270, C272 E270, S271, C272, P264, S265 E270
Loop V	-	-	**Loop V**	E375 G376	K113 K113
PT II	S404 L405	E276 N280, A272, E276, G273,	**PT II**	S404 L405	E276 E276, C272, E270, N280,

	G406	T277 E276			G273

Mutational studies of actin binding site in CPILE-a and Ia

The sequence and structural alignment of CPILE-a and Ia showed a conserved triad motif. This finding indicated that CPILE-a might be capable of ADP-ribosylation at Arg177 of G-actin, as Ia did. According to the structure comparison of CPILE-a and Ia, CPILE-a might have ADP-ribosyltransferase activity similar to that of Ia. However, we do not know which interactions with actin are important. Thus, we selected 12 amino acid residues of CPILE-a and mutated them to study the effect of those mutants on ADP-ribosyltransferase activity (Figure 31). Moreover, nine residues of Ia were also selected to mutate and undergo further study.

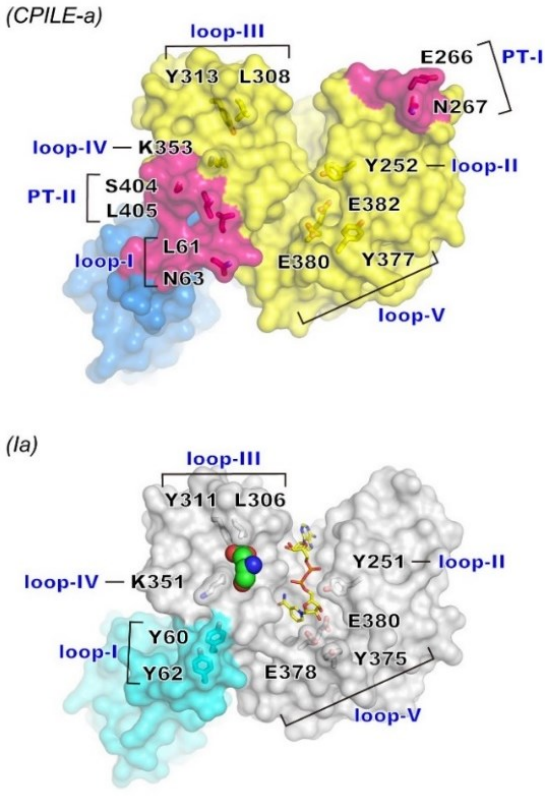

Figure 31: Actin interaction sites of CPILE-a and Ia. The amino acid residues of interest were selected for the mutational study. The side chain of Glu-270^{A} of α-actin is shown as a sphere in Ia.

The amino acids of interest were Leu61, Asn63 from loop I, Tyr252 from loop II, Leu308, Tyr313 from loop III, Lys353 from loop IV, and Tyr377, Glu380, Glu382 from loop V. Members of PT I and PT II of CPILE-a, including the double glycine mutants, Glu266, Asn267 and Ser404, Leu405 were mutated and studied. The mutants of Ia were selected as the similar sites of CPILE-a and included Tyr60 and Tyr62 from loop I; Tyr251 from loop II; Leu306 and Tyr311 from loop III; Lys351 from loop IV; and Tyr375, Glu378, and Glu380 from loop V.

FITC-assay of ADP-ribosyltransferase

To measure the ADP-ribosyltransferase activity against α-actin and β/γ-actin, both wild-type and mutants of CPILE-a and Ia were detected by using the FITC method (Figure 32). Briefly, biotin-NAD^+ interacted with the CPILE-a or Ia active site and was then cleaved to nicotinamide and the oxocarbenium cation. Next, the biotin–oxocarbenium ion was transferred to α-actin or β/γ-actin and the biotin-ADP-ribosylated actin was labeled by streptavidin-tagged fluorescein. The FITC results showed that wild-type CPILE-a exerted ADP-ribosyltransferase activity against α-actin and β/γ-actin; however, the sensitivity against β/γ-actin was one third that against α-actin. Ia also ADP-ribosylated both actin isoforms. The sensitivity against β/γ-actin was 55% of the sensitivity against α-actin.

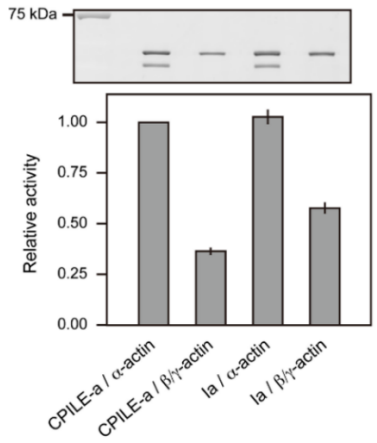

Figure 32: ADP-ribosylation assay of wild-type CPILE-a and Ia against α-actin and β/γ-actin. The top panel shows FITC-labeled α-actin and β/γ-actin. The α-actin bands are composed of native α-actin

(above) and protease-cleaved α-actin (below). Three independent experiments were performed and the error bar represents the S.D.

A comparison among the CPILE-a variants showed that most mutants affected ADP-ribosyltransferase activity against α-actin except for S404A and L405A (Figure 33). The ARTase activities of Y252A (loop II) and E266G/N267G (PT I) were drastically decreased against α-actin. On the other hand, these two mutants showed almost no effect against β/γ-actin. The selected loop III mutants (L308A and Y313A) had moderate effect against α-actin and less effect against β/γ-actin. The K353A mutant from loop IV showed drastically decreased ARTase activities against α-actin and β/γ-actin. Member of loop V influenced ARTase activities and had large effects on ARTase activity against α-actin. Mutants of catalytic glutamate had almost no ARTase activities against both actin isoforms.

A comparison of the Ia mutants showed that two mutants from loop I (Tyr60 and Tyr62) had large effects on ARTase activity against α-actin. Similar trends were found in the reaction against β/γ-actin, but showed lesser effects. Y251A (loop II) had a large effect on both actin isoforms. Mutants from loop III and loop IV had a moderate effect on both actin isoforms. Interestingly, mutants from loop V had large effects on ARTase activities against α-actin and β/γ-actin; especially E378S and E380S lost all of their enzyme activities.

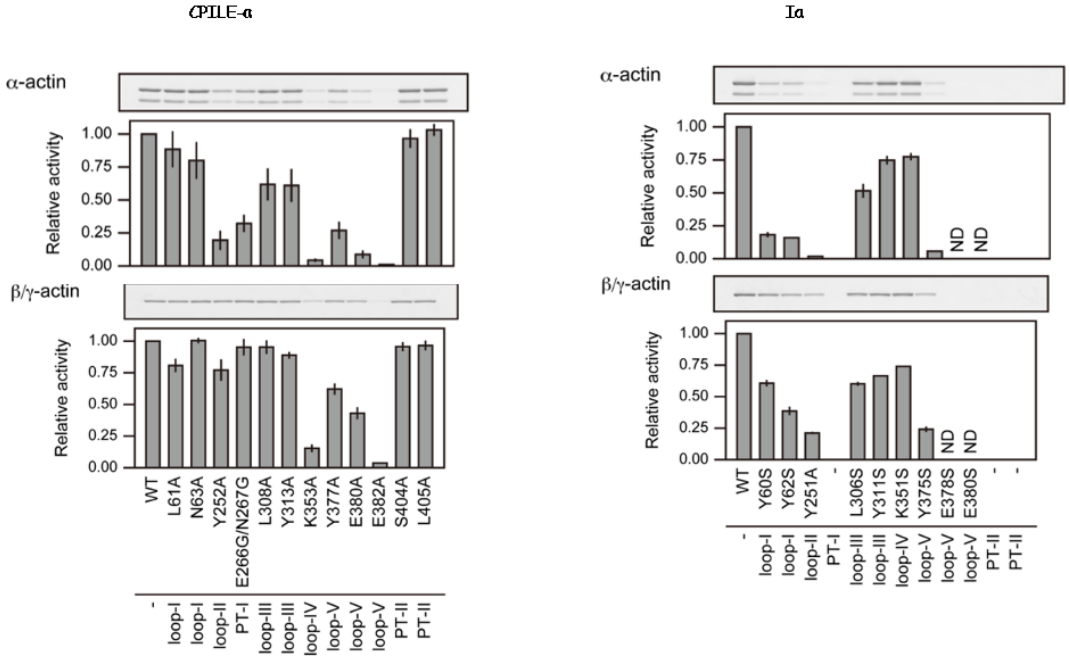

Figure 33: ADP-ribosylation assay of CPILE-a and Ia against α-actin and β/γ-actin. Comparison of the ADP-ribosylation activity of the wild-type and mutants. The ADP-ribosylation assay was performed by using biotin-NAD^+; then, the biotin-ADP-ribosylated actin was detected by streptavidin-FITC. Three independent experiments were performed and the error bar represents the S.D. In α-actin case, two bands were observed [α-actin (top) and protease cleaved α-actin (down)]. Thus each FITC- labeled actin from two bands are calculated and shown (white: non-cleaved black: cleaved).

In comparison with the Ia mutants, the CPILE-a mutants influenced the ARTase activities against α-actin and β/γ-actin; however, they demonstrated different profiles from that of Ia. Namely, CPILE-a mutants showed different ARTase activities pattern against α-actin and β/γ-actin. They have more sensitivity against α-actin than β/γ-actin. These FITC results suggested that CPILE-a preferred α-actin more than β/γ-actin as a substrate.

Discussion and Conclusion

Mutational studies of the actin binding sites in CPILE-a and Ia

In this study, FITC results showed differences in sensitivity and patterns between CPILE-a and Ia against α-actin and β/γ-actin. Regarding Ia's loop I, Tyr60 interacted with $E276^A$ through an ionic bond, shared a hydrogen bond with $N280^A$, and had a large effect on ARTase activity against α-actin (Tsuge et al., 2008; Tsurumura et al., 2013). CPILE-a harbored Leu61 and Asn63 instead of Tyr60 and Tyr62, which suggested a lower binding affinity of CPILE-a to actin relative to that of Ia.

Y252A had a large effect on ARTase activity against α-actin similar to that of Y251A of Ia (Tsuge et al., 2003). Interestingly, this CPILE-a mutant had little effect against β/γ-actin in contrast to the large effect of Ia. The role of this tyrosine in Ia and CPILE-a remains unknown. It should be noted that Tyr positions on the same α helix 7 (including Asn256), which have already been mentioned in the discussion on structural differences between Ia and CPILEa, which suggested that this α helix may have an important function for both NAD glycohydrolase and ADP-ribosyltransferase.

The double mutant from PT I showed a different pattern against actin isoforms, which indicated its role on α-actin recognition. Again, the members of loop III influenced ARTase activity against two actin isoforms in Ia. However, it showed a different pattern in CPILE-a.

Tsurumura et al., (2013) reported an ionic bond between Tyr311 and actin. However, this tyrosine residue seemed to recognize α-actin rather than β/γ-actin in CPILE-a.

The mutant from loop IV in CPILE-a showed a large effect against both actin isoforms in contrast to Ia, which indicated the important roles of this lysine residue in CPILE-a, probably on actin binding. Mutants of the catalytic glutamate had large effects on ARTase in Ia, similar to the results of previous studies (Tsuge et al., 2003), and in CPILE-a, they also showed almost no enzyme activity. However, the E380A of CPILE-a showed some activity against both actin isoforms. It was likely that this residue had a different role in the interaction between CPILE-a and Ia. According to the CPILE-a-actin model, Tyr377 seems to fit the shallow concave area as well as Tyr375 (φ) in the Ia–actin complex crystal structure (Toniti et al., 2017). Consequently, Y377A had a larger effect on ARTase activity. Together, these FITC results confirmed the important roles of this φ in actin binding. (It will be discussed in final discussion).

……

Chapter V

How does E49R mutation affect ADP-ribosylation in *I*222 crystal?

According to the constructed CPILE-a– α–actin model and the molecular packing of NAD^+-CPILE-a, Glu49 (E49) was located close to the NAD^+, and we assumed that it might be a ADP-ribose moiety acceptor in the crystal (Figure 33A). Thus, the E49R CPILE-a model was constructed (Figure 34B).

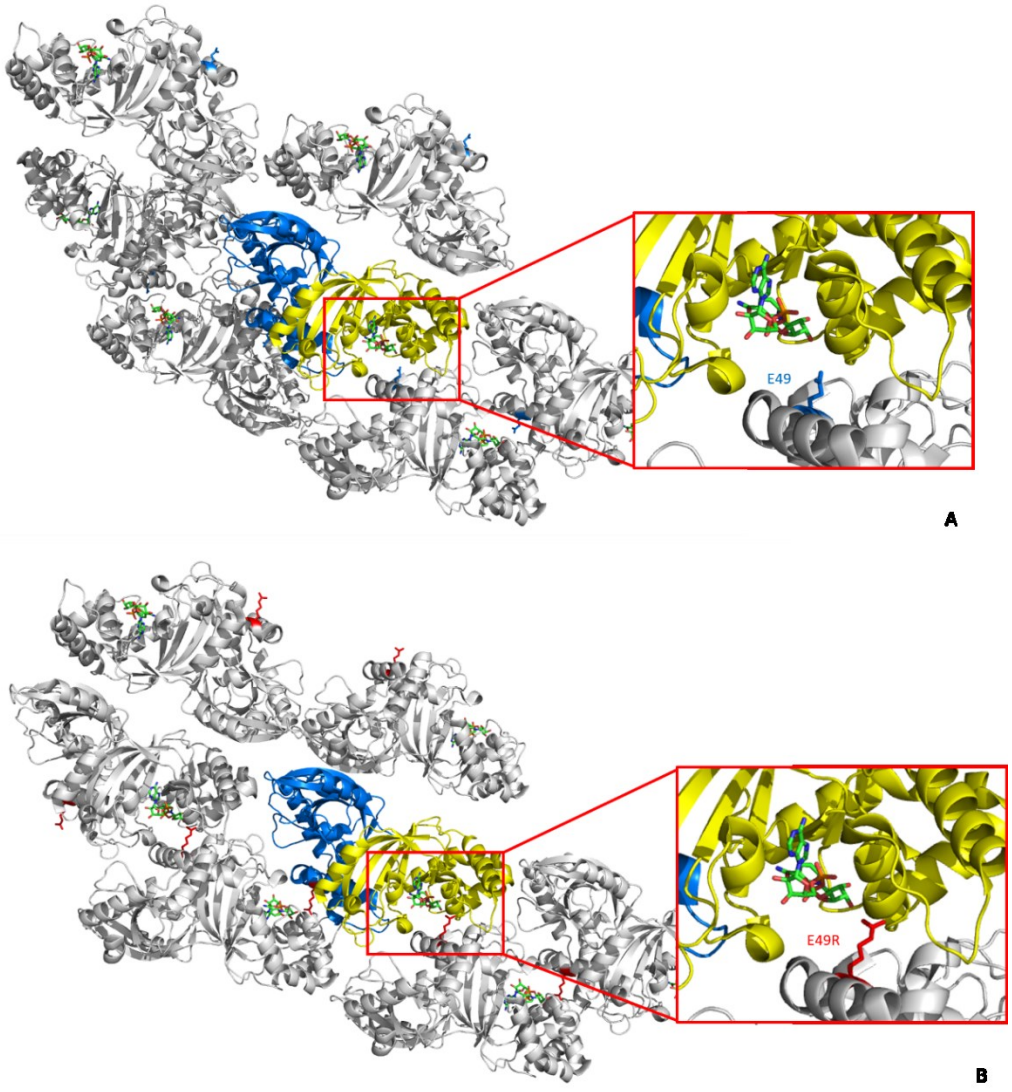

Figure 34: Crystal structure of the molecular packing of E49 CPILE-a (A) and model structure of E49R CPILE-a (B). A) The crystal structure of interest is colored as the wild type CPILE-a, whereas the neighbor molecules are gray colored. The E49 (marine blue) and NAD^+ are shown in the stick model. B) E49R CPILE-a of interest is colored as shown in A), whereas neighbor molecules are gray colored. NAD^+ is shown in the stick model. E49R is shown as the red stick.

To prove this hypothesis, the Glu49 residue was mutated to arginine. The E49R cpile-a/pGEX4T-2 was expressed and purified by following the same protocol as used for the wild-type and all CPILE-a mutants. The expression level and purity of E49R CPILE-a were not different from those of the wild-type CPILE-a.

First we checked that the FITC experiment failed to prove the hypothesis in solution (data not shown) and then we tried to see whether it possesses ADP-ribosylation activity on the adjacent molecule in the *I*222 crystal. Thus, the E49R CPILE-a purified was subjected to co-crystallization with 10 mM NAD^+ under the same conditions as those for the wild-type CPILE-a. Then, the selected trapezoidal-shaped crystals were picked up and soaked in 10 mM NAD^+ solution for 22 hours. The data set was collected at BL5A at the KEK Photon Factory (Table 10).

Table 10: Data collection of E49R.

Data collection	**E49R CPILE-a**
Space group	***I*222**
Cell dimensions	
a, b, c (Å)	70.1, 96.1, 125.2
a, b, g (°)	90.0, 90.0, 90.0
X-ray source	BL5A
Wavelength (Å)	1.0000
Resolution range (Å)	50.00-1.90 (1.93-1.90)
Observed reflections	200627
R_{meas}[a]	0.113 (0.939)
Rpim[b]	0.045 (0.474)
$CC_{1/2}$[c]	(0.799)
I / σI (%)	15.35 (0.82)
Completeness (%)	98.0 (72.8)
Redundancy	5.9 (3.3)

[a] $R\text{meas} = \sum_{hkl}\{N(hkl)/[N(hkl)-1]\}^{\frac{1}{2}}\sum_i|I_i(hkl)-\langle I(hkl)\rangle|/\sum_{hkl}\sum_i I_i(hkl)$,

[b] $R\text{pim} = \sum_{hkl}\{1/[N(hkl)-1]\}^{\frac{1}{2}}\sum_i|I_i(hkl)-\langle I(hkl)\rangle|/\sum_{hkl}\sum_i I_i(hkl)$, where $I_i(hkl)$ are the observed intensities, $\langle I(hkl)\rangle$ is the average intensity and $N(hkl)$ is the multiplicity of reflection hkl.

[c] $CC_{1/2}$ = percentage of correlation between intensities from random *hkl*-data sets

The E49R CPILE-a structure was solved at 1.88 Å by MR using 5WTZ as a search model. The E49R CPILE-a crystal structure belongs to a member of the *I*222 space group and consists of one molecule in an asymmetric unit.

Table 11: Refinement statistics of E49R.

Refinement	**E49R CPILE-a**
Resolution (Å)	1.885
R_{work}/R_{free}[a] (%)	19.5 / 26.1
r.m.s.deviations	
Bond lengths (Å)	0.007
Bond angles (°)	1.018
Ramachandran plot	
Favored regions (%)	95.43
Allowed regions (%)	4.09
Outliers (%)	0.48
PDB ID	-

[a] $R\text{work} = \sum_{hkl}||F_{obs}| - |F_{calc}||/\sum_{hkl}|F_{obs}|$. *R*free is the cross-validation R factor for the test set (5%) of reflections omitted from model refinement.

The overall structure of E49R CPILE-a was not much different from the template at RMSD 0.149 for 359 amino acid residues (Figure 35). The NAD^+ of both structure fit to the NAD cleft in the same configuration. The Ramachandran outliers of the E49R CPILE-a were Ala11 and Glu215 the same as 5WTZ.

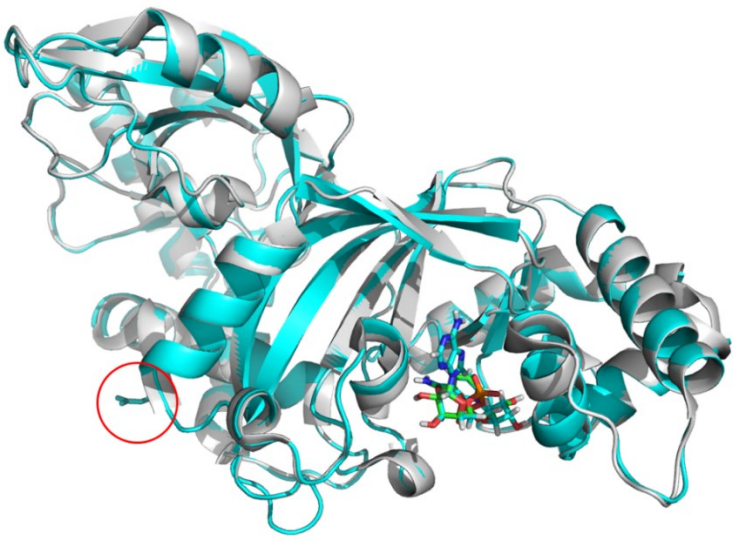

Figure 35: Superimposed structure of 5WTZ and E49R CPILE-a. 5WTZ is shown in gray, whereas E49R CPILE-a is in cyan. The NAD^+ fits in the NAD cleft. The E49R mutant is shown in the stick model (red circle).

The crystal structure demonstrated that there was no evidence of ADP-ribosylation of the adjacent Arg49 residue even if they were close enough to transfer the ADP-ribose moiety (Figure 36). The Arg49 of interest shared hydrogen bonds with O2 and NC1 of the neighboring NAD^+ at distances of 3.66 Å and 3.81 Å, respectively. Moreover, the Arg49 of interest shared another hydrogen bond with the water molecule nearby. Again, the expansion of the cell symmetry confirmed the FITC result that E49R CPILE-a failed to transfer the ADP-ribose to the adjacent molecule.

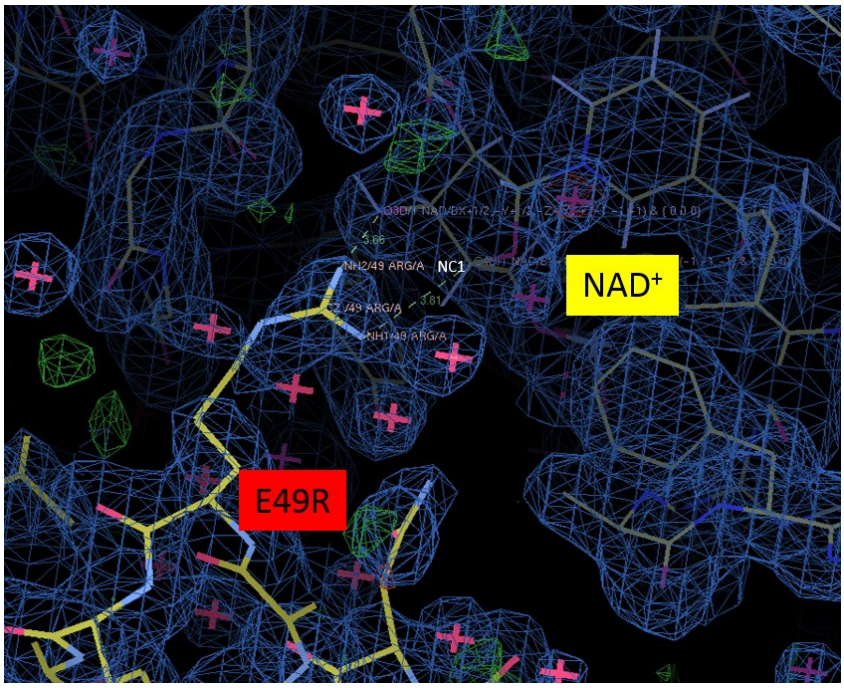

Figure 36: Structures of E49R CPILE-a and the adjacent NAD^+ molecule. The electron density maps of E49R CPILE-a are set at 2Fo-2Fc = 1.00 and Fo-Fc = 3.05 rmsd, respectively.

Figure 37 shows a representation of the molecular packing of E49R CPILE-a. The structure of E49R CPILE-a of interest is located at the center. This structure is represented by the same color as that used for the wild-type CPILE-a. Marine blue represents the N-terminal domain and yellow represents the C-terminal domain. The neighboring structure is shown in purple. The crystal structure shows the close contact between E49R and the NAD^+ of the neighbor.

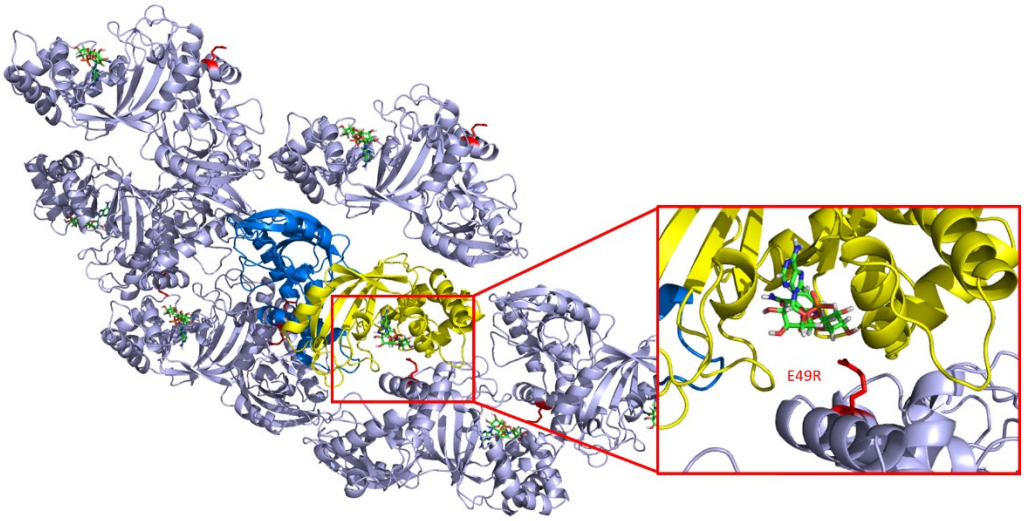

Figure 37: Crystal structure of the molecular packing of E49R CPILE-a. The crystal structure of interest is colored as the wild-type CPILE-a, whereas neighbor molecules are purple colored. NAD^+ is shown in the stick model. E49R is shown as a red stick.

Discussion and Conclusion

E49R as a model of ADP-ribosylation in the I222 crystal

Even though E49R CPILE-a failed to transfer the ADP-ribose to the adjacent molecule, the ARTase activity against actin was not affected by the E49R mutant. This mutant showed activities against α-actin and β/γ-actin similar to the wild-type. Moreover, the E49R crystal structure was not much different from the wild-type. On the basis of the FITC results and the crystal structure of E49R CPILE-a, we concluded that E49R CPILE-a failed to transfer the ADP-ribose to the adjacent molecule. This topic will be further discussed in chapter VI.

……

Chapter VI

Final discussion and Conclusion

Structural comparison of CPILE-a and Ia

Recently, the newly discovered enterotoxins were studied by two different groups and named binary enterotoxin of *C. perfringens* (BEC) and *C. perfringens* iota-like enterotoxin (CPILE), respectively (Yonogi et al., 2014; Monma et al., 2015; Irikura et al., 2015). It should be noted that CPILE (Monma's group) was presented at the 87th Annual Meeting of the Japanese Society for Bacteriology in 2013 and the 8th International Conference on the Molecular Biology and Pathogenesis of the Clostridia-ClostPath in the same year. In addition, BEC was studied by Yonogi's group, and some characteristics of BECa and BECb were published in 2014. However, the results of a BLAST search indicated that the sequences of *cpile* and *bec* matched. This BLAST result indicated that CPILE and BEC were identical toxins (Irikura et al., 2015). Our CPILE-a structures (apo-CPILE-a, NAD^+-CPILE-a, and NADH-CPILE-a) were compared with the crystal structures of apo-BECa and NADH-BECa that had been published by Yonogi's group recently (Kawahara et al., 2016).

Among all of the structures compared, only that of NADH-BECa (5H04) showed a large conformational change in the ARTT loop: the Tyr377 on the ARTT loop pointed away from the NAD binding cleft (Figure 38 and Table 12), which indicates the flexibility of the ARTT loop rather than of the natural structure. However, this flexibility of the ARTT loop did not seem to reflect the actin complex structure. The Tyr377 of the ARTT loop was thought to be an important residue in complex formation with actin, as described below.

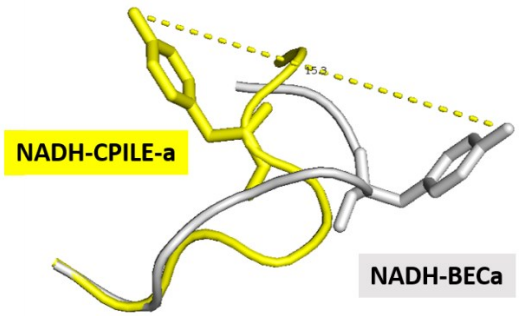

Figure 38: Graphic structure of the ARTT loops of 5WU0 (yellow) and 5H04 (gray). Tyr377 of BECa is 15.3 Å away from the same residue of CPILE-a.

Table 12: Structural comparison between CPILE-a and BECa (focus on the ARTT loop; V373-E380). Source: Toniti et al., (2017).

	5GTT	5WTZ	5WU0	5H03	5H04
5GTT	-				
5WTZ	0.38 (6)	-			
5WU0	0.58 (7)	0.20 (8)	-		
5H03	0.76 (8)	1.31 (8)	1.35 (8)	-	
5H04	3.02 (8)	2.74 (8)	2.68 (8)	3.28 (8)	-

RMSD (Å) and number of the Cα compared in the parenthesis.
5GTT: apo-CPILE-a, 5WTZ: NAD+-CPILE-a, 5WU0: NADH-CPILE-a, 5H03: apo-BECa, 5H04: NADH-BECa

φ Convex–concave interaction on the ARTT-loop

The crucial role of the bipartite ADP-ribosylating toxin turn-turn (ARTT) motif on substrate amino acid recognition of C3 exoenzyme was proposed by Han et al. (2001). The consensus sequence for the ARTT motif is φ X-X-(E/Q)-X-E, where φ represents an aromatic residue and has a role in substrate selection (Han et al., 2001). Moreover, the E/Q on the second loop is important for target residue recognition.

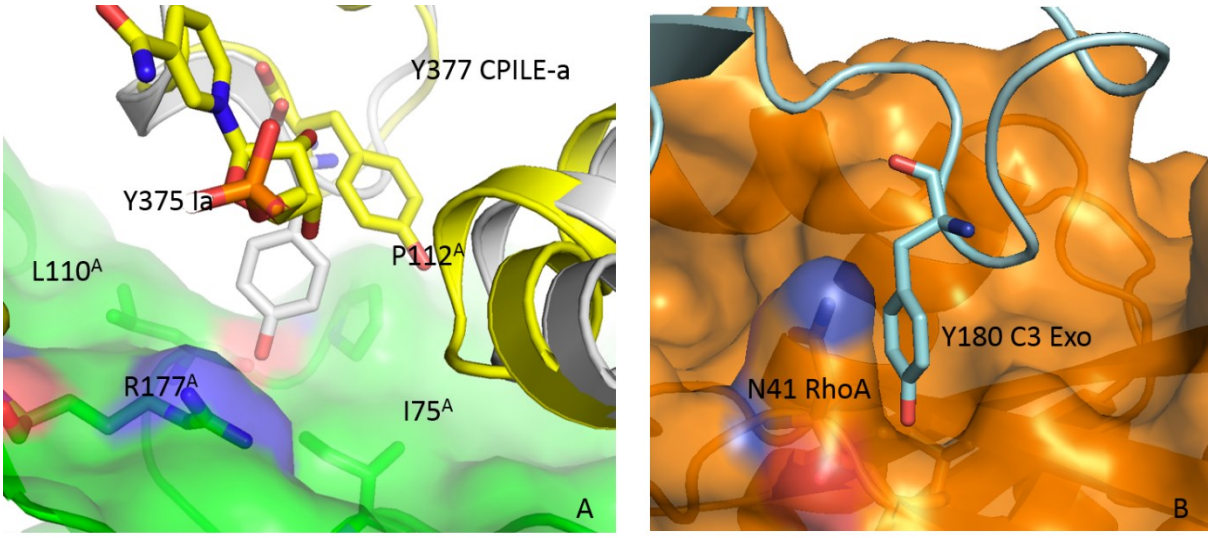

Figure 39: Convex–concave in focus. A) Model structure of CPILE-a-actin complex (CPILE-a; yellow, actin; green, Ia; gray). B) Complex structure of C3 Exoenzyme-RhoA (C3; Aquamarine, RhoA; Oranges).

In comparison with Tyr375 of Ia, the Tyr377 CPILE-a was positioned above the shallow concave area involving Leu110^{A}, Arg177^{A}, Ile75^{A}, and Pro112^{A} (Figure 39A). This Tyr377 should be a positional change upon actin binding. In C3 exoenzyme, the Tyr180 of C3 points toward the deep convex area of RhoA adjacent to the Asn41 (Figure 39B). Based on the mutagenesis of this study, it was concluded that the φ convex–concave interaction is one of the most important interactions required for formation of a complex with actin.

ADP-ribosyltransferase substrate recognition

The ADP-ribosyltransferase substrate recognition can be categorized into two concepts: protein–protein selection and protein–substrate amino acid recognition. The classic examples in ARTC members carry the RSE triad motif: CPILE-a/Ia ADP-ribosylates actin at Arg177 and C3 ADP-ribosylates RhoA at Asn41. In protein–protein selection, each toxin selects actin and RhoA as a protein substrate, respectively. How CPILE-a/Ia selects its protein substrate can be explained by the structure analysis of the Ia–actin complex and the mutagenesis studies of CPILE-a and Ia in this study.

As mentioned previously, the φ convex–concave interaction on the ARTT loop is one of the major interactions for substrate binding. However, it remains unclear how CPILE-a and Ia distinguish between α-actin and β/γ-actin. More complex structural analysis of, e.g., CPILE-a–actin, may lead to better understanding of this phenomenon. On the other hand, the C3–RhoA complex structure revealed that C3 recognized RhoA via switch I, switch II, and interswitch regions (Toda et al., 2015),and they also succeed in making the Cdc2 mutant an active substrate, as determined from structural information.

In protein–substrate amino acid recognition, each toxin recognizes arginine and asparagine as separate targets of ADP-ribosylation. The ARTT loop is located in one of the conserved triad motifs, the Q/EXE motif. It has been proposed that the first glutamine (C3) or glutamate (CPILE-a/Ia) is a key amino acid residue that is crucial for selecting and recognizing the target residue (Han et al., 2001). The role of this residue on target amino acid residues has been studied for a long time but it has not been confirmed directly (Cassel and Pfeuffer, 1978; Iglewski et al., 1978; Aktories et al., 1986; Maehama, Hoshino, and Katada, 1996; Han et al., 1999; Han et al., 2001; Hochmann et al., 2006; Margarit et al., 2006; Vogelsgesang and Aktories, 2006; Tsuge et al., 2008).

In 2006, Vogelsgesang and Aktories reported that the Q217E exoenzyme C3 (EXE C3) of *Clostridium limosum* failed to modify its natural substrates, RhoA or poly-L-asparagine. On the other hand, it turned to be an arginine–modifying enzyme. This EXE-C3lim modified poly-L-arginine and soybean trypsin inhibitor (SBTI). The SBTI was a model substrate for many arginine-specific ADP-ribosyltransferases. They concluded that an asparagine-ADP-ribosylating enzyme can be changed into an arginine-modifying transferase by exchanging one amino acid residue located in the catalytic site of the ARTT loop. They changed asparagine in RhoA to arginine and tested whether EXE-C3 was able to modifyAsn41Arg- RhoA, but they found that it did not.

Recently, the role of glutamine in target recognition has been confirmed by the complex structure of C3-RhoA (Toda et al., 2015). They demonstrated that Gln183 of C3cer shared hydrogen bonding on the Asn41 of RhoA and showed the conformational plasticity of the ARTT loop (Toda et al., 2015; Tsuge, Yoshida, Tsurumura, 2015). On the other hand, we have no direct evidence of Ia–actin structure (even pre- and post-ADP-ribosylation structures), but we expect that there should be such interaction in an intermediate structure of ADP-ribosylation (Figure 40).

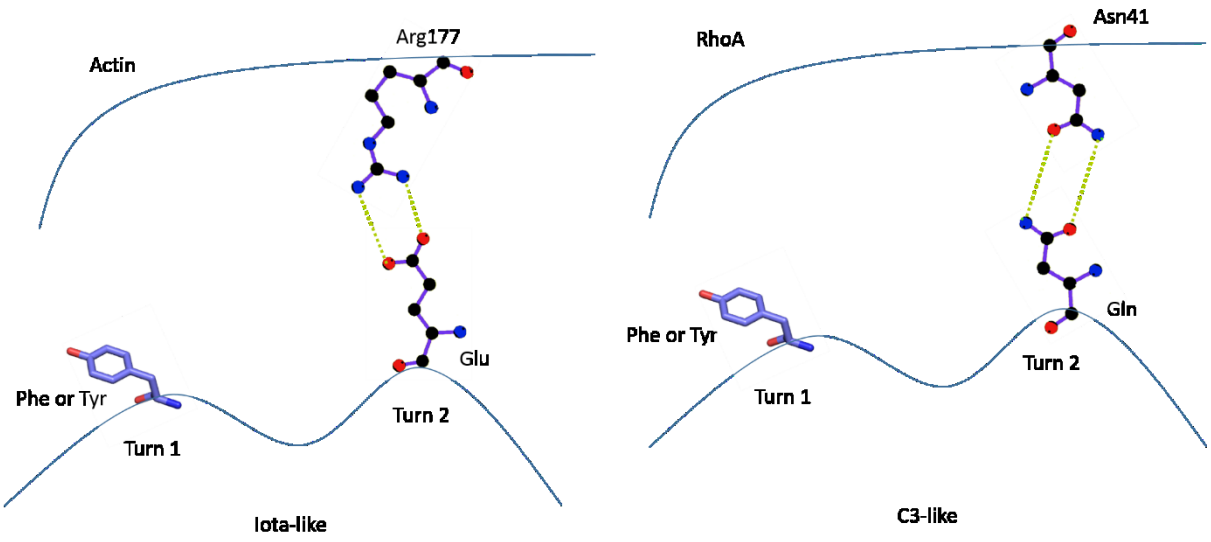

Figure 40: Mechanism of substrate recognition of the ADP-ribosylating toxins. The proposed interaction between Glu378 of Ia and Arg177 of actin is shown on the left. The interaction between Gln183 of C3 and Asn41 of RhoA is shown on the right. Modified from Tsuge et al., 2016.

The Q/EXE motif is found in all known bacterial arginine-, cysteine-, asparagine-, and guanosine-specific ARTs (Hottiger et al., 2010). Although we did not succeed in creating a model of E49R in the crystal experiment, this type of study highlights to the key factors in amino acid substrate recognition of the ADP-ribosylating toxins.

In conclusion, CPILE-a harbored the highly conserved RSE triad motif similar to that of the other members of ARTC toxins. The apo-, NAD^+-, and NADH-CPILE-a crystal structures were studied and deposited in PDB as 5GTT, 5WTZ, and 5WU0, respectively. Even though CPILE-a and Ia had similar tertiary structures, they had different NAD glycohydrolase activities. CPILE-a had almost no NAD glycohydrolase activity without actin and showed an unknown activity with actin. This difference might be caused by one α helix position forming the narrow NAD binding cleft without actin.

Actin may induce some change in the NAD binding pocket and induce an unknown reaction. Enzyme activity modulation by other protein can be seen as in next example. Without α-lactalbumin, β-1, 4-galactosyltransferase transfers UDP-galactose to terminal GlcNAc. With α-lactalbumin, this enzyme changes its acceptor from GlcNAc to D-glucose and catalyzes lactose synthesis (Richardson and Brew, 1980). However, we do not deny the possibility that the unknown product was produced from ADP-ribosylated actin.

Moreover, CPILE-a possessed ADP-ribosyltransferase activity against both α-actin and β/γ-actin, but it showed different sensitivity against actin isoforms. CPILE-a preferred α-actin as a substrate more than β/γ-actin. However, it is still unclear how CPILE-a and Ia distinguish between α-actin and β/γ-actin. In the near future, the complex structure of CPILE-a-actin might provide information useful for substrate selection and recognition of ADP-ribosylating toxins.

……

Summary

A novel enterotoxin produced by *Clostridium perfringens* was isolated from several food poisoning outbreaks in Japan between 1997 and 2010. The clinical features and epidemiological investigations provided evidence that those food poisoning outbreaks might be caused by *C. perfringens* even though the *cpe* or CPE had not been detected. The isolates were identified as *C. perfringens* type A because the lethal activity was neutralized by anti-alpha toxin serum and carried on the alpha-toxin gene.

The CPILE in the present study belonged to the W5052 strain, which was isolated from the outbreak in Tokyo. CPILE-a shared high sequence similarity to Ia (62%); hence, this study focused on the similarities and differences between CPILE-a and Ia on structural and functional aspects. The crystal structure of CPILE-a is similar to Ia with an RMSD 1.56 Å (360 amino acid residues compared), but it has some extra-long loops not present in Ia. The different loops are loop I (Ala60-Ile67), protruding loop I (PT I; Gly262-Ser269), and protruding loop II (PT II; Glu402-Lys408). The RSE triad motifs are perfectly conserved in CPILE-a.

Examination of the crystal structures of NAD^+-CPILE-a (5WTZ) and CPILE-a-NADH (5WU0) showed that there were no obvious structural differences between them. On the other hand, CPILE-a has a narrower NAD-binding pocket than that of Ia. NADase activity is different between CPILE-a and Ia. Our NADase assay showed that CPILE-a had almost no NADase activity even incubated at room temperature overnight, whereas Ia showed high NADase activity. Interestingly, the NADase activity with actin results demonstrated that actin seemed to trigger an unknown reaction of CPILE-a and produced unidentified products at chromatographic retention times of 1.4 minutes and 3.0 minutes. These differences might be brought by narrow NAD-binding pocket of CPILE-a.

Furthermore, several important amino acid residues were selected and mutated to study the interaction between CPILE-a and actin by using the FITC technique. The results showed that the CPILE-a mutants had different patterns of ADP-ribosyltransferase activity between α-actin and β/γ-actin. However, the Ia mutants influenced the ADP-ribosyltransferase activity against muscle α-actin in a manner similar to that against non-muscle β/γ-actin. Wild-type CPILE-a preferred α-actin as a substrate more than β/γ-actin. It

remains unclear how CPILE-a interacts and distinguishes particular actin isoforms that have only twenty seven amino acid residue differences between α-actin and β-actin.

Chapter VII

Materials and Methods

Protein expression and purification

A) CPILE-a

The cpile-a/pGEX4T-2 vectors that expressed a glutathione S-transferase (GST) with a thrombin site at the amino-termini were transformed into *E. coli* BL21 (DE3)-competent cells. Then, the activated competent cells were spread on LB agar containing ampicillin and were incubated at 37°C overnight. A single colony was picked up and inoculated into LB broth containing 100 μg/ml ampicillin. Those cells were grown overnight at 37°C with 150 rpm shaking.

The overnight culture was inoculated into 1.5 L of LB broth containing 100 μg/ml ampicillin. The culture broth was allowed to grow until the absorbance at 600 nm reached 0.6, then the final concentration of 1 mM of isopropyl β-D-1-thiogalactopyranoside (IPTG) was added. For the induction period, the culture cells were incubated at 16°C with 100 rpm shaking overnight and were harvested by centrifugation at 8,000 x g at 4°C for 5 minutes.

CPILE-a protein were extracted by using the Bugbuster® protein extraction reagent (Novagen) and then were centrifuged at 13,000 rpm, at 4°C for 35 minutes. Then, the supernatant was passed through GSH Sepharose 4B beads (GE Healthcare). The beads were washed with 50 ml of phosphate buffer saline (PBS), pH 7.4, then thrombin was added to the Sepharose beads, and the suspension was incubated at room temperature overnight.

The day after, CPILE-a was eluted by using PBS, and the protein concentrations of every milliliter of the eluent were checked by using NanoDrop. The eluents were further purified by gel filtration chromatography using a Superdex 200 column (GE Healthcare). The purity of CPILE-a was checked by SDS-polyacrylamide gel electrophoresis (SDS-PAGE) at 47.5 kDa band.

In addition, selenomethionine-labeled CPILE-a, triple cysteine mutants CPILE-a, and 12 mutants were expressed and purified in the manner as used for the wild-type. The 12 mutants of CPILE-a were L61A, N63A, Y252A, L308A, Y313A, K353A, Y377A, E380A,

E382A, S404A, L405A, and a double mutant E266G/N267G. To avoid a freeze-thaw cycle, the purified CPILE-a mutants were aliquoted and kept at –80°C until used.

B) Ia

The Ia/pET15b vectors that expressed His_6-tag that included a thrombin site in the amino-termini were transformed into *E. coli* BL21 (DE3) competent cells. The *E. coli* culturing was performed as described above.

The cell paste was resuspended in A-buffer containing 20 mM Tris HCl, 500 mM NaCl, and 20 mM imidazole at pH 8.0. Then, the cell suspension was lysed by sonication and centrifuged at 13,000 rpm for 35 minutes at 4°C. The supernatant was passed through Ni-NTA resin (Thermo Fisher Scientific). The resins were washed in 50 ml of A-buffer, then thrombin was added and the suspension was incubated at room temperature overnight. Ia was eluted by using the A-buffer and further passed through a first PD10. Then, the eluents were injected into a UNO-Q1 and subjected to a second PD10 before further purification by gel filtration chromatography using a Superdex 75 column (GE Healthcare). Nine mutants of Ia, including Y60S, Y62S, Y251A, L306S, Y311S, K351S, Y375S, E378S, and E380S, were expressed and purified in the same as used for the wild-type.

Crystallization and structure determination

Crystallization of the purified CPILE-a was attempted by using a variety of protein concentrations and two Hampton screening kits, including HR2-110 and HR2-112. After several tries, the crystals formed in the drop from the HR2-110 screening kit #6. Several buffers, salts, pHs, PEG concentrations, and temperatures were also screened. Interestingly, CPILE-a crystals only grew under $MgCl_2$ salt alkaline conditions.

Finally, the CPILE-a crystals were grown at 4°C via hanging drop vapor diffusion against a reservoir containing 18% PEG4000 and 100 mM Tris HCl at pH 8.5in 200 mM $MgCl_2$. The drop carried equal volumes of the purified CPILE-a and reservoir solution. The selected crystal was flash-frozen in liquid nitrogen with 30% ethylene glycol as a cryoprotectant; then, the data sets were collected in-house by using a MicroMax-007 generator and RAXIS VII (RIGAKU) at 2.01 Å. All diffraction images were processed by HKL2000 suite.

However, the first attempt to determine the CPILE-a structure by molecular replacement (MR) failed to solve the structure even though the Ia structure (1GIQ) was used as a search model. The second attempt using a selenomethionine-labeled data set also was unsuccessful in solving the phase determination problem. Thus, the triple mutants of cysteine substitution to Ala97, Ser185, and Ser366 were introduced to obtain the phase by using heavy atom replacement. The crystals were soaked in 1 mM mercury chloride mother liquor for 22 hours, then the data sets at three different wavelengths for peak, edge, and remote were collected by using an NW-12A beamline in KEK PF-AR.

The initial phase was obtained by using SHELX (hkl2map). Next, auto-tracing with side-chain information was performed by using ARP/wARP. The structure was refined by using phenix.refine and the PDB_REDO Web server. Finally, the space group of *I*222 at cell dimensions of a = 70.338 Å, b =100.665 Å, and c = 126.003 Å was refined against the wild-type CPILE-a data obtained earlier in-house at 2.01 Å resolution.

Molecular modeling of actin–CPILE-a

The alpha actin- and beta actin-CPILE-a complexes were modeled by using the Ia–actin complex (4H03) and profilin-beta actin complex (2BTF). The complex models were obtained by using LSQ superpose in the CCP4i suite, and then the complex structure was featured by using PyMOL. The models were subjected to energy minimization by using UCSF Chimera. This energy minimization consists of steepest descent and conjugate gradient methods for finding a minimum on the potential energy of the complex. The complex models were screened for all interchain contact residues by using the Contact program in the CCP4i suite at distances $\leq$ 5 Å.

Mutagenesis and ADP-ribosyltransferase activity assay

For the actin–CPILE-a model, 11 residues were selected to substitute with alanine. The mutants were L61A, N63A (loop I), Y252A, L308A, Y313A (loop III), K353A (loop IV), Y377A, E380A, E382A (loop V), S404A, and L405A (protruding loop II). Moreover, the double glycine substitution was made as E266GN267G (Protruding loop I). After purification, the mutants were tested for ADP-ribosyltransferase activity by using fluorescein isothiocyanate (FITC) labeling as a part of the streptavidin-biotin complex. Briefly, biotin-

NAD was cleaved and the biotin-ADP-ribose moiety was transferred to the target actin; hence, the ribosylated actin was labeled by streptavidin-FITC. The FITC labeling was detected by Typhoon FLA 9000 (GE Healthcare) at 800 V.

NADase activity

The reaction compoments were 10 μM enzyme (CPILE-a or Ia) and 1 mM βNAD^+ in 20 mM Tris HCl at pH 8.0. The reactions were stopped by freezing at –80°C for 2 minutes. The mixtures were thawed and injected into an LC Net II/ADC Chromatography Data Solutions system (JASCO), which was equilibrated with a mobile phase composed of a mixture of 20 mM phosphate buffer, pH 5.9, and 5% (v/v) acetonitrile. The reference substances included βNAD^+, βNADH, nicotinamide, ADP-ribose, and AMP. All reference substances were prepared as 1 mM and were injected separately. The retention times were recorded for 10 minutes. To minimize noise, the column was washed with one volume of mobile phase. A similar assay with 10 μM actin was also performed.

……

References

1. Songer JG. Clostridial enteric diseases of domestic animals. Clin Microbiol Rev. 1996 Apr; 9(2): 216–234. PMID: 8964036
2. Petit L, Gilbert M, and Popoff MR. *Clostridium perfringens*: toxinotype and genotype. Trends Microbiol. 1999 Mar; 7(3): 104-110. PMID: 10203838
3. Stiles BG, Pradhan K, Fleming JM, Perumal Samy R, Barth H, and Popoff MR. Clostridium and Bacillus binary enterotoxins: bad for the bowels, and eukaryotic being. Toxins. 2014 Sep: 6(9), 2626-2656. doi: 10.3390/toxins6092626
4. Hassen KA, Elbourne LDH, Tetu SG, Melville SB, Rood JI, and Paulsen IT. Genomic analyses of *Clostridium perfringens* isolates from five toxinotypes. Res Microbiol. 2015 May; 166(4): 255-263. doi: 10.1016/j.resmic.2014.10.003
5. Sakurai J and Kobayashi K. Lethal and dermonecrotic activities of *Clostridium perfringens* iota toxin: Biological activities induced by cooperation of two nonlinked components. Microbiol Immunol. 1995; 39(4): 249-253. PMID: 7651239
6. Papatheodorou P, Carette JE, Bell GW, Schwan C, Guttenberg G, Brummelkamp TR, et al. Lipolysisstimulated lipoprotein receptor (LSR) is the host receptor for the binary toxin *Clostridium difficile* transferase (CDT). Proc Natl Acad Sci U S A 2011; 108: 16422–16427. doi: 10.1073/pnas.1109772108 PMID: 21930894
7. Perelle S, Gibert M, Boquet P, and Popoff MR. Characterization of *Clostridium perfringens* iota-toxin genes and expression in *Escherichia coli*. Infect. Immun. 1993 Dec; 61(12): 5147-5156. PMID: 8225592
8. Marvaud JC, Stiles BG, Chenal A, Gillet D, Gibert M, Smith LA, et al. *Clostridium perfringens* iota toxin. Mapping of the Ia domain involved in docking with Ib and cellular internalization. J Biol Chem 2002 Sep; 277: 43659–43666. doi: 10.1074/jbc.M207828200 PMID: 12221101
9. Sakurai J, Nagahama M, Oda M, Tsuge H, and Kobayashi K. *Clostridium perfringens* iota toxin: structure and function. Toxins. 2009 Dec; 1(2): 208-228. doi: 10.3390/toxins1020208
10. Tsurumura T, Tsumori Y, Qiu H, Oda M, Sakurai J, Nagahama M, et al. Arginine ADP-ribosylation mechanism based on structural snapshots of iota-toxin and actin

complex. Proc Natl Acad Sci U S A. 2013; 110: 4267–4272. doi: 10.1073/pnas.1217227110 PMID: 23382240

11. Aktories K, Lang AE, Schwan C, and Mannherz HG.. Actin as target for modification by bacterial toxin protein toxins. FEBS. 2011 May; 278(23): 4526-4543. doi: 10.1111/j. 1742-4658.2011.08113.x
12. Stiles BG, Wigelsworth DJ, Popoff MR, and Barth H. Clostridial binary toxins: iota and C2 family portraits. Front Cell Infect Microbiol. 2011 Dec; 1(11): 1-14. doi: 10.3389/fcimb.2011.00011
13. Barth H, and Aktories K. New insights into the mode of action of the actin ADP-ribosylating virulence factors *Salmonella enterica* SpvB and *Clostridium botulinum* C2 toxin. Eur. J. Cell Biol. 2011 Nov; 90(11): 944-950. doi: 10.1016/j.ejcb.2010.11.007 PMID: 21247657
14. Monma C, Hatakeyama K, Obata H, Yokoyama K, Konishi N, Itoh T, et al. Four foodborne disease outbreaks caused by a new type of enterotoxin-producing *Clostridium perfringens*. J Clin Microbiol. 2015 Jan; 53(3): 859–867. doi: 10.1128/JCM.02859-14 PMID: 25568432
15. Yonogi S, Matsuda S, Kawai T, Yoda T, Harada T, Kumeda Y, et al. BEC, a novel enterotoxin of *Clostridium perfringens* found in human clinical isolates from acute gastroenteritis outbreaks. Infect Immun. 2014 Jun; 82(6): 2390–2399. doi: 10.1128/IAI.01759-14 PMID: 24664508
16. Irikura D, Monma C, Suzuki Y, Nakama A, Kai A, Fukui-Miyazaki A, et al. Identification and Characterization of a New Enterotoxin Produced by *Clostridium perfringens* Isolated from Food Poisoning Outbreaks. PLoS One 2015 Nov; 10(11): e0138183. doi: 10.1371/journal.pone.0138183 PMID: 26584048
17. Rhodes G. Crystallography made crystal clear. A guide for users of macromolecular models. 3rd ed. Academic Press. 2006.
18. Rupp B. Biomolecular crystallography. Principle, Practice, and Application to Structural Biology. Garland Science. 2010.
19. McPherson A and Gavira JA. Introduction to protein crystallization. Acta Crystallogr F Struct Biol Commun, 2014 Jan; 70(Pt 1): 2-20. doi: 10.1107/S2053230X13033141 PMID: 24419610
20. Taylor G. The phase problem. Acta Crystallogr D Biol Crystallogr. 2003; D59, 1881-1890. doi: 10.1107/S0907444903017815
21. Blundell and John 1994. Protein Crystallography. Academic Press. 1976.

22. Schneider TR and Sheldrick GM. Substructure solution with SHELXD. Acta Crystallogr D Biol Crystallogr. 2002; D58, 1772-1779. PMID: 12351820
23. Sheldrick GM. A short history of SHELX. Acta Crystallogr A Found Crystallogr. 2008; A64, 112-122. doi: 10.1107/S0108767307043930
24. Sheldrick GM. Experimental phasing with SHELXC/D/E: combining chain tracing with density modification. Acta Crystallogr D Biol Crystallogr. 2010; D66, 479-485. doi: 10.1107/S0907444909038360
25. Grüne T. CCP4-Workshop 2010: shelx c/d/e Tutorial.
26. Langer G, Cohen SX, Lamzin VS, Perrakis A. Automated macromolecular model building for X-ray crystallography using ARP/wARP version 7. Nat Protoc 2008; 3: 1171–1179. doi: 10.1038/nprot.2008.91 PMID: 18600222
27. Hottiger MO, Hassa PO, Lüscher B, Schüler H, and Koch-Nolte F. Toward a unified nomenclature for mammalian ADP-ribosyltransferasees. Trends Biochem. Sci. 2010 Apr; 35(4): 208-219. doi: 10.1016/j.tibs.2009.12.003 PMID: 20106667
28. Maehama T, Hoshino S, and Katada T. Increase in ADP-ribosyltransferase activity of rat T lymphocyte alloantigen RT6.1 by a single amino acid mutation. FEBS Letters. 1996 Jun; 388(2-3): 189-191. doi: 10.1016/0014-5793(96)00568-6
29. Han S, Arvai AS, Clancy SB, and Tainer JA. Crystal structure and novel recognition motif of Rho ADP-ribosylating C3 exoenzyme from *Clostridium botulinum*: structural insights for recognition specificity and catalysis. J Mol Biol. 2001 Jan; 305(1): 95-107. doi: 10.1006/jmbi.2000.4292 PMID: 11114250
30. Vogelsgesang M and Aktories K. Exchange of glutamine-217 to glutamate of *Clostridium limosum* Exoenzyme C3 turns the asparagine-specific ADP-ribosyltransferase into an arginine-modifying enzyme. Biochemistry. 2006 Jan; 45(3): 1017-1025. doi: 10.1021/bi052253g PMID: 16411778
31. Oppenheimer NJ. NAD hydrolysis: Chemical and enzymatic mechanism. Mol Cell Biochem. 1994; 138(1): 245-251. doi: 10.1007/BF00928468 PMID: 7898470
32. Han S, Craig JA, Putnam CD, Carozzi NB, Tainer JA. Evolution and mechanism from structures of an ADP-ribosylating toxin and NAD complex. Nat Struct Biol 1999; 6: 932–936. doi: 10.1038/13300 PMID: 10504727
33. van Troy M, Vandekerckhove J, and Ampe C. Structural modules in actin-binding proteins: towards a new classification. Biochimica et Biophysica Acta. 1999 Jan; 1448(3): 323-348. doi: 10.1016/S0167-4889(98)00152-9

34. Tsuge H, Nagahama M, Oda M, Iwamoto S, Utsunomiya H, Marquez VE, et al. Structural basis of actin recognition and arginine ADP-ribosylation by *Clostridium perfringens* iota-toxin. Proc Natl Acad Sci U S A. 2008 May; 105: 7399–7404. doi: 10.1073/pnas.0801215105 PMID: 18490658
35. Winn, MD., Ballard, CC., Cowtan, KD., Dodson, EJ., Emsley, P., Evans, PR., Keegan, RM., Krissinel, EB., Leslie, AGW., McCoy, A., McNicholas, SJ., Murshudov, GN., Pannu, NS., Potterton, EA., Powell, HR., Read, RJ., Vagin, A., and Wilson, KS. (2011). Overview of the CCP4 suite and current developments. Acta Crystallogr D Biol Crystallogr. D67, 235-242. doi: 10.1107/S09074449100045749
36. The CCP4 suite: programs for protein crystallography. Acta Crystallogr D Biol Crystallogr. 1994; D50: 760–763. doi: 10.1107/S0907444994003112 PMID: 15299374 (Bailey S. as a contact person)
37. Tsuge H, Nagahama M, Nishimura H, Hisatsune J, Sakaguchi Y, Itogawa Y, Katunuma N, and Sakurai J. Crystal structure and site-directed mutagenesis of enzymatic components from *Clostridium perfringens* iota toxin. J Mol Biol. 2003 Jan; 325(3): 471-483. PMID: 12498797
38. Toniti W, Yoshida T, Tsurumura T, Irikura D, Monma C, Kamata Y, and Tsuge H. Crystal structure and structure-based mutagenesis of actin-specific ADP-ribosylating toxin CPILE-a as novel enterotoxin. PLoS One. 2017 Feb; 12(2): e0171278 doi: 10.1371/journal.pone.0171278 PMCID: PMC5310789
39. Kawahara, K., Yonogi, S., Munetomo, R., Oki, H., Yoshida, T., Kumeda, Y., Matsuda, S., Kodama, T., Ohkubo, T., Iida, T., and Nakamura, S. (2016). Crystal structure of the ADP-ribosylating component of BEC, the binary enterotoxin of *Clostridium perfringens*. Biochem. Biophys. Res. Commun. 480, 261-267.
40. Cassel D, Pfeuffer T. Mechanism of cholera toxin action: covalent modification of the guanyl nucleotidebinding protein of the adenylate cyclase system. Proc Natl Acad Sci U S A 1978; 75: 2669–2673. PMID: 208069
41. Iglewski BH, Kabat D. NAD-dependent inhibition of protein synthesis by *Pseudomonas aeruginosa* toxin. Proc Natl Acad Sci U S A 1975; 72: 2284–2288. PMID: 166383
42. Aktories K, Barmann M, Ohishi I, Tsuyama S, Jakobs KH, Habermann E. Botulinum C2 toxin ADP-ribosylates actin. Nature 1986; 322: 390–392. doi: 10.1038/322390a0 PMID: 3736664

43. Hochmann H, Pust S, von Figura G, Aktories K., and Barth H. *Salmonella enterica* SpvB ADP-ribosylates actin at position arginine-177: Characterization of the catalytic domain within the SpvB protein and a comparison to binary clostridial actin-ADP-ribosylating toxins. Biochemistry. 2006; 45(4): 1271-1277. doi: 10.1021/bi051810w
44. Margarit SM, Davidson W, Frego L, and Stebbins CE. A steric antagonism of actin polymerization by a Salmonella virulence protein. Structure. 2006 Aug; 14(8): 1219-1229. doi: 10.1016/j.str.2006.05.022 PMID: 16905096
45. Toda A, Tsurumura T, Yoshida T, Tsumori Y, Tsuge H. Rho GTPase Recognition by C3 Exoenzyme Based on C3-RhoA Complex Structure. J Biol Chem 2015; 290: 19423–19432. doi: 10.1074/jbc.M115. 653220 PMID: 26067270
46. Tsuge H, Yoshida T, and Tsurumura T. Conformational plasticity is crucial for C3-RhoA complex formation by ARTT-loop. Pathog Dis 2015 Oct; 73(9): ftv094 doi: 10.1093/femspd/ftv094 PMID: 26474844
47. Tsuge H, Tsurumura T, Toda A, Murata H, Toniti W, and Yoshida T. Comparative studies of Actin- and Rho-specific ADP-ribosylating toxins: Insight from Structural Biology. In The Actin cytoskeleton and bacterial infection, Mannherz HG (editor). Springer. 2016
48. Richardson RH and Brew K. Lactose Synthase. An investigation of the interaction site of α-lactalbumin for galactosyltransferase by differential kinetic labeling. J Biol Chem 1980 Apr; 255(8): 3377-3385 PMID: 6767715

……

Acknowledgement

Ich weiß, dass Ich weiß nichts.

I sincerely thank to Prof. Dr. Hideaki Tsuge, Prof. Dr. Ken Yokoyama, and Prof. Dr. Akira Kurosaka for all kind suggestions. I also thank to Dr. Toru Yoshida for his valuable suggestions and comments during my experiments. I wish to thank to Dr. Toshiharu Tsurumura, Ms. Yayoi Tsumori, and Mr. Akiyuki Toda for a lot of support. Thanks for some kindness from Tsuge's lab members and staffs of Faculty of Life Sciences, Kyoto Sangyo University. I also thank all staffs of the Graduate office for their individual help, and made me able to complete this thesis.

I would like to express my deepest gratitude to my beloved advisors, Dr. Tongtavuch Anukarahanonta and Dr. Jumpol Nimpanich, for their guidance, criticism and patience throughout my long time study. I also would like to say thank you to my law teachers who being my role models in Human rights issues, Assist. Prof. Kittisak Prokati and Assoc. Prof. Phunthip Kanchanachittra Saisoonthorn from Faculty of Law, Thammasat University. My special thanks to Yasuo Imai and Nihonga classmates for every support. All of support from you will be remembered.

Throughout this thesis, many persons have provided useful comments and supports. I express sincere appreciation to AT, BC, RC, KT, NK, YT, and NP especially for both of you AK and KT.

Finally, I would like to express my deepest gratitude to my parents and family for their understanding and encouragement.

Ich weiß, dass Ich nicht weiß.

Waraphan Toniti

……

Appendix A

Summary of data collection

Wild type CPILE-a:

Summary of reflections intensities and R-factors by shells

R linear = SUM (ABS(I - <I>)) / SUM (I)

R square = SUM ((I - <I>) ** 2) / SUM (I ** 2)

Chi**2 = SUM ((I - <I>) ** 2) / (Error ** 2 * N / (N-1)))

In all sums single measurements are excluded

Shell limit	Lower Upper Angstrom	Average I	Average error	Stat.	Norm. Chi**2	Linear R-fac	Square R-fac	Rmeas	Rpim	CC1/2	CC*
50.00	5.45	957.2	14.0	6.7	1.833	0.032	0.032	0.035	0.013	0.999	1.000
5.45	4.33	1012.5	14.9	8.0	2.695	0.044	0.047	0.048	0.018	0.999	1.000
4.33	3.78	941.1	14.8	8.9	3.430	0.054	0.053	0.058	0.021	0.999	1.000
3.78	3.44	650.6	12.4	8.7	3.510	0.069	0.064	0.074	0.027	0.997	0.999
3.44	3.19	420.3	10.2	8.1	3.346	0.087	0.078	0.094	0.035	0.997	0.999
3.19	3.00	273.5	8.6	7.4	3.038	0.109	0.091	0.117	0.043	0.996	0.999
3.00	2.85	197.0	7.8	7.0	2.957	0.135	0.109	0.146	0.054	0.994	0.998
2.85	2.73	144.7	7.2	6.7	2.606	0.163	0.128	0.176	0.065	0.991	0.998
2.73	2.62	101.2	6.8	6.5	2.481	0.213	0.173	0.229	0.085	0.985	0.996
2.62	2.53	88.5	6.7	6.5	2.346	0.234	0.181	0.252	0.094	0.983	0.996
2.53	2.45	77.7	6.6	6.5	2.235	0.255	0.193	0.275	0.102	0.983	0.996
2.45	2.38	67.0	6.6	6.4	2.214	0.283	0.222	0.305	0.114	0.975	0.994
2.38	2.32	58.2	6.6	6.5	2.133	0.317	0.231	0.343	0.130	0.975	0.994
2.32	2.26	52.0	6.7	6.6	2.089	0.340	0.259	0.369	0.141	0.964	0.991
2.26	2.21	46.2	6.8	6.7	2.131	0.362	0.273	0.393	0.152	0.956	0.989
2.21	2.17	39.3	7.0	7.0	2.078	0.407	0.347	0.443	0.172	0.947	0.986
2.17	2.12	33.8	7.3	7.2	1.965	0.440	0.329	0.480	0.187	0.942	0.985
2.12	2.08	30.9	7.4	7.3	1.926	0.455	0.344	0.497	0.195	0.926	0.981
2.08	2.04	27.5	7.4	7.4	1.870	0.485	0.358	0.530	0.209	0.924	0.980
2.04	2.01	21.3	7.4	7.3	1.869	0.603	0.453	0.660	0.262	0.885	0.969
All reflections		271.7	8.7	7.2	2.493	0.092	0.059	0.099	0.037		

Shell		I/Sigma in resolution shells:								
Lower	Upper	% of of reflections with I / Sigma less than								
limit	limit	0	1	2	3	5	10	20	>20	total
50.00	5.45	0.4	0.9	1.2	1.7	3.1	5.4	10.6	87.6	98.2
5.45	4.33	0.3	0.6	1.2	2.2	2.9	6.4	12.2	87.8	100.0
4.33	3.78	0.3	1.0	1.8	2.4	3.9	8.4	15.7	84.3	100.0
3.78	3.44	0.3	0.9	2.3	3.7	6.3	13.4	24.0	76.0	100.0
3.44	3.19	1.1	2.8	4.9	7.6	12.5	22.5	38.1	61.9	100.0
3.19	3.00	1.4	4.2	6.6	10.3	16.1	30.5	49.2	50.8	100.0
3.00	2.85	3.0	5.8	10.7	14.5	23.4	37.3	57.5	42.5	100.0
2.85	2.73	2.6	6.6	12.3	17.8	27.1	45.2	65.6	34.4	100.0
2.73	2.62	4.2	10.7	17.1	24.8	35.5	55.2	74.8	25.2	100.0
2.62	2.53	5.6	12.4	20.9	29.0	41.2	59.2	78.9	21.1	100.0
2.53	2.45	5.0	13.2	23.8	33.2	47.6	63.9	81.3	18.7	100.0
2.45	2.38	7.7	16.7	28.0	36.9	49.7	67.7	84.0	16.0	100.0
2.38	2.32	9.2	20.8	31.7	41.2	55.2	72.3	88.0	12.0	100.0
2.32	2.26	9.1	20.5	34.1	44.6	59.7	74.8	89.2	10.6	99.9
2.26	2.21	11.9	26.3	40.5	49.9	62.9	76.4	89.7	9.7	99.5
2.21	2.17	11.6	26.6	39.8	50.2	64.6	81.0	92.4	6.2	98.7
2.17	2.12	15.0	30.0	44.9	56.2	68.1	82.8	93.1	4.5	97.6
2.12	2.08	15.0	30.6	44.8	55.4	68.4	82.4	90.4	4.7	95.0
2.08	2.04	15.3	31.2	46.2	56.4	69.1	79.6	86.3	3.9	90.2
2.04	2.01	16.9	32.9	45.9	56.1	68.2	78.9	83.9	1.8	85.8
All hkl		6.7	14.6	22.7	29.4	38.9	51.7	64.7	33.5	98.3

Shell		Summary of observation redundancies: % of reflections with given No. of observations										
Lower limit	Upper limit	0	1	2	3	4	5-6	7-8	9-12	13-19	>19	total
50.00	5.45	1.8	0.4	1.8	2.5	17.8	4.3	71.4	0.0	0.0	0.0	98.2
5.45	4.33	0.0	0.0	1.0	0.9	12.8	5.0	80.3	0.0	0.0	0.0	100.0
4.33	3.78	0.0	0.0	1.0	0.9	11.3	5.9	80.9	0.0	0.0	0.0	100.0
3.78	3.44	0.0	0.0	0.9	1.1	9.8	6.5	81.6	0.0	0.0	0.0	100.0
3.44	3.19	0.0	0.0	0.9	1.2	10.1	7.9	79.9	0.0	0.0	0.0	100.0
3.19	3.00	0.0	0.1	0.8	0.8	9.8	8.3	80.2	0.0	0.0	0.0	100.0
3.00	2.85	0.0	0.1	0.9	0.7	10.5	9.3	78.5	0.0	0.0	0.0	100.0
2.85	2.73	0.0	0.0	0.8	0.9	9.6	9.2	79.6	0.0	0.0	0.0	100.0
2.73	2.62	0.0	0.1	0.9	1.1	10.0	9.7	78.4	0.0	0.0	0.0	100.0
2.62	2.53	0.0	0.0	0.7	0.9	10.4	10.5	77.4	0.0	0.0	0.0	100.0
2.53	2.45	0.0	0.0	1.1	0.9	10.6	11.1	76.4	0.0	0.0	0.0	100.0
2.45	2.38	0.0	0.1	1.1	1.4	10.5	13.1	73.9	0.0	0.0	0.0	100.0
2.38	2.32	0.0	0.3	1.7	1.6	12.0	16.4	68.0	0.0	0.0	0.0	100.0
2.32	2.26	0.1	0.5	2.5	3.2	12.4	19.0	62.2	0.0	0.0	0.0	99.9
2.26	2.21	0.5	1.7	4.2	4.8	14.0	17.3	57.4	0.0	0.0	0.0	99.5
2.21	2.17	1.3	4.1	4.9	5.4	13.7	18.1	52.4	0.0	0.0	0.0	98.7
2.17	2.12	2.4	7.3	6.5	5.5	13.5	16.4	48.3	0.0	0.0	0.0	97.6
2.12	2.08	5.0	9.3	7.4	4.8	13.5	15.1	45.1	0.0	0.0	0.0	95.0
2.08	2.04	9.8	10.2	7.4	5.7	12.3	14.2	40.4	0.0	0.0	0.0	90.2
2.04	2.01	14.2	11.8	7.2	5.5	10.9	13.4	37.0	0.0	0.0	0.0	85.5
All hkl		1.7	2.3	2.7	2.5	11.8	11.5	67.6	0.0	0.0	0.0	98.3

Shell		Average Redundancy Per Shell
Lower limit	Upper limit	
50.00	5.45	6.8
5.45	4.33	7.2
4.33	3.78	7.3
3.78	3.44	7.3
3.44	3.19	7.2
3.19	3.00	7.2
3.00	2.85	7.2
2.85	2.73	7.2
2.73	2.62	7.2
2.62	2.53	7.1
2.53	2.45	7.1
2.45	2.38	7.0
2.38	2.32	6.8
2.32	2.26	6.6
2.26	2.21	6.3
2.21	2.17	6.1
2.17	2.12	5.8
2.12	2.08	5.6
2.08	2.04	5.4
2.04	2.01	5.2
All hkl		6.7

Hg-soaking CPILE-a:

Summary of reflections intensities and R-factors by shells

R linear = SUM (ABS(I - <I>)) / SUM (I)

R square = SUM ((I - <I>) ** 2) / SUM (I ** 2)

Chi**2 = SUM ((I - <I>) ** 2) / (Error ** 2 * N / (N-1)))

In all sums single measurements are excluded

Shell limit	Lower Upper Angstrom	Average I	Average error	Average Stat.	Norm. Chi**2	Linear R-fac	Square R-fac	Rmeas	Rpim	CC1/2	CC*
50.00	5.97	627.3	11.0	6.8	2.194	0.040	0.042	0.044	0.018	0.999	1.000
5.97	4.74	490.7	9.1	6.3	2.194	0.046	0.048	0.050	0.021	0.998	1.000
4.74	4.14	657.5	12.0	8.1	2.162	0.045	0.049	0.050	0.020	0.998	1.000
4.14	3.76	540.9	10.8	7.8	2.296	0.054	0.056	0.059	0.024	0.998	0.999
3.76	3.49	416.4	9.6	7.5	2.138	0.062	0.060	0.068	0.028	0.997	0.999
3.49	3.29	340.4	8.8	7.2	2.049	0.071	0.068	0.077	0.032	0.997	0.999
3.29	3.12	225.1	7.3	6.4	1.965	0.089	0.085	0.098	0.040	0.995	0.999
3.12	2.99	161.4	6.4	5.8	1.832	0.109	0.101	0.119	0.049	0.994	0.998
2.99	2.87	135.4	6.0	5.6	1.811	0.121	0.104	0.133	0.055	0.994	0.999
2.87	2.77	102.6	5.6	5.3	1.716	0.149	0.136	0.164	0.068	0.989	0.997
2.77	2.69	87.4	5.4	5.1	1.668	0.169	0.153	0.186	0.077	0.987	0.997
2.69	2.61	69.9	5.3	5.1	1.585	0.204	0.181	0.224	0.093	0.983	0.996
2.61	2.54	62.2	5.2	5.1	1.591	0.229	0.205	0.252	0.105	0.979	0.995
2.54	2.48	57.9	5.3	5.2	1.529	0.249	0.223	0.274	0.114	0.976	0.994
2.48	2.42	51.6	5.4	5.3	1.494	0.280	0.252	0.309	0.129	0.970	0.992
2.42	2.37	48.6	5.5	5.4	1.452	0.301	0.268	0.332	0.138	0.965	0.991
2.37	2.32	44.4	5.7	5.6	1.444	0.333	0.288	0.367	0.153	0.965	0.991
2.32	2.28	42.4	5.8	5.7	1.453	0.363	0.304	0.400	0.167	0.960	0.990
2.28	2.24	38.8	6.0	5.9	1.428	0.400	0.346	0.441	0.185	0.951	0.987
2.24	2.20	35.1	6.1	6.0	1.420	0.445	0.406	0.491	0.206	0.927	0.981
All reflections		211.9	7.1	6.1	1.772	0.089	0.065	0.098	0.041		

Shell		I/Sigma in resolution shells:								
Lower	Upper	% of reflections with I / Sigma less than								
limit	limit	0	1	2	3	5	10	20	>20	total
50.00	5.97	0.0	0.0	0.1	0.5	1.8	3.8	8.3	91.4	99.7
5.97	4.74	0.4	0.9	1.3	1.6	2.8	5.5	11.8	88.2	100.0
4.74	4.14	0.5	1.3	1.9	2.6	3.7	6.5	12.8	87.2	100.0
4.14	3.76	0.8	1.3	2.4	3.2	5.3	9.2	18.2	81.8	100.0
3.76	3.49	0.2	0.5	1.4	2.4	5.7	11.9	26.4	73.6	100.0
3.49	3.29	0.4	1.3	2.9	4.4	7.8	15.2	32.4	67.6	100.0
3.29	3.12	1.0	2.7	4.5	6.6	11.3	23.2	42.0	58.0	100.0
3.12	2.99	3.2	5.4	8.2	10.8	15.9	29.5	50.9	49.1	100.0
2.99	2.87	3.2	6.6	10.1	13.6	21.6	36.0	57.1	42.9	100.0
2.87	2.77	3.7	8.6	12.7	16.9	25.9	41.7	64.2	35.8	100.0
2.77	2.69	4.1	8.7	13.9	18.7	27.9	47.2	70.5	29.5	100.0
2.69	2.61	5.2	11.0	17.9	23.9	35.8	54.6	77.3	22.7	100.0
2.61	2.54	4.8	10.8	18.7	24.6	36.1	57.7	81.1	18.9	100.0
2.54	2.48	6.7	13.6	21.3	28.7	39.8	59.4	83.0	17.0	100.0
2.48	2.42	6.5	14.6	23.7	31.4	44.0	64.5	85.8	14.2	100.0
2.42	2.37	7.8	16.9	26.6	35.1	46.7	68.7	87.4	12.6	100.0
2.37	2.32	7.8	18.7	30.7	39.3	51.8	71.3	90.7	9.3	100.0
2.32	2.28	8.1	17.5	28.7	40.0	55.2	74.5	91.4	8.6	100.0
2.28	2.24	9.7	21.3	33.2	44.3	58.6	76.0	93.2	6.8	100.0
2.24	2.20	9.7	21.8	33.7	44.7	59.2	80.1	95.0	5.0	100.0
All hkl		4.2	9.2	14.7	19.7	27.8	41.8	59.0	41.0	100.0

Shell		Summary of observation redundancies: % of reflections with given No. of observations										
Lower limit	Upper limit	0	1	2	3	4	5-6	7-8	9-12	13-19	>19	total
50.00	5.97	0.3	0.3	0.5	0.9	14.9	65.8	17.3	0.0	0.0	0.0	99.7
5.97	4.74	0.0	0.0	0.1	0.4	12.4	66.6	20.5	0.0	0.0	0.0	100.0
4.74	4.14	0.0	0.0	0.1	0.5	10.7	66.4	22.3	0.0	0.0	0.0	100.0
4.14	3.76	0.0	0.0	0.0	0.5	10.8	64.4	24.2	0.0	0.0	0.0	100.0
3.76	3.49	0.0	0.0	0.0	0.2	11.0	64.6	24.2	0.0	0.0	0.0	100.0
3.49	3.29	0.0	0.0	0.0	0.1	11.2	62.9	25.8	0.0	0.0	0.0	100.0
3.29	3.12	0.0	0.0	0.0	0.3	10.9	62.8	25.9	0.0	0.0	0.0	100.0
3.12	2.99	0.0	0.0	0.0	0.2	11.1	62.5	26.1	0.0	0.0	0.0	100.0
2.99	2.87	0.0	0.0	0.0	0.3	11.3	61.9	26.5	0.0	0.0	0.0	100.0
2.87	2.77	0.0	0.0	0.0	0.4	11.6	61.8	26.1	0.0	0.0	0.0	100.0
2.77	2.69	0.0	0.0	0.0	0.5	11.5	60.8	27.2	0.0	0.0	0.0	100.0
2.69	2.61	0.0	0.0	0.0	0.2	11.5	61.7	26.6	0.0	0.0	0.0	100.0
2.61	2.54	0.0	0.0	0.0	0.4	11.7	60.4	27.6	0.0	0.0	0.0	100.0
2.54	2.48	0.0	0.0	0.0	0.6	12.4	60.0	26.9	0.0	0.0	0.0	100.0
2.48	2.42	0.0	0.0	0.0	0.8	12.5	59.2	27.5	0.0	0.0	0.0	100.0
2.42	2.37	0.0	0.0	0.0	0.6	13.2	58.8	27.4	0.0	0.0	0.0	100.0
2.37	2.32	0.0	0.0	0.0	0.7	13.2	59.8	26.3	0.0	0.0	0.0	100.0
2.32	2.28	0.0	0.0	0.0	0.5	14.1	57.0	28.3	0.0	0.0	0.0	100.0
2.28	2.24	0.0	0.0	0.1	1.9	12.7	58.4	26.9	0.0	0.0	0.0	100.0
2.24	2.20	0.0	0.0	0.4	2.1	14.1	55.9	27.4	0.0	0.0	0.0	100.0
All hkl		0.0	0.0	0.1	0.6	12.1	61.6	25.5	0.0	0.0	0.0	100.0

Shell		Average Redundancy Per Shell
Lower limit	Upper limit	
50.00	5.97	5.7
5.97	4.74	5.8
4.74	4.14	5.8
4.14	3.76	5.8
3.76	3.49	5.8
3.49	3.29	5.8
3.29	3.12	5.8
3.12	2.99	5.8
2.99	2.87	5.8
2.87	2.77	5.8
2.77	2.69	5.8
2.69	2.61	5.8
2.61	2.54	5.8
2.54	2.48	5.8
2.48	2.42	5.8
2.42	2.37	5.8
2.37	2.32	5.8
2.32	2.28	5.8
2.28	2.24	5.8
2.24	2.20	5.7
All hkl		5.8

Pt-soaking CPILE-a:

Summary of reflections intensities and R-factors by shells

R linear = SUM (ABS(I - <I>)) / SUM (I)

R square = SUM ((I - <I>) ** 2) / SUM (I ** 2)

Chi**2 = SUM ((I - <I>) ** 2) / (Error ** 2 * N / (N-1)))

In all sums single measurements are excluded

Shell limit	Lower Upper Angstrom	Average I	Average error	Stat.	Norm. Chi**2	Linear R-fac	Square R-fac	Rmeas	Rpim	CC1/2	CC*
50.00	5.40	515.1	8.6	4.9	2.036	0.039	0.047	0.043	0.018	0.998	0.999
5.40	4.29	598.3	9.6	5.5	2.130	0.039	0.045	0.043	0.018	0.998	1.000
4.29	3.74	525.9	8.8	5.4	2.270	0.043	0.049	0.047	0.019	0.998	1.000
3.74	3.40	373.3	6.8	4.6	2.187	0.047	0.050	0.051	0.021	0.998	1.000
3.40	3.16	240.8	5.0	3.7	1.977	0.052	0.053	0.057	0.023	0.998	0.999
3.16	2.97	152.7	3.8	3.1	1.864	0.061	0.057	0.067	0.027	0.998	1.000
2.97	2.82	110.4	3.2	2.7	1.766	0.070	0.063	0.077	0.032	0.997	0.999
2.82	2.70	82.7	2.8	2.5	1.662	0.080	0.070	0.088	0.036	0.997	0.999
2.70	2.60	61.3	2.6	2.3	1.639	0.099	0.087	0.109	0.045	0.996	0.999
2.60	2.51	52.3	2.5	2.3	1.557	0.109	0.089	0.120	0.049	0.995	0.999
2.51	2.43	46.3	2.5	2.3	1.551	0.123	0.100	0.136	0.056	0.994	0.998
2.43	2.36	39.9	2.5	2.3	1.480	0.137	0.105	0.150	0.062	0.993	0.998
2.36	2.30	35.1	2.5	2.4	1.420	0.153	0.118	0.168	0.070	0.992	0.998
2.30	2.24	33.4	2.6	2.5	1.572	0.176	0.137	0.193	0.080	0.991	0.998
2.24	2.19	28.9	2.6	2.5	1.438	0.193	0.145	0.212	0.088	0.988	0.997
2.19	2.14	23.2	2.5	2.5	1.367	0.226	0.167	0.249	0.103	0.984	0.996
2.14	2.10	21.3	2.6	2.5	1.356	0.247	0.187	0.272	0.114	0.980	0.995
2.10	2.06	19.4	2.6	2.5	1.414	0.273	0.211	0.301	0.126	0.979	0.995
2.06	2.02	15.1	2.5	2.5	1.294	0.324	0.227	0.358	0.150	0.971	0.993
2.02	1.99	13.2	2.6	2.6	1.230	0.343	0.250	0.382	0.166	0.957	0.989
All reflections		149.4	4.0	3.1	1.666	0.063	0.051	0.069	0.028		

Shell		I/Sigma in resolution shells:								
Lower limit	Upper limit	% of of reflections with I / Sigma less than								
		0	1	2	3	5	10	20	>20	total
50.00	5.40	0.1	0.3	0.7	0.9	1.3	2.9	5.5	93.8	99.3
5.40	4.29	0.2	0.3	0.6	0.9	1.3	2.7	5.9	94.1	100.0
4.29	3.74	0.6	1.1	1.4	1.7	2.4	4.5	9.8	90.2	100.0
3.74	3.40	0.3	0.6	1.0	1.5	2.4	6.0	14.4	85.6	100.0
3.40	3.16	0.7	1.9	3.3	4.7	7.2	12.8	24.4	75.6	100.0
3.16	2.97	1.9	3.1	4.2	6.0	9.2	16.7	32.6	67.4	100.0
2.97	2.82	3.7	6.1	8.3	11.0	15.4	25.1	42.2	57.8	100.0
2.82	2.70	4.1	8.0	10.9	13.9	19.9	31.6	50.1	49.9	100.0
2.70	2.60	4.7	9.2	13.4	17.1	24.5	40.4	59.2	40.8	100.0
2.60	2.51	5.8	10.5	16.2	21.7	29.7	45.9	64.1	35.9	100.0
2.51	2.43	7.0	13.0	19.3	23.4	32.1	48.9	68.4	31.6	100.0
2.43	2.36	8.0	15.5	22.5	28.9	37.3	54.3	74.4	25.6	100.0
2.36	2.30	8.1	16.5	25.3	32.2	43.4	58.4	77.5	22.5	100.0
2.30	2.24	9.7	19.1	28.3	35.5	46.3	62.3	80.0	20.0	100.0
2.24	2.19	9.1	19.2	29.3	37.1	49.3	65.9	82.3	17.7	100.0
2.19	2.14	11.2	23.1	34.8	44.2	55.9	71.4	87.1	12.9	100.0
2.14	2.10	10.9	23.5	36.0	45.7	57.8	73.0	88.9	11.1	100.0
2.10	2.06	11.1	24.0	38.0	48.5	60.4	77.1	90.6	9.4	100.0
2.06	2.02	15.6	31.8	44.9	54.0	65.1	80.5	93.8	6.2	100.0
2.02	1.99	16.0	33.5	48.3	56.9	68.9	83.7	94.7	5.3	100.0
All hkl		6.4	13.0	19.3	24.3	31.5	43.2	57.3	42.7	100.0

Shell		Summary of observation redundancies:										
Lower	Upper	% of reflections with given No. of observations										
limit	limit	0	1	2	3	4	5-6	7-8	9-12	13-19	>19	total
50.00	5.40	0.7	0.3	0.8	1.8	17.2	53.6	25.7	0.0	0.0	0.0	99.3
5.40	4.29	0.0	0.0	0.1	0.7	15.8	55.7	27.7	0.0	0.0	0.0	100.0
4.29	3.74	0.0	0.0	0.1	0.7	15.8	55.6	27.8	0.0	0.0	0.0	100.0
3.74	3.40	0.0	0.0	0.1	0.8	15.4	55.6	28.2	0.0	0.0	0.0	100.0
3.40	3.16	0.0	0.0	0.0	0.6	15.5	55.5	28.4	0.0	0.0	0.0	100.0
3.16	2.97	0.0	0.0	0.1	0.8	14.8	54.9	29.4	0.0	0.0	0.0	100.0
2.97	2.82	0.0	0.0	0.0	0.5	15.3	55.0	29.1	0.0	0.0	0.0	100.0
2.82	2.70	0.0	0.0	0.1	0.8	14.7	55.7	28.7	0.0	0.0	0.0	100.0
2.70	2.60	0.0	0.0	0.0	0.7	14.6	55.8	28.9	0.0	0.0	0.0	100.0
2.60	2.51	0.0	0.0	0.0	0.5	14.7	55.1	29.7	0.0	0.0	0.0	100.0
2.51	2.43	0.0	0.0	0.0	0.6	14.7	55.7	29.0	0.0	0.0	0.0	100.0
2.43	2.36	0.0	0.0	0.0	0.6	14.9	55.6	29.0	0.0	0.0	0.0	100.0
2.36	2.30	0.0	0.0	0.1	0.4	14.9	55.6	29.0	0.0	0.0	0.0	100.0
2.30	2.24	0.0	0.0	0.1	0.9	15.1	55.6	28.3	0.0	0.0	0.0	100.0
2.24	2.19	0.0	0.0	0.0	0.6	14.5	56.7	28.2	0.0	0.0	0.0	100.0
2.19	2.14	0.0	0.0	0.0	0.5	15.1	56.0	28.4	0.0	0.0	0.0	100.0
2.14	2.10	0.0	0.0	0.0	1.0	16.0	56.6	26.5	0.0	0.0	0.0	100.0
2.10	2.06	0.0	0.0	0.4	1.9	17.5	54.4	25.7	0.0	0.0	0.0	100.0
2.06	2.02	0.0	0.1	0.6	1.8	18.1	55.0	24.4	0.0	0.0	0.0	100.0
2.02	1.99	0.0	0.2	1.1	6.1	27.4	47.9	17.4	0.0	0.0	0.0	100.0
All hkl		0.0	0.0	0.2	1.1	16.1	55.1	27.5	0.0	0.0	0.0	100.0

Shell		
Lower	Upper	Average Redundancy Per Shell
limit	limit	
50.00	5.40	5.7
5.40	4.29	5.8
4.29	3.74	5.8
3.74	3.40	5.8
3.40	3.16	5.8
3.16	2.97	5.8
2.97	2.82	5.8
2.82	2.70	5.8
2.70	2.60	5.8
2.60	2.51	5.8
2.51	2.43	5.8
2.43	2.36	5.8
2.36	2.30	5.8
2.30	2.24	5.7
2.24	2.19	5.7
2.19	2.14	5.7
2.14	2.10	5.7
2.10	2.06	5.6
2.06	2.02	5.6
2.02	1.99	5.2
All hkl		5.7

NAD^+-CPILE-a

Summary of reflections intensities and R-factors by shells

R linear = SUM (ABS(I - <I>)) / SUM (I)

R square = SUM ((I - <I>) ** 2) / SUM (I ** 2)

Chi**2 = SUM ((I - <I>) ** 2) / (Error ** 2 * N / (N-1)))

In all sums single measurements are excluded

Shell limit	Lower Upper Angstrom	Average I	Average error	Stat.	Norm. Chi**2	Linear R-fac	Square R-fac	Rmeas	Rpim	CC1/2	CC*
50.00	6.78	136.6	3.7	3.2	0.471	0.032	0.034	0.035	0.014	0.998	1.000
6.78	5.38	53.8	2.3	2.2	0.465	0.048	0.047	0.053	0.022	0.998	0.999
5.38	4.70	71.3	2.9	2.7	0.534	0.054	0.052	0.059	0.023	0.998	1.000
4.70	4.27	79.4	3.2	3.0	0.634	0.059	0.056	0.064	0.024	0.998	0.999
4.27	3.97	64.1	2.8	2.7	0.615	0.067	0.059	0.072	0.027	0.998	1.000
3.97	3.73	53.4	2.6	2.5	0.632	0.077	0.071	0.083	0.031	0.998	0.999
3.73	3.55	45.7	2.6	2.5	0.663	0.087	0.093	0.095	0.037	0.997	0.999
3.55	3.39	35.9	2.4	2.3	0.618	0.095	0.079	0.104	0.041	0.997	0.999
3.39	3.26	30.4	2.3	2.2	0.564	0.098	0.078	0.107	0.044	0.995	0.999
3.26	3.15	25.5	2.2	2.1	0.571	0.112	0.088	0.123	0.050	0.995	0.999
3.15	3.05	17.1	2.0	2.0	0.541	0.151	0.112	0.164	0.065	0.994	0.998
3.05	2.96	16.2	2.0	1.9	0.519	0.152	0.103	0.166	0.065	0.994	0.999
2.96	2.89	12.3	1.9	1.9	0.516	0.188	0.150	0.205	0.080	0.988	0.997
2.89	2.82	11.3	1.9	1.9	0.512	0.201	0.145	0.219	0.086	0.990	0.997
2.82	2.75	9.6	1.9	1.9	0.496	0.220	0.170	0.240	0.095	0.984	0.996
2.75	2.69	8.4	1.9	1.9	0.492	0.249	0.187	0.272	0.107	0.984	0.996
2.69	2.64	6.7	1.9	1.9	0.513	0.310	0.260	0.339	0.135	0.966	0.991
2.64	2.59	6.2	1.9	1.9	0.482	0.305	0.247	0.333	0.132	0.966	0.991
2.59	2.54	6.7	1.8	1.8	0.495	0.301	0.221	0.329	0.131	0.970	0.992
2.54	2.50	5.9	1.8	1.8	0.510	0.343	0.259	0.375	0.149	0.962	0.990
All reflections		37.1	2.3	2.2	0.547	0.082	0.058	0.089	0.035		

Shell Lower limit	Shell Upper limit	I/Sigma in resolution shells: % of of reflections with I / Sigma less than 0	1	2	3	5	10	20	>20	total
50.00	6.78	1.0	1.9	2.7	3.7	4.8	9.4	23.1	76.6	99.7
6.78	5.38	1.0	4.0	6.5	8.9	14.4	25.8	51.7	48.3	100.0
5.38	4.70	0.6	4.1	7.6	10.6	15.6	28.0	52.5	47.5	100.0
4.70	4.27	0.7	3.4	6.5	10.3	15.6	27.5	51.3	48.7	100.0
4.27	3.97	2.4	7.0	11.6	16.3	23.5	37.9	62.0	38.0	100.0
3.97	3.73	4.5	10.6	16.3	20.3	28.7	41.9	64.1	35.9	100.0
3.73	3.55	3.7	10.6	18.6	22.2	30.4	46.2	68.4	31.6	100.0
3.55	3.39	7.0	15.2	23.2	29.5	37.7	53.4	74.8	25.2	100.0
3.39	3.26	6.1	19.6	28.4	35.1	44.6	59.1	78.7	21.3	100.0
3.26	3.15	7.2	21.3	33.5	39.5	48.1	62.3	80.2	19.7	99.9
3.15	3.05	11.1	26.7	37.6	43.9	54.1	71.0	87.4	12.0	99.4
3.05	2.96	9.4	24.8	35.3	42.8	54.1	70.0	86.9	11.0	97.9
2.96	2.89	10.0	27.6	39.4	46.2	56.4	72.9	88.7	7.4	96.2
2.89	2.82	11.0	30.5	41.1	48.4	59.9	73.6	88.5	6.6	95.1
2.82	2.75	10.8	29.0	41.4	49.9	58.8	73.4	87.5	4.6	92.0
2.75	2.69	10.7	32.2	44.0	50.5	60.0	75.5	86.2	3.6	89.7
2.69	2.64	11.5	31.7	42.7	51.8	61.2	75.8	84.8	1.4	86.1
2.64	2.59	10.7	30.6	42.1	48.9	60.2	71.8	80.2	1.3	81.5
2.59	2.54	10.2	28.5	40.0	47.3	56.2	68.8	76.9	1.4	78.3
2.54	2.50	10.5	27.8	39.7	46.3	55.9	67.3	74.1	0.8	74.8
All hkl		6.9	19.2	27.6	33.3	41.6	55.1	72.0	22.6	94.6

Shell		Summary of observation redundancies:										
Lower	Upper	% of reflections with given No. of observations										
limit	limit	0	1	2	3	4	5-6	7-8	9-12	13-19	>19	total
50.00	6.78	0.3	0.2	3.0	4.2	20.5	15.2	56.6	0.0	0.0	0.0	99.7
6.78	5.38	0.0	0.4	3.1	8.3	9.0	36.0	43.2	0.0	0.0	0.0	100.0
5.38	4.70	0.0	0.1	0.9	4.4	10.0	21.2	63.4	0.0	0.0	0.0	100.0
4.70	4.27	0.0	0.0	0.9	2.5	9.9	17.8	69.0	0.0	0.0	0.0	100.0
4.27	3.97	0.0	0.0	0.5	2.0	11.0	12.6	74.0	0.0	0.0	0.0	100.0
3.97	3.73	0.0	0.1	0.6	2.0	9.0	13.3	74.9	0.0	0.0	0.0	100.0
3.73	3.55	0.0	0.0	1.1	5.1	5.8	31.3	56.7	0.0	0.0	0.0	100.0
3.55	3.39	0.0	0.1	0.6	5.2	6.7	36.2	51.1	0.0	0.0	0.0	100.0
3.39	3.26	0.0	0.5	1.8	5.2	8.5	49.0	35.1	0.0	0.0	0.0	100.0
3.26	3.15	0.1	0.8	2.2	6.7	7.4	40.5	42.4	0.0	0.0	0.0	99.9
3.15	3.05	0.6	1.6	3.7	6.7	6.6	24.7	55.9	0.0	0.0	0.0	99.4
3.05	2.96	2.1	2.1	3.7	5.0	6.7	20.6	59.7	0.0	0.0	0.0	97.9
2.96	2.89	3.8	2.4	3.5	4.2	7.4	21.1	57.5	0.0	0.0	0.0	96.2
2.89	2.82	4.9	3.0	3.9	5.8	5.7	22.7	54.0	0.0	0.0	0.0	95.1
2.82	2.75	8.0	5.2	3.2	5.2	6.6	22.2	49.7	0.0	0.0	0.0	92.0
2.75	2.69	10.3	5.8	2.3	4.6	6.0	22.2	48.9	0.0	0.0	0.0	89.7
2.69	2.64	13.9	4.9	2.7	5.1	6.5	21.3	45.6	0.0	0.0	0.0	86.1
2.64	2.59	18.5	5.6	3.2	3.6	7.4	21.6	40.2	0.0	0.0	0.0	81.5
2.59	2.54	21.7	4.0	3.2	3.5	6.3	20.2	41.1	0.0	0.0	0.0	78.3
2.54	2.50	25.2	4.7	2.8	3.8	6.5	20.0	37.0	0.0	0.0	0.0	74.8
All hkl		5.4	2.0	2.3	4.7	8.2	24.4	52.9	0.0	0.0	0.0	94.6

Shell		
Lower limit	Upper limit	Average Redundancy Per Shell
50.00	6.78	6.3
6.78	5.38	5.9
5.38	4.70	6.5
4.70	4.27	6.7
4.27	3.97	6.9
3.97	3.73	6.9
3.73	3.55	6.4
3.55	3.39	6.2
3.39	3.26	5.8
3.26	3.15	6.0
3.15	3.05	6.2
3.05	2.96	6.3
2.96	2.89	6.2
2.89	2.82	6.1
2.82	2.75	6.0
2.75	2.69	6.0
2.69	2.64	6.0
2.64	2.59	5.9
2.59	2.54	6.0
2.54	2.50	5.9
All hkl		6.2

NADH-CPILE-a

Summary of reflections intensities and R-factors by shells

R linear = SUM (ABS(I - <I>)) / SUM (I)

R square = SUM ((I - <I>) ** 2) / SUM (I ** 2)

Chi**2 = SUM ((I - <I>) ** 2) / (Error ** 2 * N / (N-1)))

In all sums single measurements are excluded

Shell limit	Lower Upper Angstrom	Average I	Average error	Stat.	Norm. Chi**2	Linear R-fac	Square R-fac	Rmeas	Rpim	CC1/2	CC*
50.00	6.13	2235.9	33.3	11.6	3.055	0.037	0.040	0.041	0.017	0.999	1.000
6.13	4.87	1353.9	22.0	11.1	3.593	0.049	0.049	0.054	0.022	0.998	1.000
4.87	4.25	1832.8	29.4	14.3	3.901	0.052	0.055	0.058	0.024	0.998	0.999
4.25	3.86	1446.0	25.2	13.3	3.899	0.057	0.056	0.063	0.026	0.997	0.999
3.86	3.59	1148.1	21.6	12.9	4.044	0.065	0.062	0.071	0.029	0.997	0.999
3.59	3.38	943.4	19.4	12.1	4.100	0.069	0.057	0.076	0.032	0.997	0.999
3.38	3.21	705.0	16.1	11.3	3.944	0.079	0.065	0.087	0.035	0.997	0.999
3.21	3.07	503.4	13.5	10.4	3.621	0.092	0.074	0.101	0.041	0.996	0.999
3.07	2.95	398.3	12.1	9.9	3.662	0.103	0.072	0.112	0.045	0.997	0.999
2.95	2.85	309.4	11.0	9.5	3.442	0.123	0.092	0.134	0.054	0.994	0.998
2.85	2.76	227.6	10.1	9.2	3.093	0.146	0.107	0.160	0.064	0.993	0.998
2.76	2.68	193.7	9.7	9.0	3.067	0.170	0.122	0.185	0.073	0.992	0.998
2.68	2.61	139.7	9.2	8.8	2.844	0.214	0.164	0.233	0.091	0.986	0.996
2.61	2.55	136.5	9.1	8.7	2.925	0.213	0.141	0.232	0.091	0.989	0.997
2.55	2.49	118.6	9.0	8.7	2.759	0.235	0.157	0.255	0.100	0.987	0.997
2.49	2.43	97.9	8.8	8.6	2.772	0.283	0.203	0.308	0.120	0.978	0.994
2.43	2.39	88.0	8.8	8.6	2.634	0.305	0.218	0.332	0.130	0.973	0.993
2.39	2.34	80.7	8.8	8.6	2.584	0.318	0.224	0.346	0.136	0.974	0.993
2.34	2.30	71.5	8.7	8.5	2.479	0.337	0.237	0.368	0.145	0.973	0.993
2.30	2.26	62.9	9.6	9.5	2.429	0.369	0.263	0.408	0.169	0.948	0.986
All reflections		620.2	15.0	10.3	3.241	0.077	0.054	0.084	0.034		

Shell		I/Sigma in resolution shells: % of of reflections with I / Sigma less than								
Lower limit	Upper limit	0	1	2	3	5	10	20	>20	total
50.00	6.13	0.8	1.4	1.7	1.9	2.5	4.7	8.6	87.3	95.9
6.13	4.87	1.8	2.2	3.0	4.1	5.4	9.5	17.2	82.7	99.9
4.87	4.25	1.0	1.2	2.4	3.3	4.6	7.7	13.8	85.6	99.5
4.25	3.86	2.5	3.2	4.2	5.3	6.9	12.4	21.0	78.6	99.5
3.86	3.59	2.8	3.9	5.1	6.2	8.8	13.6	25.4	74.0	99.4
3.59	3.38	2.3	3.8	5.2	6.6	8.7	16.2	28.0	71.4	99.3
3.38	3.21	2.1	3.9	5.2	7.8	11.5	21.9	37.2	62.2	99.4
3.21	3.07	2.3	4.6	8.5	11.8	17.7	26.9	43.3	55.7	99.0
3.07	2.95	3.0	5.4	7.8	11.2	16.4	27.1	49.9	49.1	99.0
2.95	2.85	3.3	6.1	9.2	13.2	18.4	34.0	54.8	44.3	99.1
2.85	2.76	3.0	6.4	10.6	15.7	25.4	41.5	63.7	34.6	98.3
2.76	2.68	3.7	7.7	14.6	19.5	28.1	46.3	66.7	32.4	99.1
2.68	2.61	4.1	8.4	15.2	23.2	34.6	56.6	74.8	23.9	98.7
2.61	2.55	4.7	10.2	17.9	24.9	36.5	55.8	76.4	21.6	98.0
2.55	2.49	4.7	10.5	17.6	26.6	39.8	60.9	80.1	17.9	98.0
2.49	2.43	4.3	11.8	19.8	28.9	44.7	65.6	81.8	16.0	97.8
2.43	2.39	6.7	13.8	22.8	32.6	47.3	68.5	84.8	13.2	98.0
2.39	2.34	4.6	12.8	23.5	34.1	51.4	71.3	87.1	11.1	98.1
2.34	2.30	7.6	16.7	29.7	40.2	54.6	74.9	87.9	9.7	97.6
2.30	2.26	9.5	20.1	33.9	43.8	59.4	76.1	88.1	6.9	95.0
All hkl		3.7	7.6	12.7	17.8	25.8	39.1	54.0	44.4	98.4

Shell		Summary of observation redundancies:										
Lower	Upper	% of reflections with given No. of observations										
limit	limit	0	1	2	3	4	5-6	7-8	9-12	13-19	>19	total
50.00	6.13	4.1	1.2	3.9	5.7	22.9	24.1	38.2	0.0	0.0	0.0	95.9
6.13	4.87	0.1	0.9	2.4	6.2	18.8	24.1	47.6	0.0	0.0	0.0	99.9
4.87	4.25	0.5	1.1	2.6	6.4	19.0	23.4	46.9	0.0	0.0	0.0	99.5
4.25	3.86	0.5	0.6	3.6	7.8	17.7	24.6	45.2	0.0	0.0	0.0	99.5
3.86	3.59	0.6	0.9	3.0	7.7	20.0	24.4	43.3	0.0	0.0	0.0	99.4
3.59	3.38	0.7	0.8	3.4	7.3	18.3	26.3	43.2	0.0	0.0	0.0	99.3
3.38	3.21	0.6	0.9	3.2	6.2	15.7	27.2	46.2	0.0	0.0	0.0	99.4
3.21	3.07	1.0	1.4	3.3	5.4	14.0	26.5	48.3	0.0	0.0	0.0	99.0
3.07	2.95	1.0	1.2	2.4	5.7	14.3	25.7	49.7	0.0	0.0	0.0	99.0
2.95	2.85	0.9	0.9	3.4	6.0	11.2	23.7	53.9	0.0	0.0	0.0	99.1
2.85	2.76	1.7	0.7	3.2	5.1	10.6	26.0	52.8	0.0	0.0	0.0	98.3
2.76	2.68	0.9	0.9	3.0	4.6	10.9	25.1	54.5	0.0	0.0	0.0	99.1
2.68	2.61	1.3	1.3	2.9	5.6	8.1	25.1	55.6	0.0	0.0	0.0	98.7
2.61	2.55	2.0	0.8	2.5	5.5	8.3	23.3	57.6	0.0	0.0	0.0	98.0
2.55	2.49	2.0	0.9	2.4	5.0	8.8	24.2	56.8	0.0	0.0	0.0	98.0
2.49	2.43	2.2	0.8	2.9	4.5	7.3	26.6	55.8	0.0	0.0	0.0	97.8
2.43	2.39	2.0	1.8	2.6	3.8	7.6	24.6	57.7	0.0	0.0	0.0	98.0
2.39	2.34	1.9	1.5	3.0	5.5	8.0	25.0	55.2	0.0	0.0	0.0	98.1
2.34	2.30	2.4	1.1	2.6	4.5	8.5	30.6	50.2	0.0	0.0	0.0	97.6
2.30	2.26	5.0	3.3	6.5	10.5	12.1	26.4	36.2	0.0	0.0	0.0	95.0
All hkl		1.6	1.2	3.1	5.9	13.2	25.3	49.7	0.0	0.0	0.0	98.4

Shell		
Lower	Upper	Average Redundancy Per Shell
limit	limit	
50.00	6.13	5.6
6.13	4.87	5.9
4.87	4.25	5.9
4.25	3.86	5.8
3.86	3.59	5.8
3.59	3.38	5.8
3.38	3.21	5.9
3.21	3.07	6.0
3.07	2.95	6.0
2.95	2.85	6.1
2.85	2.76	6.2
2.76	2.68	6.2
2.68	2.61	6.3
2.61	2.55	6.3
2.55	2.49	6.3
2.49	2.43	6.3
2.43	2.39	6.3
2.39	2.34	6.2
2.34	2.30	6.2
2.30	2.26	5.4
All hkl		6.0

E49R CPILE-a

Summary of reflections intensities and R-factors by shells

R linear = SUM (ABS(I - <I>)) / SUM (I)

R square = SUM ((I - <I>) ** 2) / SUM (I ** 2)

Chi**2 = SUM ((I - <I>) ** 2) / (Error ** 2 * N / (N-1)))

In all sums single measurements are excluded

Shell limit	Lower Upper Angstrom	Average I	Average error	Stat.	Norm. Chi**2	Linear R-fac	Square R-fac	Rmeas	Rpim	CC1/2	CC*
50.00	5.16	269.0	6.9	5.8	1.499	0.054	0.059	0.059	0.023	0.998	1.000
5.16	4.09	236.8	6.6	5.8	1.126	0.055	0.060	0.060	0.023	0.997	0.999
4.09	3.58	173.8	5.5	4.9	1.290	0.066	0.071	0.072	0.028	0.997	0.999
3.58	3.25	119.6	4.6	4.2	1.360	0.079	0.080	0.087	0.035	0.997	0.999
3.25	3.02	74.8	3.5	3.3	1.173	0.095	0.091	0.103	0.040	0.995	0.999
3.02	2.84	47.5	2.9	2.8	1.073	0.122	0.112	0.132	0.051	0.993	0.998
2.84	2.70	32.5	2.7	2.6	0.978	0.158	0.145	0.171	0.065	0.990	0.997
2.70	2.58	22.8	2.6	2.6	0.911	0.208	0.191	0.225	0.085	0.984	0.996
2.58	2.48	19.6	2.8	2.8	0.821	0.227	0.200	0.247	0.096	0.977	0.994
2.48	2.39	15.7	2.9	2.9	0.794	0.277	0.250	0.303	0.119	0.964	0.991
2.39	2.32	13.8	3.0	3.0	0.781	0.317	0.282	0.346	0.139	0.960	0.990
2.32	2.25	12.0	3.0	3.0	0.762	0.379	0.350	0.413	0.162	0.950	0.987
2.25	2.19	11.0	3.0	3.0	0.670	0.401	0.339	0.437	0.172	0.945	0.986
2.19	2.14	8.6	3.0	3.0	0.620	0.488	0.409	0.534	0.213	0.923	0.980
2.14	2.09	7.3	3.0	3.0	0.590	0.552	0.464	0.606	0.247	0.907	0.975
2.09	2.05	6.3	3.1	3.1	0.630	0.606	0.557	0.671	0.282	0.881	0.968
2.05	2.01	4.8	3.2	3.2	0.507	0.705	0.537	0.790	0.346	0.841	0.956
2.01	1.97	4.0	3.4	3.4	0.494	0.777	0.593	0.880	0.401	0.784	0.937
1.97	1.93	3.4	3.7	3.7	0.510	0.868	0.609	1.002	0.485	0.678	0.899
1.93	1.90	3.2	3.9	3.9	0.626	0.803	0.632	0.939	0.474	0.799	0.942
All reflections		56.8	3.7	3.5	0.902	0.104	0.070	0.113	0.045		

Shell		I/Sigma in resolution shells:								
Lower	Upper	% of of reflections with I / Sigma less than								
limit	limit	0	1	2	3	5	10	20	>20	total
50.00	5.16	0.7	1.9	3.5	4.4	5.7	10.9	25.4	74.1	99.6
5.16	4.09	0.3	1.6	3.4	4.6	7.3	13.7	29.3	70.6	99.9
4.09	3.58	1.1	2.4	3.7	6.2	10.0	18.1	37.0	63.0	100.0
3.58	3.25	1.4	3.8	6.3	9.3	13.9	24.6	47.9	52.1	100.0
3.25	3.02	1.4	4.8	8.9	12.5	19.2	35.2	60.9	39.1	100.0
3.02	2.84	2.9	7.3	12.3	17.1	26.5	46.1	72.8	27.2	100.0
2.84	2.70	2.2	8.4	17.0	25.2	36.4	58.4	82.8	17.2	100.0
2.70	2.58	4.3	13.1	24.2	33.9	48.1	68.7	89.6	10.4	100.0
2.58	2.48	4.6	16.0	28.6	39.2	53.9	74.5	92.2	7.8	100.0
2.48	2.39	6.1	20.1	34.2	45.8	61.7	80.2	95.2	4.8	100.0
2.39	2.32	7.2	23.1	40.1	51.1	67.0	84.0	97.1	2.9	100.0
2.32	2.25	8.7	26.2	44.3	56.1	70.9	87.4	97.7	2.2	99.9
2.25	2.19	8.7	29.8	49.5	61.1	75.1	88.5	98.5	1.5	100.0
2.19	2.14	11.8	35.9	57.0	67.7	79.6	93.2	99.4	0.6	100.0
2.14	2.09	13.6	42.6	61.3	72.5	82.9	94.4	99.6	0.1	99.6
2.09	2.05	17.0	46.7	67.4	77.5	86.4	96.3	99.3	0.1	99.4
2.05	2.01	18.1	52.7	73.0	82.3	90.5	97.1	98.4	0.0	98.4
2.01	1.97	21.3	57.6	76.8	84.7	91.9	96.6	97.5	0.0	97.5
1.97	1.93	26.4	60.2	77.0	83.5	88.1	91.6	92.1	0.0	92.1
1.93	1.90	19.5	46.8	61.2	66.7	70.5	72.5	72.8	0.0	72.8
All hkl		8.8	24.8	37.1	44.6	53.8	66.1	78.9	19.1	98.0

Shell		Summary of observation redundancies: % of reflections with given No. of observations										
Lower limit	Upper limit	0	1	2	3	4	5-6	7-8	9-12	13-19	>19	total
50.00	5.16	0.4	0.4	5.4	3.4	18.9	26.8	44.7	0.0	0.0	0.0	99.6
5.16	4.09	0.1	0.5	1.6	2.1	12.8	19.6	63.3	0.0	0.0	0.0	99.9
4.09	3.58	0.0	0.3	2.7	2.3	10.9	27.8	55.9	0.0	0.0	0.0	100.0
3.58	3.25	0.0	0.3	3.6	2.7	13.8	39.7	40.0	0.0	0.0	0.0	100.0
3.25	3.02	0.0	0.1	2.0	1.6	11.3	28.4	56.6	0.0	0.0	0.0	100.0
3.02	2.84	0.0	0.0	1.3	1.8	10.1	22.9	63.9	0.0	0.0	0.0	100.0
2.84	2.70	0.0	0.2	1.2	1.1	9.4	18.3	69.8	0.0	0.0	0.0	100.0
2.70	2.58	0.0	0.1	1.4	1.3	8.9	16.0	72.4	0.0	0.0	0.0	100.0
2.58	2.48	0.0	0.2	2.9	1.8	10.6	29.0	55.5	0.0	0.0	0.0	100.0
2.48	2.39	0.0	0.2	3.7	1.6	10.7	34.4	49.3	0.0	0.0	0.0	100.0
2.39	2.32	0.0	0.2	3.6	3.4	10.9	40.4	41.5	0.0	0.0	0.0	100.0
2.32	2.25	0.1	0.4	2.3	3.0	9.4	30.6	54.3	0.0	0.0	0.0	99.9
2.25	2.19	0.0	0.3	2.6	2.5	10.2	31.6	52.8	0.0	0.0	0.0	100.0
2.19	2.14	0.0	0.1	2.4	3.2	11.8	36.2	46.3	0.0	0.0	0.0	100.0
2.14	2.09	0.4	0.4	3.1	4.8	15.8	36.7	38.9	0.0	0.0	0.0	99.6
2.09	2.05	0.6	1.6	6.8	8.1	19.5	32.0	31.4	0.0	0.0	0.0	99.4
2.05	2.01	1.6	2.1	9.0	13.0	21.5	30.1	22.7	0.0	0.0	0.0	98.4
2.01	1.97	2.5	5.6	14.0	15.0	22.1	24.0	16.7	0.0	0.0	0.0	97.5
1.97	1.93	7.9	9.9	16.1	16.9	21.9	18.4	8.9	0.0	0.0	0.0	92.1
1.93	1.90	27.2	13.2	14.1	11.7	17.6	14.3	2.0	0.0	0.0	0.0	72.8
All hkl		2.0	1.8	5.0	5.0	13.9	27.8	44.5	0.0	0.0	0.0	98.0

Shell		
Lower limit	Upper limit	Average Redundancy Per Shell
50.00	5.16	6.0
5.16	4.09	6.7
4.09	3.58	6.5
3.58	3.25	6.0
3.25	3.02	6.5
3.02	2.84	6.7
2.84	2.70	6.8
2.70	2.58	6.9
2.58	2.48	6.4
2.48	2.39	6.3
2.39	2.32	6.1
2.32	2.25	6.4
2.25	2.19	6.4
2.19	2.14	6.2
2.14	2.09	5.9
2.09	2.05	5.4
2.05	2.01	4.9
2.01	1.97	4.4
1.97	1.93	3.8
1.93	1.90	3.3
All hkl		5.9

.....